國立臺灣大學工學院材料科學與工程學系
碩士論文

Department of Materials Science and Engineering
College of Engineering
National Taiwan University
Master's Thesis

基於醣類高分子/奈米碳管複合材料之界面工程於熱電應用

Tailoring Interfaces of Sugar-based Nanocomposites Materials for Thermoelectric Application

陳彥宇

Yen-Yu Chen

指導教授：劉振良 博士
Advisor: Cheng-Liang Liu, Ph.D.

中華民國 114 年 7 月
July 2025

doi:10.6342/NTU202502950

致謝

一轉眼，從我第一次走進 OPMD 實驗室到現在，已經四年了。這幾年不只是做實驗，更是在各種挑戰中慢慢累積經驗，也讓我成長不少。在本論文完成之際，首先要感謝我的指導老師劉振良教授，在研究過程中，感謝他給予我許多指導與寶貴的建議，也提供了許多磨練的機會，讓我在學術上受益良多。除此之外，也很感謝在法國合作的 Borsali 教授。他不僅幽默風趣，每次討論時也總是能帶來很多有趣又啟發性的想法。當然也很感謝提供我研究材料的 Hong Li，在我待在法國的那段時間，他也帶著我一起做實驗，讓我更快熟悉 CERMAV 的環境。希望你在博後結束之後，能順利在法國找到理想的工作，繼續留在那邊發展。另外也感謝諶玉真教授、致榮與 Tanaka 同學協助我把研究完成的更完善。

這段時間，我很感謝所有 OPMD 的成員。首先，在我還是專題生的時候，亦淳是第一個帶著我們快速熟悉電晶體製程的學長，為我往後的研究奠下基礎。張云也在我電晶體的題目幫了我很多，除了研究上的認真負責，她活潑外向的性格，與 Arthur、彥廷和家豪一起帶給實驗室許多歡樂與有趣的回憶。博班的大學長姐們更是維持這個實驗室運轉不可或缺的角色。當實驗遇到問題時，柏伸與維妮總是能給我許多不一樣的新想法或實用的建議。很高興紹桓能在畢業後還回來這裡當博後，身為在這間實驗室待的最久的人，包攬了實驗室大大小小的事務，彷彿沒有他解決不了的問題。

在我碩班的第一篇研究中，孟儒絕對是幫助我最多的人，他豐富的經驗也幫助我們少走了很多冤枉路，隨著更深入的認識，外表看似安靜的孟儒在熟了之後也是有很多幹話。靠著飲料續命的建發則是我們 OPMD 的開心果，總是扮演者帶動氣氛角色的他幫助了很多新同學更好的融入這個實驗室。嘉佑也為實驗室扛下了許多雜務，除此之外，他也總是喜歡跑來和我們一起聊天八卦。說到聊天，晴寶肯定是話最多最吵的那個(雖然她自己都不承認)，身為老師最喜歡的小秘書，總是將各

doi:10.6342/NTU202502950

項事務安排的很好，此外也教會我怎麼把簡報設計的更好看。剛認識凌潔時覺得她個性非常活潑，甚至有點瘋瘋的感覺，但相處起來卻非常自然、舒服，她也會去關心周遭人的情緒或狀況十分貼心，很開心能在未來職場上繼續當同事。

隨著待在實驗室的時間越來越久，總是會有一批又一批的新血加入，讓這個地方一直充滿活力。志偉在做實驗的方面令人十分放心，我也常常與他討論實驗的細節，但請大家多多關心志偉的牙齒，他常常因為要去看牙醫 meeting 請假，還是其實是吃太多大餐造成的。我也十分感謝以璿多次帶我去打熱分析，我們總是有很多的話題可以聊天，要相信自己很棒，妳一定夠堅強可以把碩士順利念完的。但請不要給她喝太多酒，不然會看到她比較不一樣的一面。同樣不能給他喝太多酒的是一樣從專題生升上來的暐宸，你幾乎都在晚上很認真的做實驗，這點相信我也是學不來的。士庭希望你之後去日本讀書一切順利。我也要感謝滋翎，經過多次的嘗試我們終於試出準確量測 C_p 的方式，讓我得以完成最後缺失的數據順利完成研究，但我真的不想再測 DSC 了。除此之外，在明諺進來之前，我也向他請教一些合成的細節，他的幫忙讓我能順利把我的產物合出來。當然也需要感謝負責管帳的凱西，有妳幫忙處理報帳的事才能維持整個實驗室順利運轉。每次看到翔仁的行事曆，都很佩服他能把事情規劃的井井有條，希望你在剩下的時間內能準時順利完成兩篇研究。至於 Jennifer 跟子禎，雖然你們大部分時間都待在鄭江，比較少機會一起相處，不過之後水膠組就要靠你們兩個撐起來啦。育銓的部分，以後法國那邊的事情就交給你接手了，如果你以後有機會去 Grenoble 也可以問我，真心希望我之後不會留太多東西給你收尾。接下來是我這幾個月的好鄰居冠霖，都還沒正式拿到博士學生身分已經幫老師做太多事了。能連續吃一個禮拜一樣的午餐真的很厲害，期待你開發不一樣的午餐組合。

同時，也要感謝跟我們這一屆的六個同學，這兩年的碩士生活我們也一起經歷許多事情。亦佐，妳總是表現得很客氣，也常常關心身邊同學的狀況。我們在碩一一起處理了許多實驗室的事務，規劃出遊的部分你也幫了我很多，希望妳未來能完

doi:10.6342/NTU202502950

成妳的夢想出國念書。羽媗，剛開始認識妳的時候覺得妳很安靜，但漸漸變熟之後發現妳其實是個很有趣的人，還記得以前我們晚上在工綜聊到很晚，是個值得信任的好朋友，以後聚餐找餐廳的重責大任就交給妳了。鈺皓是我第一個認識的新進同學，雖然平常話不多，總是默默坐在旁邊聽我們聊天，但只要聊到他熱愛的籃球和湖人隊，整個人就會立刻神采飛揚。他的沉穩內斂讓人很放心，是個值得信賴的夥伴，更是我們當中進度最快的男人。政遠則是我做碳管的好夥伴，給人的感覺跟他的開車技術一樣可靠。平常不管是學術討論還是彼此閒閒聊都不會缺席，唯一可能找不到人是午餐揪吃飯的時候，我會想念你沒事起來晃來晃去的樣子。

最後，一路跟我從專題生撐到最後的哲安、靖頡，我們從大一就已經熟識，誤打誤撞一起加入 OPMD，從青澀的專題生一路走到現在能夠獨當一面的研究生。一起成長的過程中留下不少回憶，還有那趟始終沒成行的深坑老街之旅。外表看似冷酷的阿頡實則內心細膩，標準的刀子嘴豆腐心，研究能力強的你在工作上肯定也能如魚得水，期待你哪天錢賺夠了回台東開酒吧肯定要去捧場一下，沒有的話去吃芒果也可以。哲安是大家眼中的萬事通，也是實驗室最熱情、樂於助人的好學長，不知道如果我是學弟你會不會帶我打三次 UV。他同時也是我每天一起買午餐的固定班底，我們聊天內容包羅萬象，什麼都能聊上一輪。相信我們幾個的友誼不會隨著畢業而結束，而是會持續到未來人生的階段。

再次感謝這一路上曾經幫助過我的每一位，不論是給我研究指引的老師、一起趕進度的同伴，還是默默支持著我的家人。有你們的陪伴，讓這段求學過程不再孤單，也變得充實又有意義。這段經歷會一直留在我的心裡，陪我走向下一段旅程。

doi:10.6342/NTU202502950

Abstract

Organic thermoelectric materials represent a promising frontier in sustainable energy technology, offering the ability to convert waste heat directly into electricity. Among them, carbon nanotubes (CNTs) and their nanocomposites have emerged as strong candidates due to their high thermoelectric performance, exceptional mechanical properties, and unique physicochemical characteristics. In this study, sugar-based polymers are utilized to enhance the dispersibility of CNTs, thereby promoting the formation of efficient conductive pathways within the nanocomposites and contributing to the development of more sustainable energy harvesting technologies.

In the first part of this research, two sugar-based block copolymers (BCPs), maltotriose-*block*-polystyrene (MT-PS) and maltoheptaose-*block*-polystyrene (MH-PS), featuring varying oligosaccharide and polystyrene block lengths, were synthesized and characterized to investigate their influence on CNT dispersibility and subsequent thermoelectric properties. The inherent amphiphilic characteristics of these BCPs enable efficient dispersion of CNTs in both N-methyl-2-pyrrolidone (NMP) and N,N-dimethylformamide (DMF). These solvents prove instrumental in the fabrication of BCP/CNT thin films, yielding both p-type and n-type nanocomposites. Through optimization of processing conditions, the resultant nanohybrids exhibit enhanced

doi:10.6342/NTU202502950

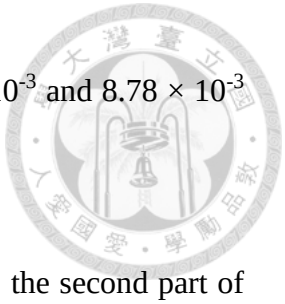

thermoelectric properties, with figure of merit (zT) reaching 9.10×10^{-3} and 8.78×10^{-3} for p-type and n-type materials, respectively.

Distinct from the aforementioned physical adsorption approach, the second part of this study presents the first report of a stable aqueous suspension of sugar-functionalized CNTs applied to thermoelectric. A systematic investigation of bio-based materials, maltotriose (MT) and maltoheptaose (MH)-based CNTs, reveals that the sugar polymer plays a crucial role in governing both dispersion stability and thermoelectric performance. The multiple hydroxyl groups present in the oligosaccharide segments facilitate strong hydrogen bonding with aqueous solvent, significantly improving the colloidal stability of the functionalized CNTs. Furthermore, the anchored sugar chains on the CNT surface result in a four-fold reduction in thermal conductivity, which outweighs the electrical penalty and contributes to an overall improvement. Sugar-functionalized CNT-MH exhibits the highest zT value of 1.46×10^{-3}, outperforming pristine CNTs in aqueous media. Overall, this study offers a versatile and sustainable platform for engineering CNT interfaces in solution-processable thermoelectric systems.

Keywords: thermoelectric, carbon nanotube, sugar-based polymer, nanocomposite, interface engineering

doi:10.6342/NTU202502950

摘要

熱電材料能夠將廢熱直接轉換為電能，是綠色能源技術中極具發展潛力的研究領域。近年來，奈米碳管（CNTs）及其奈米複合材料，因具備優異的熱電性能、優良的機械強度與獨特的物理化學性質，已被廣泛認可為具前瞻性的熱電材料候選者。然而，CNTs 在溶液中易產生聚集現象，限制其在材料中的均勻分散與電荷傳輸效率。為改善此問題，本研究引入醣基結構的高分子作為分散劑，藉由分子間作用力提升 CNTs 在溶液中的穩定分散性，進而促進奈米複合材料中連續且高效導電通道的構建，對提升整體熱電性能具有關鍵性意義。此策略有望推動高效能熱電材料的設計，並為再生能源轉換技術提供可行性方案。

本研究的第一部分聚焦於奈米碳管系統中，導入兩種具有不同寡醣鏈段與苯乙烯（polystyrene, PS）鏈段長度的醣類嵌段共聚物（BCPs），分別為 maltotriose-block-polystyrene（MT-PS）與 maltoheptaose-block-polystyrene（MH-PS），以系統性探討其對奈米碳管分散性與熱電性能之影響。由於這些醣類嵌段共聚物具備明顯的雙親性，其親水性寡醣鏈段可與極性溶劑產生良好互溶性，疏水性苯乙烯鏈段則有助於與奈米碳管表面產生 π–π 作用力，從而實現奈米碳管在 N-甲基吡咯烷酮（NMP）與 N,N-二甲基甲醯胺（DMF）等極性溶劑中的穩定分散。透過溶劑選擇與製程過程的控制，可有效調變複合材料的導電特性，進一步構築具有 p 型與 n 型行為的奈米熱電複合材料。經過製程條件的優化後，所得材料展現出優異的熱電性能，其中 p 型與 n 型複合薄膜分別達到 9.10×10^{-3} 和 8.78×10^{-3} 的熱電優值（zT）。此結果也展現出溶劑與材料間相互作用的重要性，以提升奈米複合材料熱電效率。

有別於前述基於物理吸附之分散策略，本研究的第二部分成功合成具醣類官能基的奈米碳管，可穩定分散於水相溶劑中並首次報導應用於熱電材料系統。針對以 maltotriose（MT）與 maltoheptaose（MH）為主體的醣類高分子所官能化之奈

doi:10.6342/NTU202502950

米碳管進行系統性探討，結果顯示醣類鏈段在提升分散穩定性與改善熱電性能方面扮演關鍵角色。由於醣鏈中富含羥基基團，能與水溶劑形成氫鍵作用力，顯著提高奈米碳管於水相中的穩定性。另一方面，碳管表面的醣類分子亦有助於降低其熱傳導特性，使官能化奈米碳管之熱導率降低至未修飾奈米碳管的約四分之一。儘管表面修飾導致導電性略有下降，整體熱電性能仍因顯著降低熱導率而獲得提升。在所有樣品中，以 MH 官能基化之奈米碳管（CNT-MH）展現最高熱電優值達 1.46 × 10^{-3}，優於未修飾 CNT 於水相中的表現。上述成果不僅驗證醣類高分子修飾策略在提升熱電效能上的可行性，更提供一項具備永續性、高可調性與溶液製程相容性的界面工程方法，對未來綠色熱電材料之設計與應用具有重要意義。

關鍵詞：熱電、奈米碳管、醣類高分子、奈米複合材料、界面工程

doi:10.6342/NTU202502950

Table of Contents

doi:10.6342/NTU202502950

doi:10.6342/NTU202502950

List of Figures

doi:10.6342/NTU202502950

doi:10.6342/NTU202502950

doi:10.6342/NTU202502950

doi:10.6342/NTU202502950

List of Tables

doi:10.6342/NTU202502950

1. Introduction

1.1. Background

With the rapid advancement of technology and the widespread adoption of artificial intelligence, modern industries are experiencing significantly increased energy demands. This surge in consumption has intensified concerns over energy sustainability, making the global energy crisis one of the most pressing challenges facing humanity today. Today, most conventional power generation methods suffer from substantial energy losses, with heat dissipation being a major inefficiency. In particular, the combustion of fossil fuels (coal, petroleum, and natural gas) results in 60-70% of the input energy being released as waste heat.[1] Therefore, extensive investigations have been undertaken to harness dissipated thermal energy and improve overall energy efficiency. Among the various approaches, thermoelectric (TE) technologies have attracted considerable attention due to their capability to directly convert temperature gradients directly into electrical energy by the Seebeck effect, a phenomenon that was first reported by Thomas J. Seebeck in 1821.[2] Compared to traditional power generation methods, TE systems offer a solid-state, scalable, and environmentally friendly solution, making them highly promising for both waste heat recovery and sustainable energy applications.[3] **Figure 1.1** illustrates the

doi:10.6342/NTU202502950

rising trend in thermoelectric research publications over the past 25 years, highlighting the growing interest and rapid development in this field.

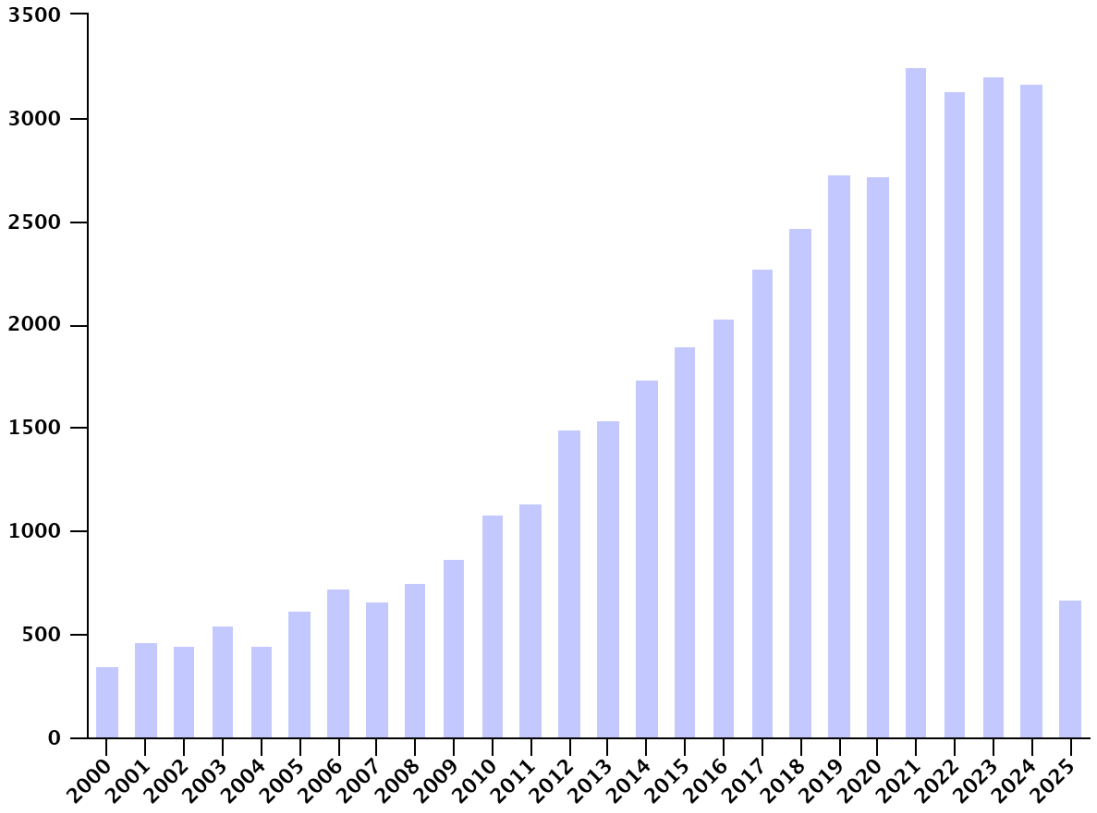

Figure 1.1 Recent publications of thermoelectric researches over the last 25 years. "Thermoelectric" as a keyword obtained from Web of Science database.

1.1.1. Fundamentals of Thermoelectric Phenomena

The Seebeck effect is a fundamental physical phenomenon that enables the direct conversion of a temperature gradient into an electrical voltage across a material. When

doi:10.6342/NTU202502950

two ends of a conductive material or a thermoelectric junction are maintained at different temperatures, charge carriers diffuse from the hot side to the cold side, resulting in a measurable thermovoltage by the following equation:

$$S = -\frac{\partial V}{\partial T} = \frac{V_{cold} - V_{hot}}{T_{hot} - T_{cold}} \quad (1.1)$$

Based on dominant type of charge carriers, thermoelectric materials can be distinguished by the sign of their Seebeck coefficient (S). P-type materials exhibit a positive S, indicating that holes are the majority charge carriers responsible for transport. In contrast, n-type materials display a negative S, signifying that electrons dominate the charge transport.

In order to evaluate the overall thermoelectric performance, two different parameters power factor (PF) and the dimensionless figure of merit (zT) are defined as below:

$$PF = S^2\sigma \quad (1.2)$$

$$zT = \frac{S^2\sigma}{\kappa}\mathrm{T} \quad (1.3)$$

where σ represents the electrical conductivity, κ denotes the thermal conductivity, and T indicates the operating temperature. Achieving optimal zT requires a combination of high σ, high S and low κ. Since all three parameters are inherently dependent on the concentration of charge carriers (presented in **Figure 1.2**), the carrier concentration (n)

doi:10.6342/NTU202502950

plays a critical role in the optimization of zT.[4] Balancing these interdependent properties is essential for maximizing thermoelectric efficiency.

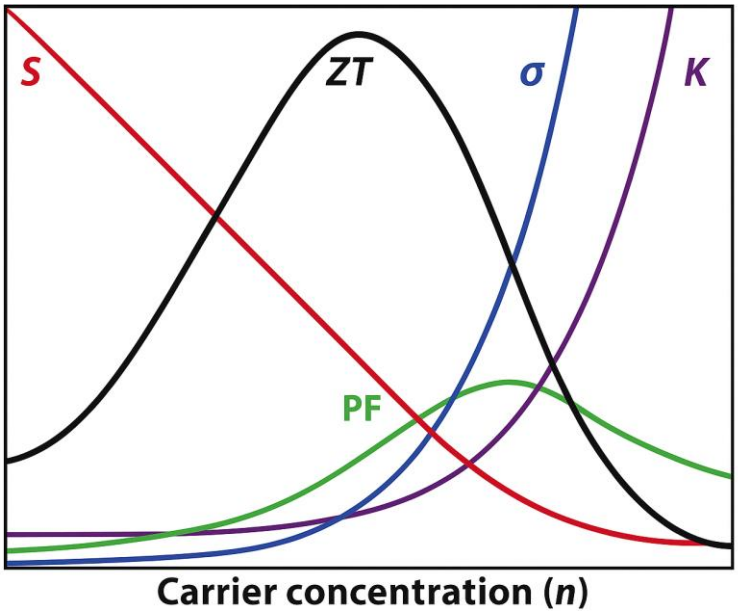

Figure 1.2 Graphical correlation between *S*, σ, κ, ***zT***, and *PF* with respect to *n*.[4]

1.1.2. Development of Thermoelectric Materials

Inorganic TE materials have been extensively studied due to their superior performance. Conventional inorganic TE materials are typically crystalline chalcogenides in their bulk form, with well-known examples including bismuth telluride (Bi_2Te_3) and lead telluride (PbTe). These materials exhibit relatively high TE efficiency, with zT approaching 1.1 at room temperature.[5] Owing to their stable performance and mature processing techniques, the majority of commercial TE devices are currently based on

doi:10.6342/NTU202502950

these heavy-element compounds, despite concerns regarding toxicity, scarcity, and mechanical brittleness.[6] Metal oxide materials arise as another promising candidates for inorganic TE materials, manifesting competitive performance (ZnO: zT = 0.65 at 1247 K[7], $Na_xCoO_{2-\delta}$: zT = 1.2 at 800 K[8]) and demonstrating excellent chemical stability at high temperatures, which enables operation over a wide temperature range.[9]

In contrast to the well-established study of inorganic counterparts, organic thermoelectric (OTE) materials have seen growing interest in recent years. Specifically, the ability to operate efficiently at low temperatures for OTE materials is particularly attractive, as low-temperature waste heat (below 300 °C) accounts for approximately 89% of industrial waste heat, according to a statement by the EU.[10] Furthermore, multiple features such as lightweight, affordability, excellent flexibility, low thermal conductivity, solution processability, and environmental friendliness make OTE materials highly attractive for practical applications.[11]

Solution processable organic conductors are capable of achieving high σ and decent performance.[3] These polymers exhibit semiconducting properties derived from their delocalized π-electron systems along conjugated backbones, combined with inherently low thermal conductivity relative to inorganic compounds. Such features render these polymers well-suited for use in TE devices. Representative materials such as

doi:10.6342/NTU202502950

pure P3HT films have demonstrated high zT value of 0.1 via an epitaxial growth method.[12] PEDOT : PSS following ethylene glycol treatment has achieved a PF of 469 μW m^{-1} K^{-2} and a zT value of 0.42.[13] Various strategies including doping, molecular designing and post-processing have been employed to enhance the TE performance further for organic materials.[14] However, it is challenging to simultaneously optimize all relevant parameters within a single-component material. As an alternative, the fabrication of composites combining two or more materials offers a promising approach to enhance the TE performance of organic systems. As shown in **Figure 1.3**, a variety of carbon nanomaterials form through sp^2 hybridization, including carbon nanotubes (CNTs), graphene and fullerenes are considered favorable conducting fillers owing to their exceptional electrical conductivity. Among these, CNTs are particularly noteworthy for their high aspect ratio and tunable electronic structure, enables efficient charge transport while preserving the flexibility and low thermal conductivity of polymer matrices.[15] Furthermore, the one-dimensional nature of CNTs promotes anisotropic transport, which can be exploited to align thermoelectric and thermal pathways.[16] In this study, CNTs are selected as the primary filler due to these distinctive advantages. The following chapter will explore the role of CNTs in organic TE nanocomposites, highlighting their structural characteristics, impact on charge and heat transport properties and functionalization

doi:10.6342/NTU202502950

strategies.

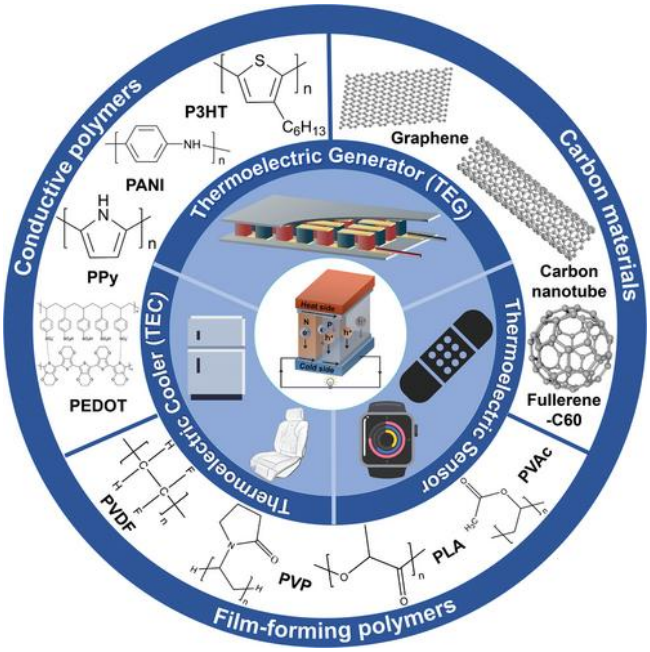

Figure 1.3 Schematic diagram of thermoelectric applications and organic materials commonly used in thermoelectric composites.[17]

1.2. Carbon Nanotubes Nanocomposites in Thermoelectric Applications

Discovered in 1991,[18] CNTs are cylindrical nanostructures composed of rolled graphene sheets and are categorized based on the number of concentric graphene layers: single-walled (SWCNTs), double-walled (DWCNTs), and multi-walled (MWCNTs). Among them, SWCNTs exhibit exceptional electrical conductivity and tunable electronic properties based on chirality, making them ideal for optimizing charge transport in TE applications. To elucidate their potential in this context, the following sections will

doi:10.6342/NTU202502950

examine the structural and electronic properties of pristine CNTs, explore strategies for improving dispersion and charge transport, and discuss surface modification approaches through non-bonding interactions and covalent functionalization.

1.2.1. Structural and Electronic Properties of Pristine CNTs

A key feature that distinguishes SWCNTs and contributes to their diverse properties is their unique structural configuration. Chirality is a fundamental structural characteristic of CNTs, describing the specific orientation in which a graphene sheet is rolled into a cylindrical shape. It is defined by a chiral vector indexed by a pair of integers (n, m), which determines the nanotube's diameter and helical angle. This geometric configuration not only classifies CNTs into armchair, zigzag, or chiral types, but also governs their electronic behavior, dictating whether a CNT exhibits metallic or semiconducting properties. Specifically, CNTs with chiral indices (n, m) where $n - m$ is a multiple of three exhibit metallic or small bandgap semiconducting behavior, while all other configurations result in large-bandgap semiconductors, according to the calculation results of tight-binding model.[19] Furthermore, the electronic density of states, band structure, and optical absorption characteristics can also be modulated by varying the

doi:10.6342/NTU202502950

diameter and chirality of CNTs, which demonstrates their tunable electronic and optoelectronic properties.[20]

Regardless of the importance of chirality, properly sorting CNTs by specific chiralities remains time-consuming and requires distinct procedures for each type.[21] In addition, different chiralities may exert varying degrees of influence depending on the surrounding matrix or composite system, complicating the design of consistent thermoelectric performance.[22] To circumvent these challenges, researchers rely on post-synthetic modification approaches to tune the electronic and thermoelectric properties of CNTs. These include acid-base treatments, small-molecule doping, and incorporation into nanocomposites,[21a, 23] which offer more practical and scalable routes to modulate CNT behavior without the need for precise chirality separation.

Owing to their high surface-to-volume ratio, CNTs are highly sensitive to the surrounding environment. For instance, CNTs tend to exhibit n-type behavior intrinsically; however, upon exposure to oxygen in ambient, they often shift to p-type due to charge transfer effects. Bradley et al. proposed a model correlating the Seebeck coefficient with the density of states in oxygen-doped semiconducting CNT.[24] Meanwhile, solvent selection during CNT film processing has also emerged as a critical factor, capable of

doi:10.6342/NTU202502950

inducing p–n type inversion without relying on external dopants. Hata et al. reported a series of common organic solvents and their corresponding Seebeck coefficients, as presented in **Figure 1.4**. When CNTs are processed with polar aprotic solvents such as DMF and NMP, the unshared electron pairs from adsorbed solvent molecules are transferred to the CNTs, which results in a transition from p-type to n-type behavior. Conversely, CNT dispersions in nonpolar or polar protic solvents tend to retain positive Seebeck coefficients, thereby maintaining their p-type characteristics.[25] Achieving polarity control through intrinsic material and solvent properties, instead of using external chemical dopants, simplifies the fabrication process and eliminates issues related to inhomogeneous dopant distribution.

doi:10.6342/NTU202502950

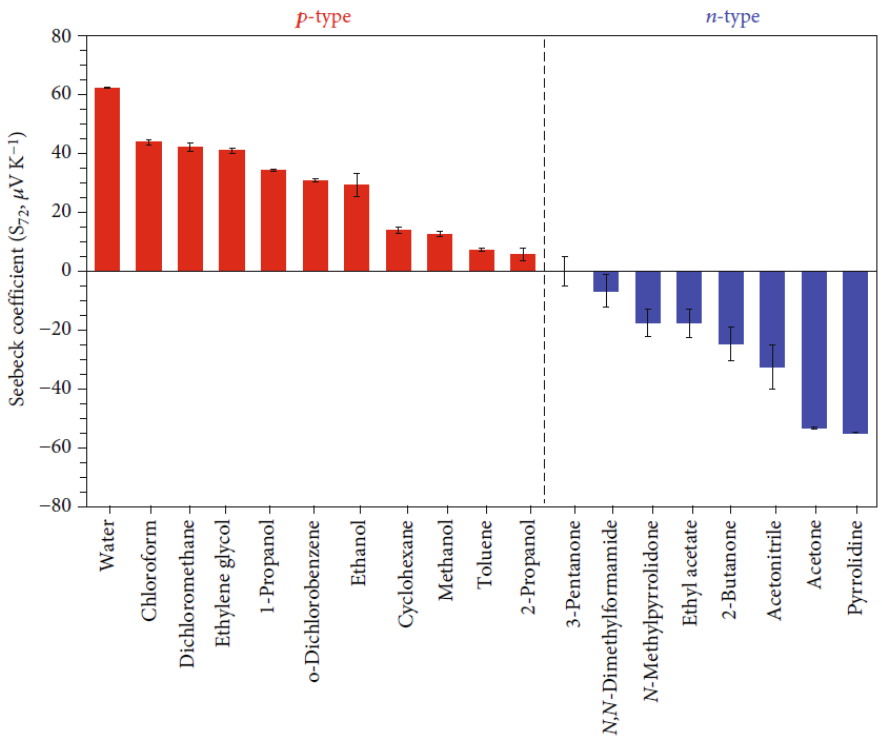

Figure 1.4 Effect of solvent type on Seebeck coefficient at 345 K of CNT films.[25]

1.2.2. Dispersion Methodologies and Electronic Transport Modulation

The electrical and thermal conductivities of CNTs are highly dependent on their structural configuration. Individual SWCNT reach demonstrate exceptionally high thermal conductivity, with longitudinal values reaching up to ~3500 W $m^{-1}K^{-1}$ at room temperature,[26] attributed to their defect-free, aligned graphene structure enabling efficient phonon transport. In contrast, the randomly oriented three-dimensional network of CNT bulk samples, display thermal conductivities that are several orders of magnitude lower due to increased phonon scattering at tube-tube junctions and structural disorder.[27]

doi:10.6342/NTU202502950

For practical applications, scalable bulk forms such as films, mats, or composites are fabricated. However, these assemblies face considerable challenges due to strong inter-tube van der Waals interactions, with binding energies of approximately 500 eV per micrometer of inter-tube contact.[28] These interactions promote CNT aggregation, thereby hindering both processability and overall performance. In such aggregated networks, electron transport is further impeded by high resistance at poorly connected junctions between misaligned tubes.[29] Therefore, attaining well-dispersed CNTs is crucial for maximizing charge transport efficiency and ensuring uniform film formation, which are essential for high-performance applications in electronics, energy devices, and composites.

Fabricating CNT thin films typically requires a preliminary step in which the CNTs are pre-dispersed in a suitable solvent. Due to their hydrophobic nature, CNTs tend to agglomerate in aqueous media, making organic solvents the preferred choice. In particular, polar aprotic solvents with high electron pair donicity and low hydrogen-bonding parameters, such as N-methyl-2-pyrrolidone (NMP), N,N-dimethylformamide (DMF) and hexamethylphosphoramide (HMPA), have proven effective in forming stable CNT dispersions.[30] The effectiveness of these solvents is attributed to their ability to interact with the π-conjugated system of the CNTs to facilitate enhanced π-π orbital

doi:10.6342/NTU202502950

stacking and overlap.[31] Theoretical calculations further support the suitability of NMP and DMF, revealing favorable interaction geometries and charge-transfer characteristics that contribute to improved dispersion stability.[32]

In addition, mechanical treatment including high-power ultrasonication, ball milling, and shear mixing are commonly employed to facilitate the exfoliation and dispersion of CNTs.[33] However, the application of external mechanical forces may compromise the structural integrity of CNTs and introduce undesirable defects, which can negatively affect their electrical properties. Therefore, a careful balance must be struck between achieving effective dispersion and minimizing structural damage to preserve the intrinsic properties of CNTs. The dispersity of CNTs can be quantified by monitoring the maximum absorbance in UV-vis spectra, with well-dispersed individual CNTs typically exhibiting strong absorption between 200 and 300 nm.[34] Yu et al. reported that, by varying the sonication time, the absorbance peak increased progressively with longer sonication and eventually plateaued after approximately 50 minutes, indicating a dispersion limit beyond which further sonication had little effect.[35] Beyond solvent and mechanical treatments, surface functionalization offers an effective means to improve CNT dispersibility and interface interactions. Both covalent and non-covalent approaches

doi:10.6342/NTU202502950

have been widely employed to tailor CNT surfaces, and are further elaborated in the next two sections.

1.2.3. Covalent Functionalization for CNT Modification

Covalent surface functionalization of CNTs involves the introduction of reactive groups or modifier molecules onto their sidewalls or terminals, enabling tailored physicochemical properties and enhanced integration into functional systems.[36] These modulations can generally be categorized into two distinct approaches. As illustrated in **Figure 1.5**, these modifications generally follow two sequential strategies: The first strategy focuses on the direct attachment of primary functional groups to the CNT surface, creating reactive sites that facilitate subsequent chemical interactions.[37] The second strategy leverages these initial functional groups as anchoring points for covalent conjugation with polymers, small molecules, or advanced functional materials, thereby tailoring the CNT surface for targeted applications and enhancing compatibility with various matrices.

For introducing primary functional groups, acid treatment is the most frequently employed covalent chemical modification method to increase the chemical activity and hydrophilicity of CNTs. Employing nitric acid and/or sulfuric acid oxidized the nanotubes

doi:10.6342/NTU202502950

surface, forming hydroxyl, ester, carbonyl and nitro groups on the defect sites of the sidewall.[38] Such functionalization enhances the dispersibility of CNTs in aqueous solutions by converting their inherently hydrophobic surfaces into more hydrophilic ones through the introduction of polar functional groups. This modification increases the zeta potential and strengthens electrostatic stabilization, thereby improving colloidal stability in water.[39] Moreover, these oxygen-bearing groups are feasible for further derivatization, enabling subsequent functionalization with polymers, biomolecules, or other reactive species to tailor interfacial properties. Similar approaches involving halogenation,[40] radical addition[41] and thiolation,[42] have also been employed to introduce reactive sites onto CNT surfaces for enhanced chemical versatility and interfacial engineering.

Building upon these reactive functional groups, a broader range of surface modifications can be developed to further tailor the physicochemical properties of CNTs for a diverse application. Hamon et al. reported the synthesis of octadecyloxy- and octadecylamido- ester functionalized SWCNTs and the enhancement of solubility in common organic solvent with small bundles.[43] Qin et al. grafted SWCNTs with polystyrene (PS) with azide-functionalized PS ($–N_3$) via a cycloaddition reaction. This polymer functionalization significantly boosted the dispersion stability in dichlorobenzene, extending it from less than 10 minutes to over 5 months.[44] Gao et al.

doi:10.6342/NTU202502950

achieved the functionalization of MWCNTs with the hydrophilic polymer glycerol monomethacrylate (GMA) through atom transfer radical polymerization (ATRP) on oxidized MWCNTs, resulting the polymer-immobilized MWCNTs exhibited excellent dispersibility in polar solvents such as methanol, ethanol, DMSO, and DMF.[45] Apart from facilitating the exfoliation and dispersion of CNTs, covalently functionalized CNTs have also been widely applied in various fields, including biosensors, cellular interfaces, drug delivery systems.[46]

In the context of thermoelectric applications, covalent functionalization plays a pivotal role in tuning the electronic structure across CNT-based materials. For example, Zhou et al. reported that tuning the electronic structures of CNTs via different functional groups enables precise control over n- and p-type CNT thermoelectric performance by adjusting the blending ratio of amino- and carboxyl-functionalized CNTs.[47] Similarly, Lan and co-workers reported enhanced thermoelectric performance by incorporating hydroxyl and carboxyl functional groups that increased the Seebeck coefficient while reducing thermal conductivity.[48] While interfacial engineering has advanced significantly, research remains limited on the thermoelectric properties of CNTs that undergo secondary substitution reactions, wherein primary functional groups serve as reactive sites for additional chemical modifications. Nevertheless, this strategy presents

doi:10.6342/NTU202502950

a promising and underexplored avenue for achieving precise control over interfacial properties, with strong potential to significantly enhance thermoelectric performance in CNT-based materials.

To conclude this section, covalent functionalization modifies the intrinsic sp^2-hybridized carbon network of CNTs by introducing sp^3-hybridized sites through the formation of σ-bonds. This structural transformation enhances the macroscopic processability and dispersibility of CNTs in composite systems. However, the disruption of the delocalized π-conjugation inevitably results in a reduction of electrical performance.[33] This trade-off has motivated the exploration of alternative strategies, such as non-covalent surface modification, which aim to improve dispersion while preserving the structural and electronic integrity of CNTs.

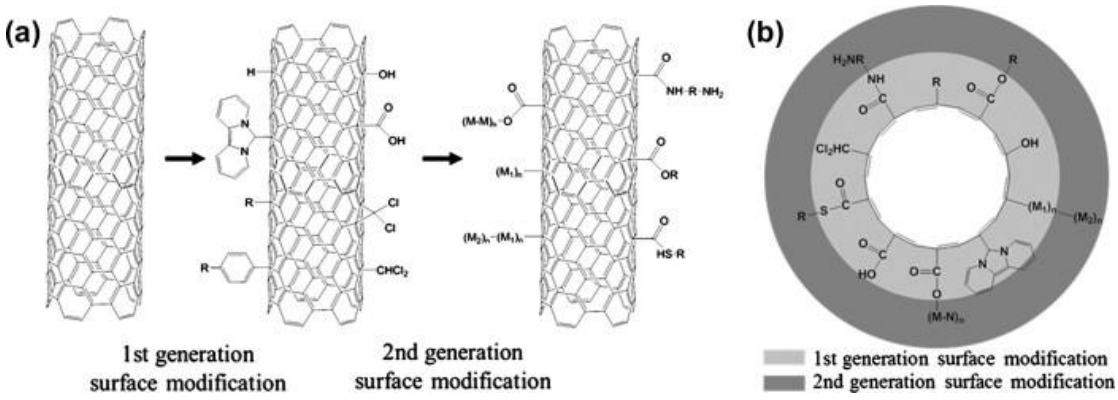

doi:10.6342/NTU202502950

Figure 1.5 Schematic illustration of typical covalent modifications on CNT surfaces, presented from (a) a side view and (b) a top view.[36b]

1.2.4. Surface Modification via Non-Bonding Interactions

In contemporary nanomaterial design, non-covalent surface modification strategies have emerged as a versatile toolkit for tailoring material interfaces. Techniques leveraging π–π stacking, hydrogen bonding, and electrostatic interactions enable adsorption of polymers, surfactants, or biomolecules onto nanomaterials without altering their core structure. This approach not only improves dispersion in solution but also modulates interfacial charge transport, making this approach especially beneficial for fabricating high-performance thermoelectric materials.

Surfactant molecules possess both hydrophobic and hydrophilic segments: the hydrophobic tails adhere to the CNT surface through van der Waals or π–π interactions, while the hydrophilic heads promote compatibility in aqueous environments. Molecular dynamics (MD) simulations have shown that sodium dodecylbenzene sulfonate (SDBS), a well-known anionic surfactant, wraps SWCNTs into an ordered multilayer structure, where the alkyl chains align closely with the CNT surface and the sulfonate groups extend outward, interacting with surrounding water molecules to stabilize the dispersion.[49] In

doi:10.6342/NTU202502950

addition, pristine p-type CNTs can be effectively converted to n-type through the introduction of the alkylammonium cationic surfactant cetyltrimethylammonium bromide (CTAB), driven by halide anion-induced electron transfer.[50] The long alkyl chains of CTAB further promote dispersion of CNTs in solution. By optimizing the CNT to CTAB ratio, a synergistic effect between charge carrier modulation and improved dispersion is achieved, resulting in a maximum power factor of 185.7 ± 8.5 μW m^{-1} K^{-2}.[51] Hata et al. reported the use of water-soluble gemini surfactants—comprising two surfactant-like moieties connected by a propylene spacer, as effective dispersants for CNTs. Specifically, gemini surfactants with tail lengths of eight or twelve carbon atoms (8-3-8 and 12-3-12) were investigated. Notably, the introduction of the gemini surfactant significantly enhances the number of conduction pathways for charge transport. Furthermore, the increased surface coverage not only improves thermoelectric performance but also enhances stability under ambient conditions, outperforming the conventional single-tailed counterpart surfactant.[52]

The incorporation of polymers into CNT matrices has attracted considerable attention due to their ability to improve CNT dispersion, enhance mechanical flexibility, and modulate electrical properties. Moreover, the intrinsically low thermal conductivity of polymers contributes to enhanced thermoelectric performance in CNT-based

doi:10.6342/NTU202502950

nanocomposites by suppressing heat transport while maintaining sufficient electrical conductivity. Poly(3,4-ethylenedioxythiophene) (PEDOT)-based materials have been among the most extensively studied polymers in thermoelectric research. With appropriate treatment, the power factor of PEDOT-based polymers can exceed 400 $\mu W\ m^{-1}\ K^{-2}$.[53] Yu et al. reported that PEDOT : PSS nanocomposites exhibit an ultralow thermal conductivity of 0.3 $W\ m^{-1}\ K^{-1}$, resulting in a *zT* value of 0.02 at room temperature.[54] Polyaniline (PANI) is another widely used conjugated polymer for forming nanocomposites with CNT matrices. Strong donor–acceptor interactions and π–π stacking between PANI and CNTs result in a tightly wrapped morphology, facilitating close interfacial contact.[55] The abundant PANI–CNT interfaces effectively scatter phonons and suppress lattice thermal conductivity, leading to a reported *zT* value of 0.12 at room temperature for a composite containing 64% SWCNTs.[56] Other conjugated polymers, including poly(3-hexylthiophene) (P3HT),[57] polypyrrole (PPy),[58] and various small molecules[59] have been extensively explored for their ability to enhance the thermoelectric performance of CNT-based nanocomposites. These non-covalent modification strategies enable precise tuning of interfacial interactions without compromising the intrinsic electronic structure of CNTs, while also contributing to reduced thermal conductivity through interface phonon scattering.

doi:10.6342/NTU202502950

1.3. Sugar-based Polymers

Sugar-based polymers represent a promising class of bio-derived materials due to their abundant natural resources**,** excellent biocompatibility, and high density of polar functional groups.[60] As illustrated in **Figure 1.6**, these polymers are broadly classified into three structural categories: Oligo- and polysaccharides, along with their derivatives such as cellulose, chitosan, maltotriose, and dextran, are naturally occurring biopolymers made up of monosaccharide units. Utilizing sugar-based resources also enables the production of a diverse array of cyclic monomers, including lactones, lactams, and both oxygen- and nitrogen-containing carboxyanhydrides.[61] In addition, sugar-linked polymers, in which sugars used as backbones or branch points, taking advantage of the multiple hydroxyl groups of sugars as attachment sites. Lastly, glycopolymers, where synthetic polymers bearing pendant sugar moieties, have been extensively studied across various architectures, including linear, star-shaped, and dendritic structures.[62]

doi:10.6342/NTU202502950

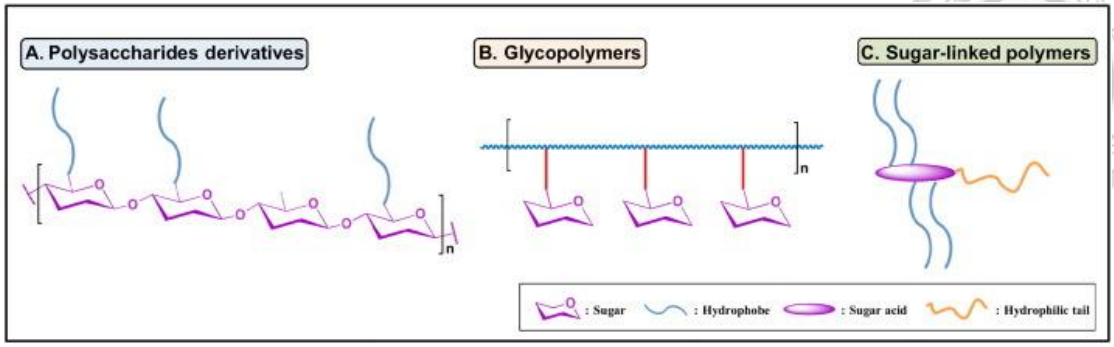

Figure 1.6 Schematic representation and classification of sugar-based polymeric systems.[62]

The incorporation of carbohydrates markedly influences surface affinity and molecular interactions at material interfaces. However, among these structures, block copolymers (BCPs) are specifically discussed separately from glycopolymers due to their distinct structural architecture and enhanced control over self-assembly and morphology.[63] The covalent bonding within BCPs effectively prevents the macro-scale phase separations that are commonly observed in polymer blends. The low degree of polymerization (N) and high Flory-Huggins interaction parameter (χ) of the sugar-based BCPs lead to strong segregation between different blocks.[64] Notably, self-assembled maltoheptaose-*block*-polystyrene (MH-PS) thin films fabricated using a solvent vapor annealing method can achieve periodic nanostructures on the sub 10-nm scale,[65] representing a cost-effective approach to enhancing lithographic precision beyond conventional methodologies.

doi:10.6342/NTU202502950

The precise control of BCP morphology is governed by various factors, including block composition, molecular weight, solvent environment, and processing conditions. Interestingly, the use of a cosolvent system, rather than a single solvent, provides an effective strategy for directing self-assembly. For instance, in the case of MH-PS, where the sugar block (MH) is water-soluble and the PS block prefers tetrahydrofuran (THF), adjusting the water/THF ratio significantly influences the resulting morphology. While single-solvent systems result in poorly ordered structures, introducing a cosolvent system with increasing THF content progressively improves the morphology. Specifically, at THF ratios below 80%, fingerprint-like patterns are observed, whereas a THF content of 80% leads to the formation of horizontally aligned cylindrical domains. This morphological transformation can be attributed to the differential affinities of the individual blocks for the vapor phase of the annealing solvent during processing.[66] Furthermore, as presented in **Figure 1.7**, Hung et al. reported that variations in block length and annealing time of maltoheptaose-*block*-polyisoprene (MH-PI) led to pronounced changes in the nanostructured morphologies of MH-PI thin films.[67] The alteration of sugar block also leads to diverse nanostructures; for instance, maltotriose-*block*-polystyrene (MT-PS), MH-PS, β-cyclodextrin-*block*-polystyrene (βCD-PS) thin films exhibit spherical domains, mixed cylindrical morphologies, and vertically aligned

doi:10.6342/NTU202502950

cylinders, respectively.[68] Through careful control of these parameters, the renewable and biodegradable sugar-based BCPs have demonstrated great potential as versatile materials for adjustable nanostructures in a wide range of applications, including field-effect transistors,[64a, 69] memory devices,[67, 70] and drug delivery systems.[71]

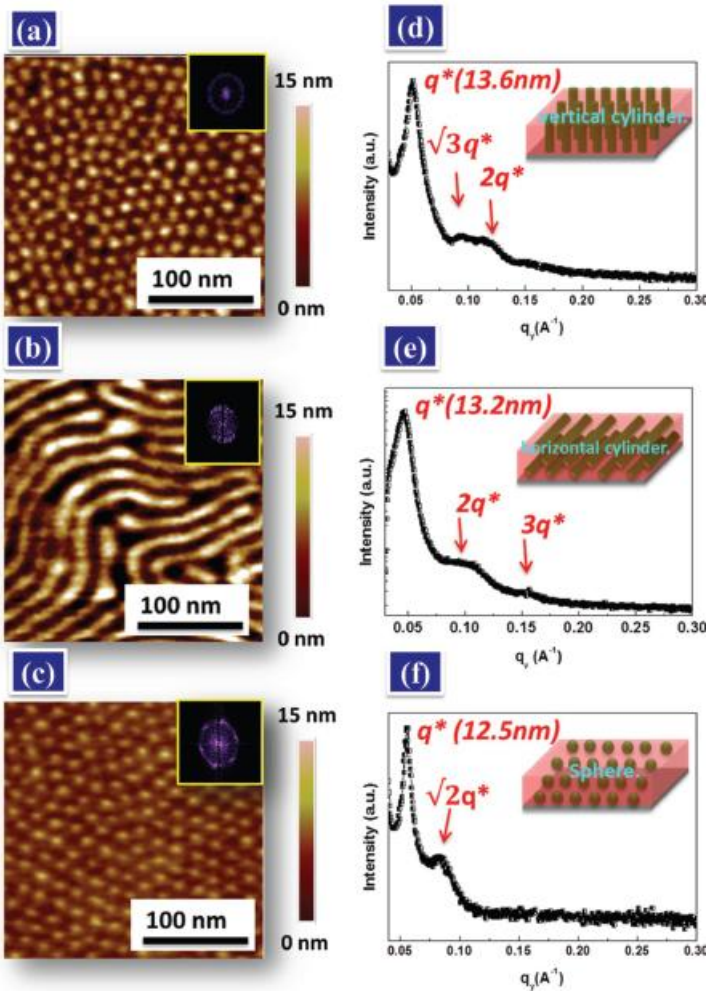

Figure 1.7 AFM topographies of (a) 8 h annealed, (b) 48 h annealed MH-$PI_{3.8k}$, and (c) 24 h annealed MH-$PI_{12.6k}$ thin films. 1D GISAXS profiles of (d) 8 h annealed, (e) 24 h annealed MH-$PI_{3.8k}$, and (f) 24 h annealed MH-$PI_{12.6k}$ thin films.[67]

doi:10.6342/NTU202502950

1.4. Research Motivation

The development of lightweight, flexible, and sustainable thermoelectric materials is critical for next-generation energy harvesting technologies, which aim to convert low-grade waste heat into electricity to power small-scale devices such as sensors and wearable electronics. CNTs have garnered significant attention due to their excellent electrical conductivity, mechanical strength, and inherent thermoelectric potential. Nevertheless, achieving stable dispersion and efficient charge transport in CNT-based composites remains a significant challenge. Sugar-based polymers provide a bio-based, environmentally friendly, and functionally versatile platform for interfacial engineering. Their abundant hydroxyl groups and structural diversity facilitate strong interactions with CNT surfaces, thereby enhancing dispersibility and rendering the materials suitable for solution-based processing techniques.

In the first study, CNTs were incorporated with sugar-based BCPs, MT-PS and MH-PS, which differ in their oligosaccharide and polystyrene block lengths. While earlier studies focused on microdomain formation via self-assembly, this work highlights the amphiphilic nature of sugar-based BCPs in enhancing interfacial interactions and dispersion. The hydroxyl-functionalized moiety demonstrates strong affinity toward polar

doi:10.6342/NTU202502950

solvents, while the hydrophobic polystyrene (PS) segment exhibits preferential binding to the CNT surface, thereby enhancing CNT dispersion in polar organic solvents. Moreover, by controlling the processing solvent and environment, provide the capability to induce p-n inversion without the use of molecular dopants, simplifying the fabrication processes. Optimizing nanocomposite components and controlling material polarity enables the fabrication of flexible thermoelectric generator (TEG) based on p-n junctions, as demonstrated in **Figure 1.8a**.

In contrast to the above study, which relied on the physical adsorption of sugar-based BCPs onto the CNT surface to aid dispersion, the second part of this research focuses on synthesizing sugar-functionalized CNTs via click reaction. By covalently attaching sugar moieties to the CNT surface, the multiple hydroxyl groups present in the oligosaccharide segments facilitate strong hydrogen bonding with aqueous solvent, significantly improving the colloidal stability of the functionalized CNTs. Anchored sugar chains on the CNT surface significantly reduce thermal conductivity, leading to improved *zT* and thermoelectric performance compared to pristine CNTs, as illustrated in **Figure 1.8b**.

Overall, the nanocomposite materials provide a compelling opportunity to optimize both the electrical and thermal transport properties in organic thermoelectric materials. Therefore, the integration of sugar-functionalized polymers with CNTs presents a

doi:10.6342/NTU202502950

promising strategy for designing efficient, sustainable, and processable thermoelectric nanocomposites.

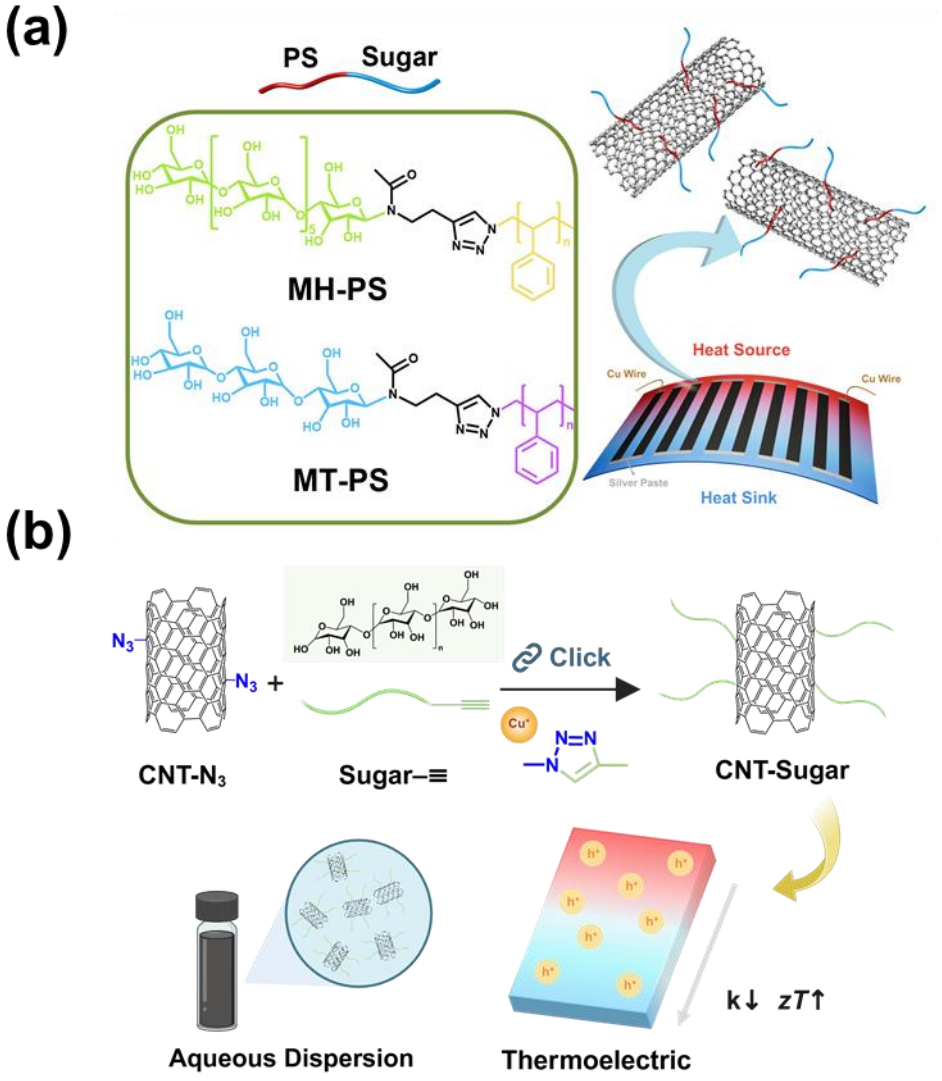

Figure 1.8 Strategic design framework of (a) Sugar-based BCP/CNT nanocomposites developed in this work for fabricating TEG. (b) Sugar-functionalized CNTs in aqueous dispersion and thermoelectric application.

doi:10.6342/NTU202502950

2. Experimental Section

2.1. Materials

The sugar-based BCPs maltoheptaose-*block*-polystyrene ($MH_{1.2k}$-*b*-$PS_{4.5k}$; MH-PS) and maltotriose-block-polystyrene ($MT_{0.6k}$-*b*-$PS_{2.1k}$; MT-PS) were synthesized through the copper-catalyzed azide-alkyne cycloaddition (CuAAC) method, as previously reported.[66b, 68] N-maltoheptaosyl-3-acetamido-1-propyne and alkyne-functionalized maltoheptaose (MH-C≡CH) was synthesized according to a previously reported method.[72] Similarly, N-maltotriosyl-3-acetamido-1-propyne (MT-C≡CH) was prepared using the same procedure. These sugar-based polymers are provided by Prof. Borsali's group, CNRS, France. Single-walled carbon nanotubes (SWCNTs) with a diameter of less than 2 nm and length greater than 5 μm (80% purity) were sourced from Tuball^{TM}. Carboxylated single-walled carbon nanotubes (CNTCOOH, XFS18), with a purity of 95%, a length ranging of 5-30 μm, and a diameter of 1-2 nm, were purchased from XFNANO.

11-Bromoundecyltrichlorosilane (BUTS, 97%, TCI), sodium azide (NaN_3, ≥99.0%, TCI), and N,N,N',N'',N''-pentamethyldiethylenetriamine (PMDETA, 98%, Macklin) were used as received. Copper(I) bromide (CuBr, 98%, Thermo Scientific) was purified

doi:10.6342/NTU202502950

by stirring in glacial acetic acid for 24 h at room temperature, followed by rinsing with ethanol and diethyl ether, and then drying overnight under vacuum.[73] N-methyl-2-pyrrolidone (NMP, anhydrous 99.5%), dimethylformamide (DMF, anhydrous, 99.8%) and toluene (anhydrous, 99.8%) were purchased from Sigma-Aldrich and used as received. All other reagents and solvents were used without further purification.

2.2. Synthesis of sugar-functionalized CNTs

Azide-functionalized CNTs (CNT-N_3) were first synthesized by modifying a method described in the literature.[74] Carboxylated CNTs (50 mg) were dispersed in 15 mL of toluene using a tip sonicator for 30 min. After sonication, the suspension was transferred to a 250 mL round-bottom flask. To this suspension, 250 μL (0.854 mmol) of BUTS was added, and the mixture was stirred for 18 h under a nitrogen atmosphere to prevent hydrolysis of the silane in ambient conditions. After silanization, the suspension was centrifuged at 6000 RPM for 5 min, and the supernatant was discarded. The silanized CNTs (CNT-silane) were then washed twice by redispersing in 10 mL of toluene, followed by centrifugation at 6000 rpm for 5 min to remove unreacted silane, amorphous carbon, and excess solvent. The silanized CNTs were subsequently dispersed in 20 mL of anhydrous DMF with excess NaN_3 (75 mg, 1.154 mmol) and stirred in an oil bath at

doi:10.6342/NTU202502950

65 °C overnight under a nitrogen atmosphere. After the reaction, the suspension was vacuum-filtrated to separate the CNT-N_3 from excess solvents and residues. The products were washed sequentially with 15 mL of DMF and 15 mL of ethanol three times, followed by drying under vacuum overnight to ensure complete removal of residual solvents.

Next, sugar-functionalized CNTs (CNT-MT and CNT-MH) were synthesized via a copper-catalyzed azide-alkyne cycloaddition click reaction. In a typical procedure, either CNT-N_3 and alkyne-functionalized maltotriose (0.6 g, 1.052 mmol), or CNT-N_3 and alkyne-functionalized maltoheptaose (1.2 g, 0.985 mmol), were dissolved in 20 mL of anhydrous DMF in a round-bottom flask. The reaction mixture was degassed via three freeze-pump-thaw cycles to ensure an oxygen-free environment. PMDETA (250 μL, 1.198 mmol) and CuBr (0.18 g, 1.255 mmol) were subsequently added, followed by an additional round of freeze-pump-thaw cycles. The reaction was then conducted under a nitrogen atmosphere at 65 °C with continuous stirring for 3 days to promote efficient coupling of the sugar moieties onto the CNT surface. Upon completion of the reaction, the mixture was vacuum-filtered to separate the sugar-functionalized CNTs from the reaction medium and residual reagents. The product was sequentially washed three times with DMF, ethanol, and THF to remove unreacted species and impurities. Finally, the products were dried under vacuum overnight to ensure complete removal of residual

doi:10.6342/NTU202502950

solvents.

2.3. Device Fabrication and Thermoelectric Characterization

2.3.1. Preparation and Measurement of Composites Thin Film

For fabricating sugar-based BCP/CNT thin films, MH-PS and MT-PS BCPs were individually dissolved in 3 mL of NMP or DMF at various weight ratios relative to CNTs (ratios of 2:1, 1:1, 1:2, and 1:3). A fixed amount of 1.5 mg of CNTs (at a concentration of 0.5 mg mL^{-1}) was then added to the BCP solution. Additionally, a pure CNT solution was prepared using the same procedure, but without the addition of BCP powder. As for the second part of the research, 3.0 mg of CNT, CNTCOOH, CNT-MT, and CNT-MH was dispersed in 3.0 mL of deionized water, yielding a dispersion concentration of 1.0 mg mL^{-1}. All the mixture were homogenized using a ball mill (Retsch MM440) set to 30 Hz for 15 min.

Glass substrates (7.5 × 15 mm) were sequentially cleaned in an ultrasonic bath using acetone, isopropanol, and deionized water, followed by surface activation via ozone plasma treatment. A 100 μL nanohybrid solution was drop-cast onto the substrates twice, and the moist films were dried under heat at 150 °C, 120 °C and 70 °C for NMP, DMF and water solution, respectively. The resulting nanohybrid films, with thicknesses ranging from approximately 2 to 6 μm as measured by a surface profiler (KLA Alpha-Step® D-

doi:10.6342/NTU202502950

300), were then annealed for 10 min before thermoelectric property measurement. For NMP (n-type) thin films, the drop-casting and heating were performed inside a nitrogen-filled glove box to prevent oxidation and moisture interference. In contrast, DMF, water (p-type) thin films were fabricated under ambient conditions.

The thermoelectric properties, including electrical conductivity and Seebeck coefficient, were measured at 303 K in a helium atmosphere using a commercial thermoelectric performance testing system (ZEM-3, ADVANCE RIKO Inc., Japan). Silver paste was applied to both ends of the films to ensure good electrical contact during the measurements. The in-plane thermal conductivity (κ) of the films was calculated using the equation $\kappa = \alpha C_p \rho$, where C_p and ρ denote specific heat capacity and film density, respectively.

2.3.2. Fabrication and Measurement of Thermoelectric Generator

The MH-PS/CNT and MT-PS/CNT nanocomposites with an optimized weight ratio of 1:2 were selected to fabricate the thermoelectric generator. DMF and NMP were used as solvents for the fabrication of the p-type and n-type legs, respectively. The thermoelectric legs were formed by drop-casting the solution onto a polyimide substrate, following the same procedure mentioned earlier. The films were then cut into rectangular shapes of 3 mm in width, 30 mm in length, and 5 μm in thickness. Each thermoelectric

doi:10.6342/NTU202502950

leg was subsequently adhered to a flexible polyethylene terephthalate (PET) substrate using double-sided tape. To create consecutive p-n junctions, conductive silver paint was applied, and five p-n junctions were connected in series. Copper wires were attached to ensure proper electrical contact and connected to an external circuit for measurement. The performance of the thermoelectric generator was tested using a custom-built system in an ambient environment. A water-cooling system was used to regulate the temperature at both the heat source and the heat sink. The heat source temperature was adjusted to create different temperature gradients, while the heat sink was maintained at a constant temperature of 298 K. The K-type thermocouples were attached to the surface of the thermoelectric generator to monitor the device's temperature using a Keithley DAQ 6510 multimeter system. The output voltage and short-circuit current were measured by connecting the copper wires with copper probes, using a Keithley 2182A nanovoltmeter and a Keithley 2400 sourcemeter, respectively.

2.4. Instruments

2.4.1. Characterization

Ultraviolet photoelectron spectroscopy (UPS) and X-ray photoelectron spectroscopy (XPS) were performed using a PHI 5000 VersaProbe III system (ULVAC-PHI, Inc.) under ultra-high vacuum conditions (6.7×10^{-8} Pa), with a monochromatic Al Kα X-ray

doi:10.6342/NTU202502950

source (1486.6 eV) as the excitation beam. Attenuated total reflection Fourier-transform infrared (ATR-FTIR) spectra were acquired using a Bruker Tensor 27 FTIR spectrophotometer at a resolution of 4 cm^{-1}, employing the KBr disk method. Ultraviolet-visible-near-infrared (UV-vis-NIR) spectra were recorded on a Hitachi U-4100 spectrophotometer with a resolution of 1 cm^{-1}. Raman spectroscopy was conducted using a Jobin Yvon LabRAM HR800 UV spectrometer equipped with an Nd:YAG laser (532 nm). Instrument calibration was carried out using a silicon (Si) substrate, exhibiting a characteristic Raman peak at 520.71 cm^{-1}. Thermogravimetric analysis (TGA) was conducted using a TGA 55 instrument (TA Instruments). Atomic force microscopy (AFM) was conducted using a Hitachi AFM5100N instrument operated in tapping mode under ambient conditions. Measurements were carried out with Hitachi SI-DF3PS probes, featuring a resonant frequency of 70 kHz and a force constant of 2.0 N m^{-1}. Field-emission scanning electron microscopy (FE-SEM) imaging was carried out using a Hitachi S-4800 microscope operated at an acceleration voltage of 10 kV. Transmission electron microscopy (TEM) was performed using a JEOL JEM-2100F instrument. Hall effect measurements were performed using an M91 FastHall™ system (Lake Shore Cryotronics, Inc.), with the final values averaged over 500 individual measurements. Thermal diffusivity coefficient (α) was determined using a Thermowave Analyzer TA (Bethel,

doi:10.6342/NTU202502950

Ishioka, Japan). Film density was determined from the measured weight and volume of the composite films. The C_p value was measured using a DSC instrument (DSC 25, TA Instrument), with the temperature ramp rate of 5 K min^{-1}. Sapphire was used as the calibration standard for accurate determination of C_p.

2.4.2. Computational Settings

The molecular dynamics (MD) simulations were conducted by using Nanoscale Molecular Dynamics (NAMD), a parallel molecular dynamics code designed for high-performance simulations. Non-bonding interactions were modeled using the 12-6 Lennard-Jones (L-J) potential for van der Waals forces, with a cutoff distance of 12 Å. The Lorentz-Berthelot mixing rule was applied to compute the L-J parameters between different atom types. Electrostatic interactions were calculated using the Coulomb potential, and long-range electrostatics were treated with the particle mesh Ewald (PME) method. The L-J parameters of all molecules were modeled using the CHARMM-based force field.[75] All simulation systems were generated and visualized in VMD.[76]

For sugar-based BCPs/CNT systems, CNT was constructed using VMD, and it was modeled with a (12,10) chirality, with a diameter of 1.5 nm and a length of 16 nm in the z-direction. The simulation box was defined with dimensions of 5 nm × 5 nm in the x-

doi:10.6342/NTU202502950

direction and y-direction, and 18 nm in the z-direction. The CNT was positioned at the center of the simulation box and remained fixed throughout the simulation. Four identical polymer molecules, either MH-PS or MT-PS, were positioned near the surface of the CNT in each simulation, with the molecules evenly spaced along the z-direction. The solvent, consisting of 4900 molecules of either NMP or DMF, filled the entire system.

The initial structure underwent the process of minimization for 30000 steps. Then, simulations were conducted in the isothermal-isobaric ensemble at 300 K and 1.01325 bar for 1500 ps to reach equilibrium. Data from the equilibrium state between 1250 and 1500 ps were selected for analyzing the wrapping behavior of MH-PS and MT-PS. The center of mass positions of the entire polymer, the hydrophilic end, and the hydrophobic end were calculated to measure their distances from the center of the CNT. The distance distributions between the atoms of the hydrophobic end and the CNT were calculated and plotted. All calculation considered only the projections on the x-y plane, ignoring the distance in the z-direction. A shorter distance from the center of the CNT indicates a more favorable wrapping behavior.

In the case of sugar-functionalized CNT systems, the CNT had a (12,10) chirality with a diameter of 1.5 nm and a length of 8.6 nm along the z-axis. The CNT was placed at the center of a rectangular simulation box with dimensions 80 Å × 80 Å × 110 Å and

doi:10.6342/NTU202502950

remained fixed throughout the simulations. All systems were filled with 23,600 TIP4P water molecules, yielding a density close to 1 g/cm^3. The four simulation systems were described as follows: CNT contained only the CNT and water. CNTCOOH contained the CNT, water, and ten formic acid molecules, with five molecules fixed near each side of the CNT sidewall. CNT-MT consisted of the CNT, water, and four MT molecules, symmetrically fixed near both sides of the CNT sidewall. CNT-MH was composed of the CNT, water, and four MH molecules, fixed in the same configuration as the MT molecules.

All simulations were performed under the Isothermal–Isobaric Ensemble (NPT). The initial configurations were first minimized for 60 ps. The systems were equilibrated and simulated at 300 K and 1 atm for 3000 ps. A time step of 1 fs was used throughout the simulations. Interaction energies between water and the carbon nanotube along with the associated functional molecules were calculated using the NAMD energy plugin in VMD. In this study, coordination numbers were determined by integrating the radial distribution function (RDF) curves up to a cutoff distance of R = 6 Å and 12 Å, using the trapezoidal rule to numerically evaluate the integral.

doi:10.6342/NTU202502950

3. Design of Sugar-Based Block Copolymer/Carbon Nanotube Nanocomposites for Thermoelectric Applications

3.1. Brief Introduction

In this study, two distinct oligosaccharide-based block copolymers (BCPs) are selected for their promising properties: maltotriose-*block*-polystyrene (MT-PS) and maltoheptaose-*block*-polystyrene (MH-PS). These BCPs are blended with CNTs to enhance their thermoelectric (TE) performance through improved CNT dispersion. Furthermore, the fabrication process strategically employs the solvents *N*,*N*-dimethylformamide (DMF) and *N*-methyl-2-pyrrolidone (NMP) under various processing conditions to produce p- and n-type TE nanocomposites. The polarity changes induced by each solvent system are confirmed by X-ray photoelectron spectroscopy (XPS), ultraviolet photoelectron spectroscopy (UPS), and Raman spectroscopy. The nanostructure and morphology are further characterized by atomic force microscopy (AFM) and scanning electron microscopy (SEM). Additionally, a flexible thermoelectric generator (TEG) is constructed from the optimized nanohybrids by connecting five pairs of as-fabricated p-n junctions in series. This device achieves a maximum open-circuit voltage of 17.28 mV and a maximum power output of 133.90 nW under a 25 K

doi:10.6342/NTU202502950

temperature gradient. Overall, this study introduces an innovative approach for the fabrication of p- and n-type TE nanocomposites through solvent-mediated control, and represents the first application of sugar-based BCPs in organic TE materials, thereby highlighting their potential for flexible and sustainable energy solutions.

3.2. Results and Discussion

3.2.1. Preparation and Measurement of Composites Thin Film

The chemical structure of sugar-based BCPs and the fabricating procedures of the composites are presented in **Figure 3.1**. A series of sugar-based BCPs consisting of MT-PS and MH-PS is employed to improve the dispersion of CNTs in solution. These amphiphilic BCPs possess both hydrophobic polystyrene (PS) segments that interact with the CNT surface and hydrophilic maltose sugar moieties that enhance solvent compatibility, and their syntheses have been reported in the literature.[68, 77] The choice of solvent is crucial, as it must simultaneously ensure good solubility for the amphiphilic BCPs and promote efficient CNT dispersion. Amphiphilic BCPs are known for the selective solvent compatibility of their distinct blocks, and cosolvents have been used in previous studies to enhance the solubility of sugar-based BCPs.[66b, 71, 77] The oligosaccharide component of these BCPs, with multiple hydroxyl groups, forms

doi:10.6342/NTU202502950

extensive hydrogen bonds with water, which makes water a preferred solvent (**Figure 3.2a**). However, the use of water as a solvent induces p-type charge transfer in CNT systems.[25] Therefore, when mixing water with n-type solvents, it compromises the n-type TE performance. Consequently, rather than employing cosolvents, it is crucial to select a solvent that can dissolve sugar-based BCPs while preserving the desirable TE properties of the CNT system. This work has tested several common organic solvents, such as, acetone, propanol, and ethylene glycol. The result in **Figure 3.2b** found them to be ineffective at dissolving sugar-based BCPs, while NMP and DMF effectively dissolve the BCPs. This difference in solubility arises from the pronounced disparity in hydrophilicity and hydrophobicity between the oligosaccharide and PS blocks. As a result, the solvent polarity and Hildebrand solubility parameters must be carefully considered in solvent selection. Thus, the amide-based solvents NMP and DMF are distinguished from other solvents by their high polarity indices of 6.7 and 6.4, respectively.[78] which facilitate the dissolution of malt sugar. Experimental data confirm that maltotriose and maltoheptaose are highly soluble in both NMP and DMF (**Figure 3.2a**). Additionally, according to Hildebrand's theory, polymers tend to dissolve in solvents with similar solubility parameters.[66a] PS is soluble in DMF due to the proximity of the respective Hildebrand solubility parameters, at 22.5 and 24.9, respectively.[79] The solubility

doi:10.6342/NTU202502950

parameter (δ) of DMF (δ_{DMF} = 24.9 $MPa^{1/2}$) is also close to that of NMP (δ_{NMP} = 23.0 $MPa^{1/2}$), making both solvents suitable for dissolving the PS component.[80]

Various solvents have been explored for their ability to solubilize and disperse CNT aggregates. Polar aprotic solvents with high electron pair donicity and low hydrogen-bonding parameters, such as DMF, hexamethylphosphoramide (HMPA), and NMP, have demonstrated efficacy in forming stable dispersions of single-walled carbon nanotubes (SWCNTs) by various dispersion methods.[30] The effectiveness of these solvents is attributed to their ability to interact with the π-conjugated system of the CNTs to facilitate enhanced π-π orbital stacking and overlap.[31] Given the large specific surface area of CNTs, their electronic properties, including energy levels and local density of states, are highly sensitive to the surrounding chemical environment.[81] As a result, the selection of solvent for CNT dispersion significantly affects the TE properties.[49, 82] When CNTs are processed with polar aprotic solvents such as DMF and NMP, the unshared electron pairs from adsorbed solvent molecules are transferred to the CNTs, which results in a transition from p-type to n-type behavior. Conversely, CNT dispersions in nonpolar or polar protic solvents tend to retain positive Seebeck coefficients, thereby maintaining their p-type characteristics.[25]

Considering all factors, NMP and DMF are the more favorable solvents for the

doi:10.6342/NTU202502950

preparation of sugar-based BCP/CNT nanocomposites. Importantly, for the construction of TEGs, both p-type and n-type materials are required. While NMP and DMF exhibit n-type behavior when processing is carried out in a nitrogen-filled glove box to exclude water and oxygen, the TE behavior can be tuned by adjusting the processing environment, as shown in **Figure 3.3**. On the contrary, under ambient conditions, the as-prepared CNT nanocomposites exhibit p-type thermoelectric characteristics due to the electron-withdrawing effect of oxygen molecules adsorbed on the CNT surface.[83] Notably, NMP demonstrates a stronger tendency for electron injection into CNTs compared to DMF.[84] Thus, this work employs NMP as a solvent under inert glove box conditions to fabricate n-type composites, while p-type composites are produced using DMF under ambient conditions, where oxygen exposure promotes hole conduction. As demonstrated by the C 1s XPS spectra in **Figure 3.4**, the shift to lower binding energy indicates an increased transfer of electrons to the carbon atoms. Thus, NMP facilitates a greater transfer of electrons to the carbon atoms on the CNT surface, resulting in a lower binding energy compared to DMF. This shift reflects a transition in charge-carrier properties from hole-dominated (p-type) to electron-dominated (n-type), confirming the n-type characteristics of CNTs processed with NMP in a glove box. Therefore, by strategically selecting the solvent and processing environment, both p-type and n-type thermoelectric composites

doi:10.6342/NTU202502950

can be produced from the same BCP/CNT system.

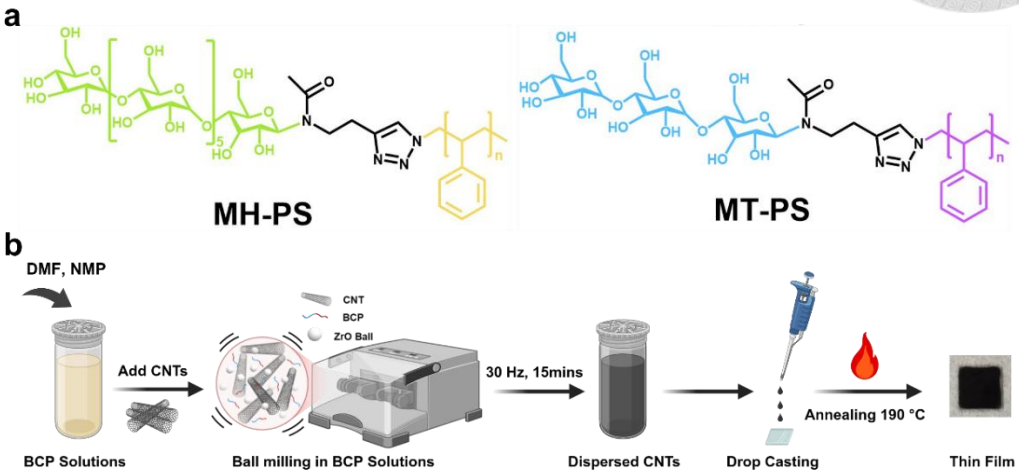

Figure 3.1 (a) Chemical Structures of sugar-based block copolymers MH-PS and MT-PS. (b) The fabrication process of BCP/CNT nanocomposite films.

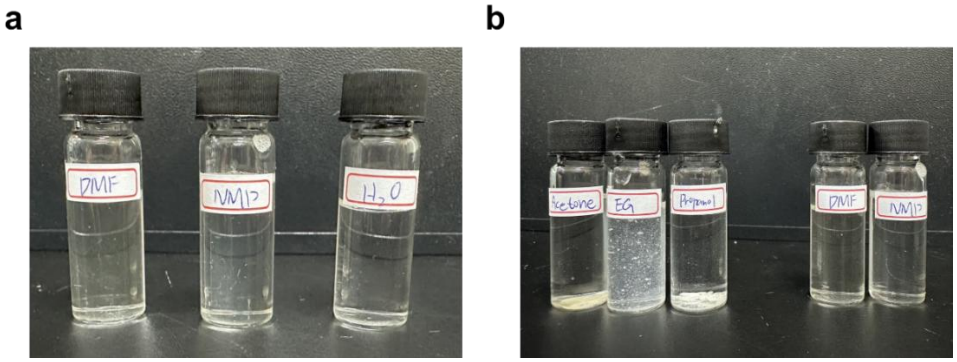

Figure 3.2 Solubility test in different solvents for sugar-based polymers. (a) MH shows high solubility in high polar solvents DMF, NMP and water. (b) MH-PS in different organic solvents.

doi:10.6342/NTU202502950

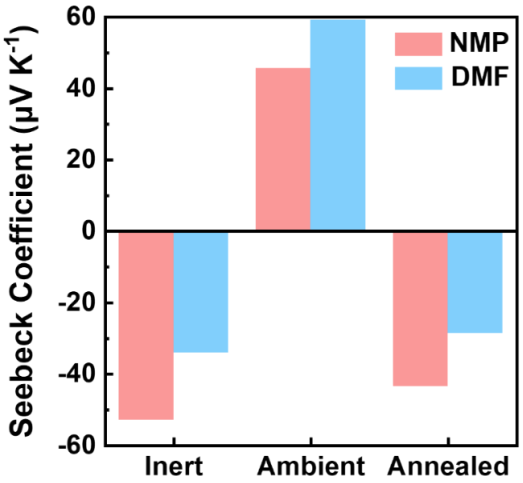

Figure 3.3 Seebeck coefficients of MH-PS/CNT nanocomposites under different processing environments using NMP and DMF. The inert environment was processed in a nitrogen-filled glove box. The annealed films were first processed in ambient conditions (298 K, RH = 50%), then annealed at 190˚C for 10 minutes in a nitrogen-filled glove box.

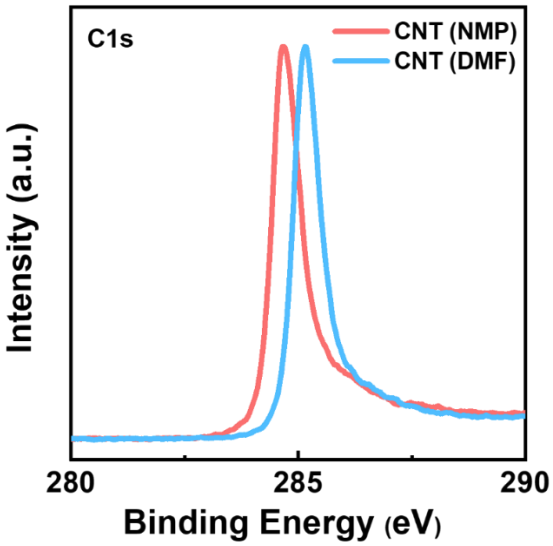

Figure 3.4 XPS C1s spectra. Pristine CNT prepared in NMP and DMF solvent.

doi:10.6342/NTU202502950

3.2.2. Theoretical simulation of sugar-based BCP/CNT composites

The theoretical simulation of BCP/CNT nanocomposites reveals critical insights into the configurational behavior of sugar-based BCPs and their interaction with CNTs. In this study, geometrical optimization of the BCPs was conducted using density functional theory (DFT) at the B3LYP/6-311G(d,p) level. To reduce computational costs, some repetitive PS units were omitted while preserving the original monomer ratio for MH-PS and MT-PS, corresponding to 7 and 3 styrene monomers, respectively. The optimized sugar-based BCP structures are detailed in **Figure 3.5**. Next, molecular dynamics (MD) simulations were performed using the Nanoscale Molecular Dynamics (NAMD) simulation package to investigate the wrapping behavior of sugar-based BCPs around the CNTs. The results in **Figure 3.6a** clearly confirm that the CNTs exhibit a stronger affinity for the hydrophobic PS block than for the hydrophilic oligosaccharide moiety in both DMF and NMP. The quantitative analyses in **Figure 3.6b and c** reveal the spatial relationships between the PS block and the center of mass of the CNTs for both MH-PS and MT-PS, indicating that the longer PS block of the MH-PS system positions the PS closer to the CNT surface than the shorter MT-PS system. A previous investigation employing an empirical MM+ force field obtained similar results, where an increase in the number of PS monomer units resulted in a decrease in the distance between PS and

doi:10.6342/NTU202502950

the CNT.[85] This proximity correlates with enhanced interfacial interactions by facilitating the formation of π–π stacking interactions between the aromatic rings of PS and the CNTs.[86] Notably, solvent effects are negligible for the MH-PS system, where significant variations in the PS-CNT distances are not observed across different solvent environments (**Figure 3.6b**). In contrast, for MT-PS, the PS chains exhibit longer distances to CNTs, with solvent choice noticeably impacting the spatial organization of the PS block (**Figure 3.6c**). This difference arises because longer MH-PS chains establish stronger, more stable interactions with CNTs, this steric stabilization resist changes induced by solvents. Conversely, the shorter MT-PS chains, with fewer anchoring points and increased conformational flexibility, exhibit a spatial organization that is markedly more responsive to variations in solvent quality.[87]

In contrast to the non-polar solvent benzene (BEN), the high-polarity solvents NMP and DMF exhibit different interaction dynamics. The role of the solvent in modulating the polymer behavior is elucidated by the polymer-solvent interaction parameter (χ), which is presented in **Table 3.1**. Here, a larger χ value indicates stronger repulsive interactions, while a smaller χ value suggests more favorable or attractive interactions between the polymer and solvent. Thus, DMF, with the highest χ value for the PS block, exhibits a stronger tendency for PS adhesion to the CNTs rather than relaxation (**Figure**

doi:10.6342/NTU202502950

3.6a), thus resulting in the shortest PS-CNT distance in the MT-PS system. Conversely, benzene, characterized by the lowest χ value for the PS block and the highest χ value for the sugar block, leads to the greatest separation between PS and CNT, reflecting weaker interactions due to competition between benzene and CNTs for the PS block. These results demonstrate the profound influence of polymer-solvent interactions on the BCP/CNT interfacial dynamics. The thermodynamic driving forces shaped by the solvent-polymer interaction parameters govern the molecular configurations and determine the interfacial distances, offering critical insights for tailoring nanocomposite properties in solvent-specific environments.

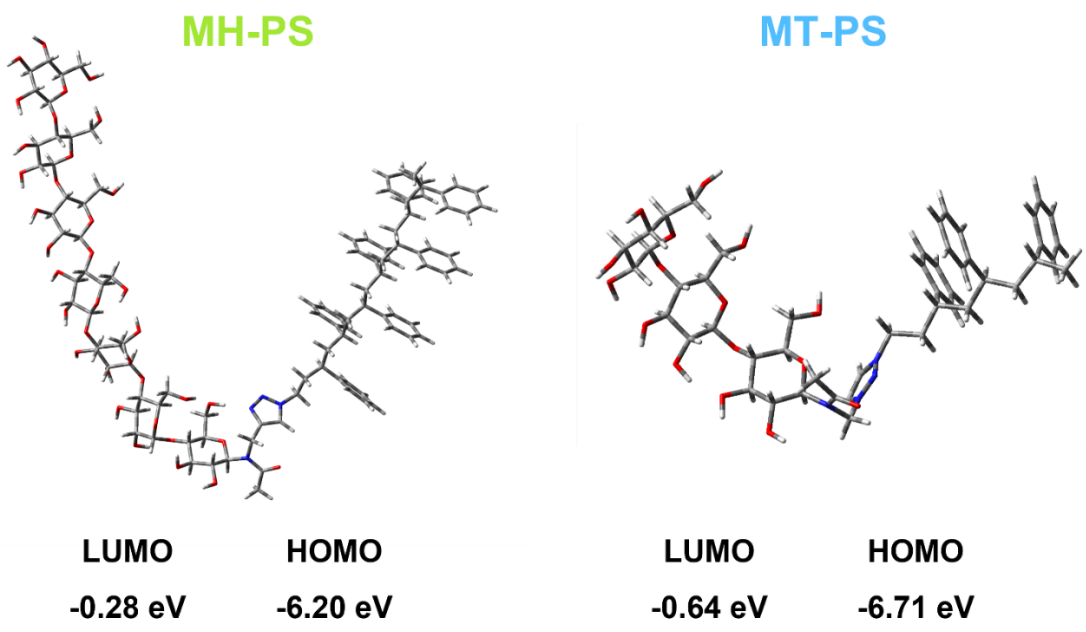

Figure 3.5 DFT calculation of MH-PS and MT-PS (omitted some repeated polystyrene units): optimized geometries and energy levels.

doi:10.6342/NTU202502950

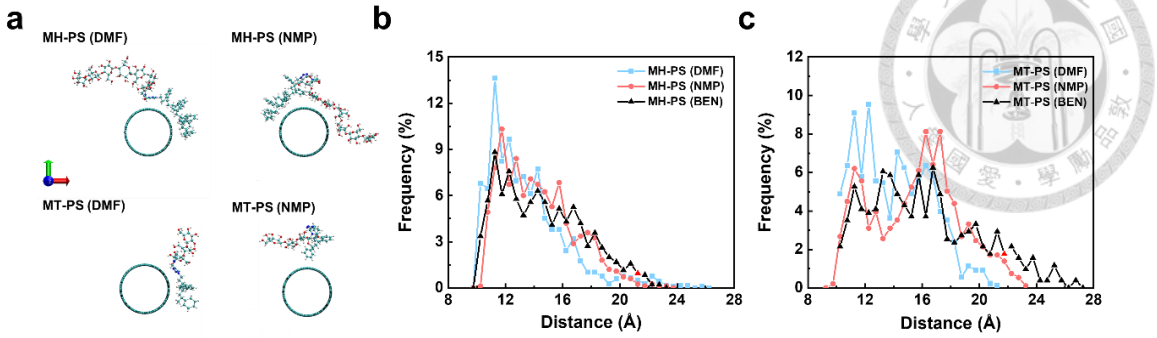

Figure 3.6 Molecular dynamics simulation. (a) Snapshots of a polymer chain interacting with CNT in DMF and NMP solvent. Analysis of distance between polystyrene block and center of mass of CNT for (b) MH-PS (c) MT-PS in DMF, NMP and benzene solvents.

Table 3.1 Theoretical calculation of the Flory-Huggins interaction parameter (χ) between different polymer blocks and solvents at 298 K, performed by Material Studio.

Monomer	Solvent	#1	#2	#3	#4	#5	Avg
Styrene (PS)	DMF	2.068	2.089	2.050	2.051	2.008	**2.053**
	NMP	1.062	1.074	0.983	1.004	1.154	**1.055**
	Benzene	0.379	0.377	0.379	0.361	0.342	**0.368**
Maltoheptaose (MH)	DMF	0.926	0.500	0.524	0.966	0.896	**0.763**
	NMP	2.155	1.776	2.285	1.631	1.603	**1.890**
	Benzene	3.814	4.457	4.651	4.364	4.762	**4.410**

doi:10.6342/NTU202502950

3.2.3. Thermoelectric performance of sugar-based BCP/CNT composites

The TE performance of the as-prepared MH-PS/CNT nanocomposite films with various mass ratios (2:1 to 1:3) and a fixed CNT concentration of 0.5 mg mL^{-1} is summarized in **Figure 3.7a–c** and **Table 3.2**. Here, the pristine CNT films exhibit electrical conductivity (σ) values of 572.08 ± 161.30 S cm^{-1} in NMP and 564.17 ± 193.78 S cm^{-1} in DMF. In the case of the MH-PS composite, the electrical conductivity tends to increase as the insulating MH-PS decreases in both solvent systems. However, the conductivity plateaus at an MH-PS:CNT weight ratio of 1:2 in the NMP solvent. In the DMF solvent, however, the electrical conductivity decreases at a weight ratio of 1:3, which suggests that an optimal amount of sugar-based BCP is necessary to aid CNT dispersion and enhance the charge carrier pathways. This hypothesis is further supported by examining the morphology of each nanocomposite. Seebeck coefficient (*S*) specifically relates to the transport of energetic charge carriers. Hence, the DFT calculations in **Figure 3.5** are used to explore the endowment of a large bandgap in the sugar-based BCPs. When incorporated into the CNT composite, the insulating component introduces barriers to charge transport between CNTs. In this respect, the variable-range hopping (VRH) model can be used to explain how charge carriers traverse thin barriers,

doi:10.6342/NTU202502950

such as tube-tube junctions and tube-polymer interfaces, via a hopping mechanism.[88] This model accounts for the dominance of energetic carriers in the transport process in heterogeneous systems, which leads to an increase in the Seebeck coefficient due to the selective favorable transport of higher-energy carriers. Consequently, the incorporation of MH-PS into the CNT matrix enhances the absolute Seebeck coefficient, yielding values of –54.68 ± 3.80 and 63.54 ± 5.10 μV K^{-1} in NMP and DMF, respectively, compared to values of –49.70 ± 1.14 and 52.47 ± 11.19 μV K^{-1} for the pristine CNTs. The results in **Figure 3.7b** indicate that the Seebeck coefficient also decreases as the proportion of MH-PS decreases in the case of the p-type solvent (DMF). This observation aligns with the VRH hopping model, where reducing the insulating component lowers the absolute value of the Seebeck coefficient. Although this trend is not evident in the NMP system, the optimized Seebeck coefficient still achieves a moderate value of –54.68 ± 3.80 μV K^{-1} at a weight ratio of 1:2.

For a comprehensive evaluation, the power factor (*PF*) at each weight ratio is calculated by multiplying the square of the Seebeck coefficient by the electrical conductivity, as shown in **Figure 3.7c**. In the NMP system, the pristine CNT film exhibits a *PF* of 140.63 ± 37.19 μW m^{-1} K^{-2}, while the optimized MH-PS/CNT hybrid with a 1:2 weight ratio reaches a *PF* of 175.07 ± 40.73 μW m^{-1} K^{-2}. Similarly, the pristine CNT film

doi:10.6342/NTU202502950

processed in DMF solvent exhibits a *PF* of 147.06 ± 39.82 μW m^{-1} K^{-2}, whereas the optimized MH-PS/CNT composite in DMF achieves a *PF* of 181.34 ± 46.95 μW m^{-1} K^{-2}. Contrary to expectations, the introduction of the insulating sugar-based BCP does not degrade TE performance; rather, it enhances it when an optimal ratio of the sugar-based BCP is incorporated. The insulating component must contribute positively to the composite without overwhelming the conductive pathways, thereby enhancing the overall thermoelectric efficiency. Compared to MH-PS, MT-PS is expected to interact less effectively with both the CNT surface and the solvent because it contains only three maltose sugars and has a shorter PS block. Nevertheless, the results in **Figure 3.7d and f** show that the MT-PS/CNT nanocomposites perform well in both solvents, achieving slightly lower *PF* values of 162.70 ± 27.88 and 174.09 ± 27.58 μW m^{-1} K^{-2} in NMP and DMF, respectively.

In addition to the Seebeck coefficient and electrical conductivity, the thermal conductivity (κ) is a critical factor in determining the TE performance of materials. The thermal conductivity consists of two components, namely: the electronic contribution (κ_e), governed by the Wiedemann-Franz law ($\kappa_e = LT\sigma$), where L is the Lorenz number and T is temperature, while the lattice contribution (κ_L) relates to the periodic structure and phonon transport. Because κ_e is proportional to the electrical conductivity, the pristine

doi:10.6342/NTU202502950

CNTs, which are known for their high electrical conductivity, also exhibit high thermal conductivity compared to polymer materials. Moreover, the low mass of carbon atoms, strong covalent C–C bonds, and low anharmonicity of the lattice make the CNTs particularly efficient in phonon transport, thereby contributing to their inherently high lattice thermal conductivity (κ_L).[89] However, the high thermal conductivity of the CNTs makes them less suitable for TE applications, where a low thermal conductivity is desirable to maintain temperature gradient and enhance the figure of merit (zT).[90] As shown in **Figure 3.7e and g**, pristine CNT thin film exhibits thermal conductivity values of 15.56 W m^{-1} K^{-1}. For materials with low electrical conductivity, such as polymers and nanocomposites, κ_e contributes minimally to the overall thermal conductivity, thus making the reduction of κ_L more critical. Incorporating a sugar-based BCP into the CNT matrix successfully lowers the overall thermal conductivity due to the inherently low κ value of the BCP and the interfacial phonon scattering that arises at the polymer-CNT interface. For the MH-PS/CNT and MT-PS/CNT composites with a 1:2 weight ratio, the in-plane thermal conductivities κ are decreased to 6.04 and 9.87 W m^{-1} K^{-1}, respectively. This significant reduction in κ results in improved zT value of 8.78×10^{-3} and 4.99×10^{-3} compared to 2.74×10^{-3} for the pristine CNT films in NMP solvent, as shown in **Figure 3.7e**. Wherein p-type system, **Figure 3.7g** also demonstrates the increased zT value of

doi:10.6342/NTU202502950

9.10×10^{-3} and 5.34×10^{-3} for MH-PS and MT-PS, respectively. Notably, the MT-PS/CNT hybrids exhibit slightly higher thermal conductivity than the MH-PS/CNT hybrids, likely due to differences in polymer structure, as supported by the following comparative analyses. Spin-coated polymer thin films of MH-PS and MT-PS were prepared, and the AFM images in **Figure 3.8** reveals that MH-PS film exhibits a higher pore density, albeit with smaller pore sizes compared to MT-PS, creating a high density of interfaces that enhance phonon scattering at pore boundaries and thereby further reduce the thermal conductivity.[91] It is worth noting that MH-PS/CNT composites achieve higher *zT* values than MT-PS/CNT composites in both NMP and DMF solvents, which underscores the effectiveness of MH-PS in improving the thermoelectric *zT* value through its lower thermal conductivity.

doi:10.6342/NTU202502950

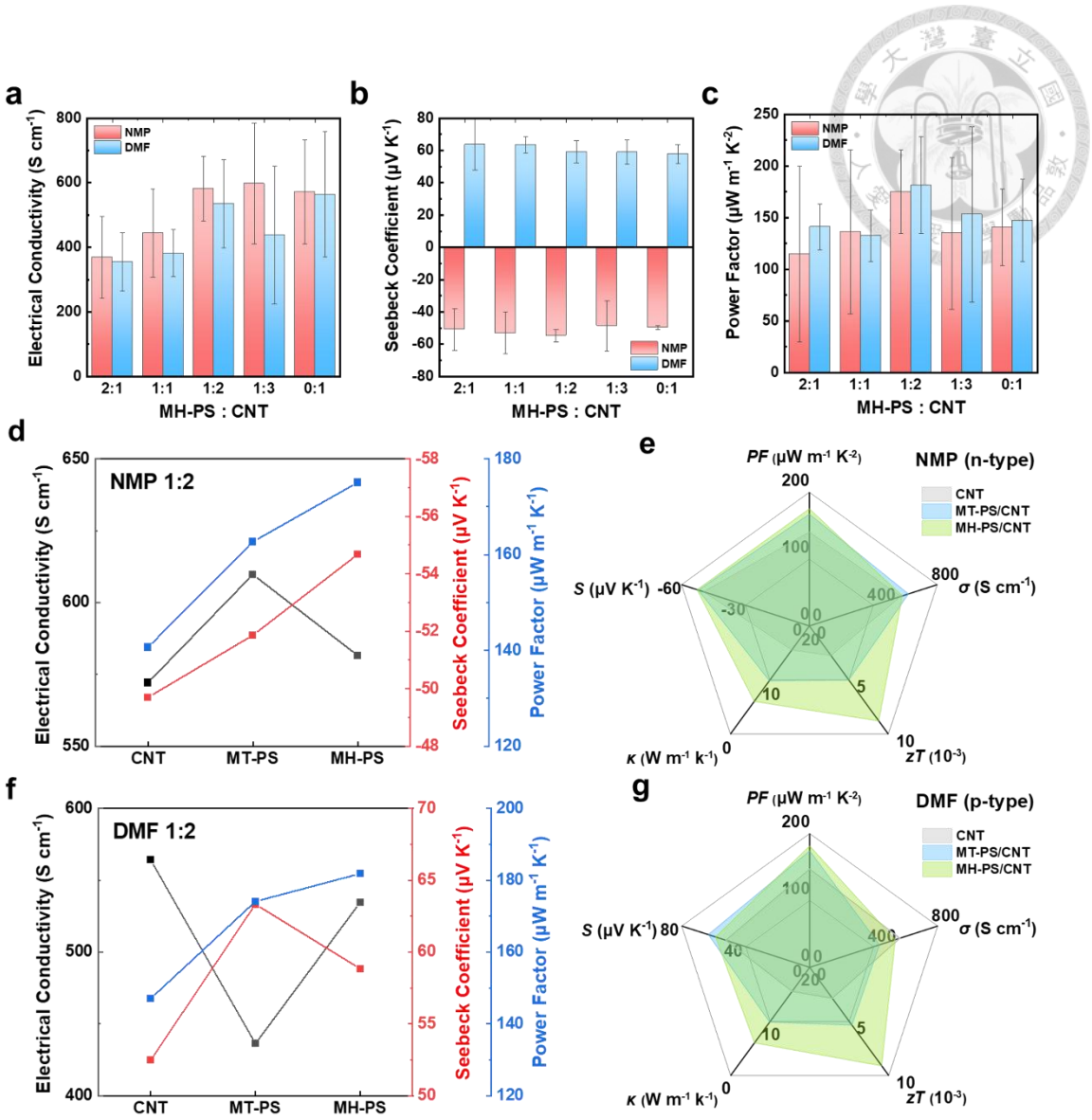

Figure 3.7 (a) Electrical conductivity, (b) Seebeck coefficient and (c) Power Factor of MH-PS/CNT nanocomposites. Comparative analysis of thermoelectric performance of CNT and optimized ratio 1:2 of sugar-based BCP/CNT nanocomposites prepared in (d-e) NMP (f-g) DMF solvent.

doi:10.6342/NTU202502950

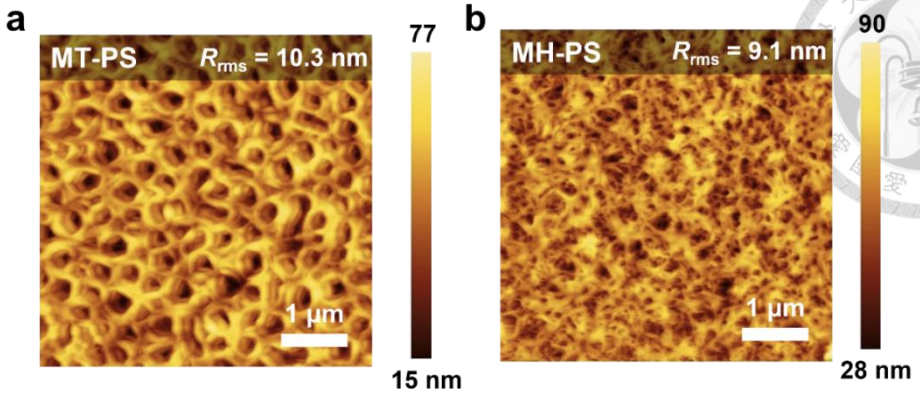

Figure 3.8 AFM images of spin-coated sugar-based BCP. (a) MT-PS (b) MH-PS thin films.

Table 3.2 Thermoelectric characteristics of BCP/CNT nanocomposites.

Nanocomposite	***σ*** [S cm^{-1}]	***S*** [μV K^{-1}]	**Power Factor** [μW m^{-1} K^{-2}]
CNT (NMP)	572.08 ± 161.30	-49.70 ± 1.14	140.63 ± 37.19
MH-PS : CNT (2:1) (NMP)	368.27 ± 127.30	-50.90 ± 12.88	114.64 ± 84.9
MH-PS : CNT (1:1) (NMP)	444.55 ± 136.99	-52.99 ± 12.80	136.23 ± 79.19
MH-PS : CNT (1:2) (NMP)	581.55 ± 100.92	-54.68 ± 3.80	175.07 ± 40.73

doi:10.6342/NTU202502950

MH-PS : CNT (1:3) (NMP)	597.76 ± 186.79	-48.60 ± 15.55	134.73 ± 73.53
MT-PS : CNT (1:2) (NMP)	609.77 ± 123.20	-51.86 ± 3.57	162.70 ± 27.88
CNT (DMF)	564.17 ± 193.78	52.47 ± 11.19	147.06 ± 39.82
MH-PS : CNT (2:1) (DMF)	355.38 ± 89.81	63.54 ± 5.10	141.07 ± 22.10
MH-PS : CNT (1:1) (DMF)	381.43 ± 72.92	59.22 ± 6.85	132.41 ± 25.23
MH-PS : CNT (1:2) (DMF)	534.56 ± 136.69	58.84 ± 7.51	181.34 ± 46.95
MH-PS : CNT (1:3) (DMF)	437.81 ± 212.91	57.71 ± 5.92	153.00 ± 84.79
MT-PS : CNT (1:2) (DMF)	436.26 ± 81.49	63.33 ± 2.65	174.09 ± 27.58

doi:10.6342/NTU202502950

3.2.4. Spectroscopic properties of sugar-based BCP/CNT composites

The interactions between BCP and CNTs in the nanocomposite are investigated using Raman spectroscopy at an excitation at a wavelength of 532 nm, as illustrated in **Figure 3.9, a and b**. The spectra clearly show the characteristic D-band at around 1345 cm^{-1}, which is associated with defect-induced scattering, along with the G-band, which is linked to the vibrational modes of sp^2 carbon atoms. The G-band comprises two components: the lower-frequency G^-, which corresponds to circumferential vibrations, and the higher-frequency G^+, which corresponds to axial vibrations along the nanotube axis.[92] Importantly, the absence of any new Raman peaks after combining the BCP with CNTs suggests that the two components interact physically without the formation of new chemical bonds. Additionally, the low D-band intensities and D/G ratios in the composite films indicate that the CNT structure remains largely intact after incorporating the BCP, which is essential for preserving their intrinsic electronic properties within the nanocomposites. The Raman spectra also reveal solvent-dependent shifts in the G-band. In the NMP solvent (n-type), the G-band demonstrates a bathochromic shift towards lower wavenumbers relative to the DMF solvent (p-type) across both investigated composite systems, which provides spectroscopic evidence elucidating the electronic environment in the NMP system. This shift indicates that charge transfer between the

doi:10.6342/NTU202502950

CNTs and BCP is affected by the choice of solvent, which aligns with previous studies showing that such shifts in vibrational properties can occur when charge transfer is significant.[82b, 93]

In addition, the energy levels of the composites are elucidated by the UPS results in **Figure 3.9c**. Here, the work function of pristine CNTs exhibits solvent-dependent behavior, with values of 4.33 and 4.48 eV in NMP and DMF, respectively. The shallower work function in the NMP system facilitates electron transfer to the CNTs, whereas the deeper work function in DMF promotes electron transfer from the CNTs to the solvent medium. These results align with the above XPS and Raman spectroscopy data, further validating the considerable effect of the selected solvent on the electronic structures and energy levels of the nanocomposites, thereby influencing the charge carrier polarity.

The electrical properties of the BCP/CNT nanocomposite films are further revealed by the Hall effect measurements in **Table 3.3**. Consistent with the above observations, all samples processed in NMP exhibit n-type behavior, thus confirming electrons as the majority carriers, while those processed in DMF retain p-type characteristics, indicating holes as the majority carriers. In addition, the introduction of BCPs into the CNT matrix results in a reduction in charge-carrier concentration, accompanied by a slight increase in carrier mobility. This phenomenon is attributed to the insulating nature of the BCPs,

doi:10.6342/NTU202502950

which introduce charge barriers within the composite system. These barriers facilitate scattering events, which enable higher-energy carriers to traverse the polymer-CNT interfaces preferentially.[94] According to the Mott forumla, the Seebeck coefficient is inversely correlated with the charge-carrier concentration, whereby increased carrier concentrations lead to more frequent scattering events, thereby reducing the energy gradient available for thermoelectric effects and lowering the Seebeck coefficient.[95] This trade-off relationship explains the observed enhancements in both the carrier mobility and Seebeck coefficient in the MH-PS/CNT and MT-PS/CNT nanocomposites, thus highlighting the synergistic effects of BCP incorporation on the thermoelectric performance.

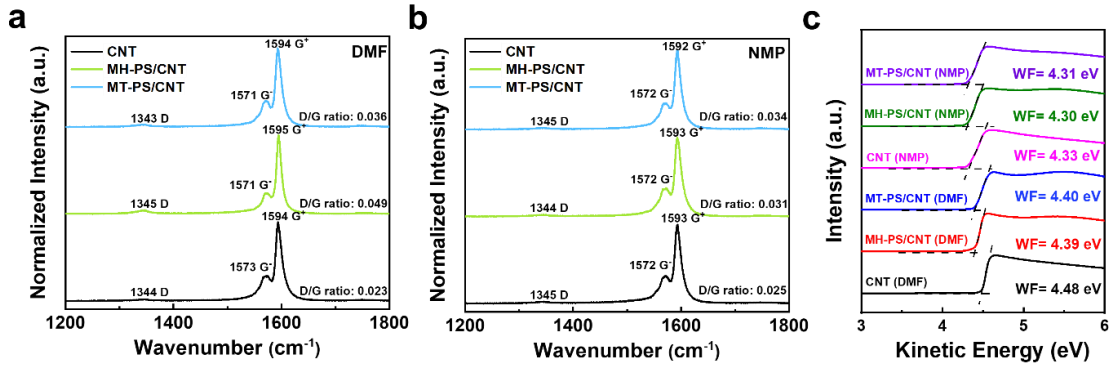

Figure 3.9 Raman spectra of CNT and BCP/CNT nanocomposites films in (a) DMF (b) NMP solvent. (c) UPS spectra and work function of CNT and BCP/CNT nanocomposites films.

doi:10.6342/NTU202502950

Table 3.3 Hall measurement results. Carrier mobility, carrier concentration and conductivity of BCP/CNT nanocomposites.

Nanocomposite	Carrier Concentration [cm^{-3}]	Carrier Mobility [$cm^2 V^{-1} s^{-1}$]	σ (Hall effect) [$S\ cm^{-1}$]	σ (Zem 3) [$S\ cm^{-1}$]
CNT (NMP)	-5.38×10^{22}	5.91×10^{-2}	459.6	572.08
MT-PS : CNT (1:2, NMP)	-4.81×10^{22}	7.75×10^{-2}	502.1	609.77
MH-PS : CNT (1:2, NMP)	-5.12×10^{22}	7.06×10^{-2}	495.2	581.55
CNT (DMF)	6.56×10^{22}	7.04×10^{-2}	606.8	564.17
MT-PS : CNT (1:2, DMF)	3.45×10^{22}	8.63×10^{-2}	420.8	436.26
MH-PS : CNT (1:2, DMF)	5.61×10^{22}	8.06×10^{-2}	558.3	534.56

doi:10.6342/NTU202502950

3.2.5. Morphological analysis of sugar-based BCP/CNT composites

The fabrication of CNT networks is often challenged by van der Waals forces between individual CNTs, which induce bundling and increased tube-to-tube junctions. This aggregation behavior can negatively affect the conductivity, as the presence of these junctions impedes the charge transport. A higher conductivity can be achieved with effective CNT dispersion, which reduces agglomeration and debundle the nanotubes.[96] Hence, precise control over the morphology of nanocomposite thin films is critical for optimizing their thermoelectric properties. The morphologies of the pristine CNTs and the various BCP/CNT composites in NMP and DMF are revealed by the SEM and AFM images in **Figure 3.10–13**. Notably, the CNT bundles dispersed in NMP exhibit similar morphological features and bundle sizes (**Figure 3.10a–c** and **Figure 3.11**), with only slight changes upon the addition of the sugar-based BCP. This observation arises from the high dispersibility of NMP, which is known to be one of the most effective organic solvents for CNT exfoliation.[97] Consequently, the addition of BCP provides only marginal improvements in CNT dispersion.[98] By contrast, the CNTs dispersed in DMF exhibit a larger average bundle size of 28.5 ± 26.4 nm, with a surface roughness of 29.0 nm, compared to 21.0 ± 12.1 nm and 20.6 nm, respectively, in NMP. Despite DMF being generally regarded as a good solvent for achieving well-dispersed CNTs, previous studies

doi:10.6342/NTU202502950

have suggested that the solubility of CNTs in DMF is lower than in NMP.[30b, 99] This discrepancy can be addressed by the incorporation of a sugar-based BCP, which effectively enhances the CNT dispersion and reduces the surface roughness, as demonstrated in **Figure 3.10d–f** and **Figure 3.11–Figure 3.14**. However, decreasing the polymer:CNT weight ratio to 1:3 in the MH-PS/CNT nanocomposite (in DMF) leads to an increase in bundle size, approaching that of the pristine CNTs. A concurrent decline in the electrical conductivity is also observed as the MH-PS content decreases (**Figure 3.7a**), thereby indicating the essential role of polymer content in maintaining the electrical performance of the nanocomposite. The transmission electron microscopy (TEM) images in **Figure 3.15** further reveal the successful wrapping of the sugar-based BCP around the CNT network, indicating effective interactions that enhance the CNT dispersion while preserving the structural integrity of the composite.

doi:10.6342/NTU202502950

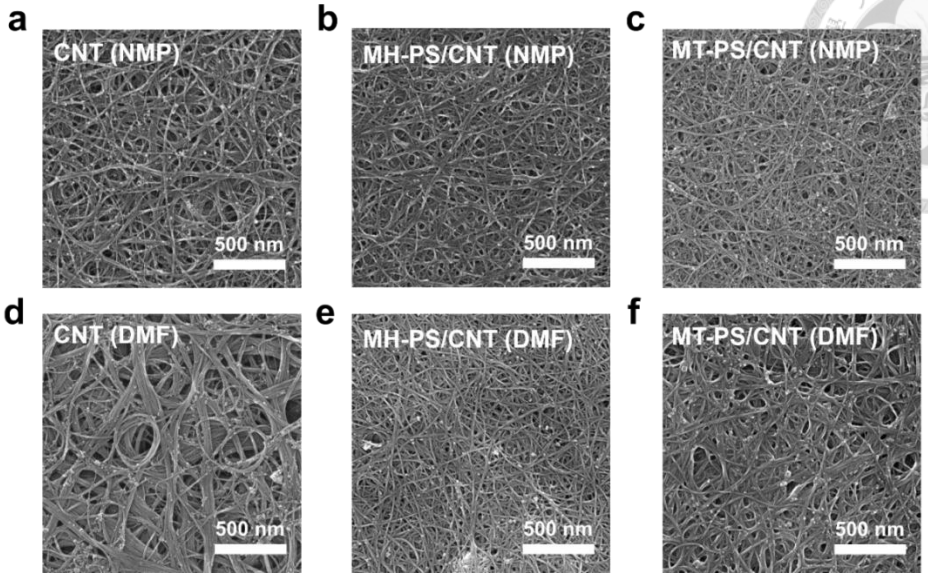

Figure 3.10 SEM images of CNT and BCP/CNT nanocomposite films prepared with a weight ratio of 1:2 in NMP solvent: (a) CNT, (b) MH-PS/CNT, (c) MT-PS/CNT films and in DMF solvent: (d) CNT, (e) MH-PS/CNT, (f) MT-PS/CNT films.

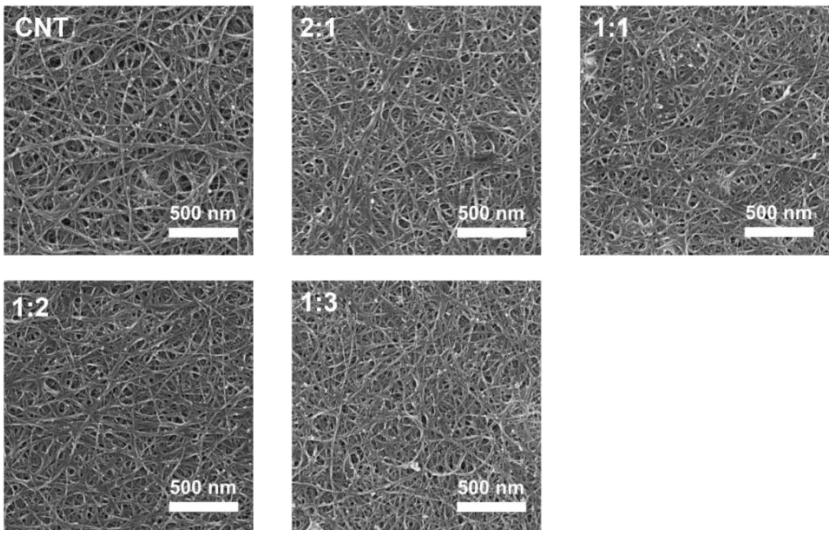

Figure 3.11 SEM images of nanocomposite thin films fabricated in NMP solvent. Pristine CNT and various mass ratio of MH-PS/CNT nanocomposites.

doi:10.6342/NTU202502950

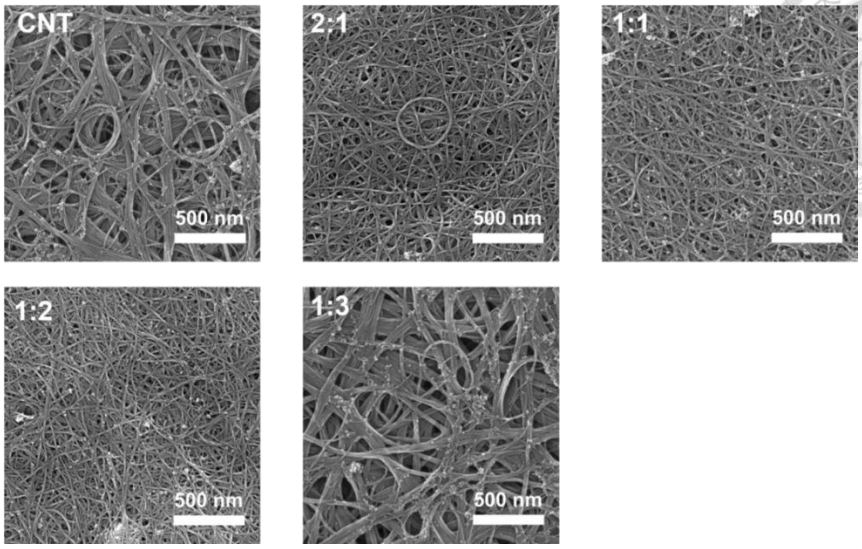

Figure 3.12 SEM images of nanocomposite thin films fabricated in DMF solvent. Pristine CNT and various mass ratio of MH-PS/CNT nanocomposites.

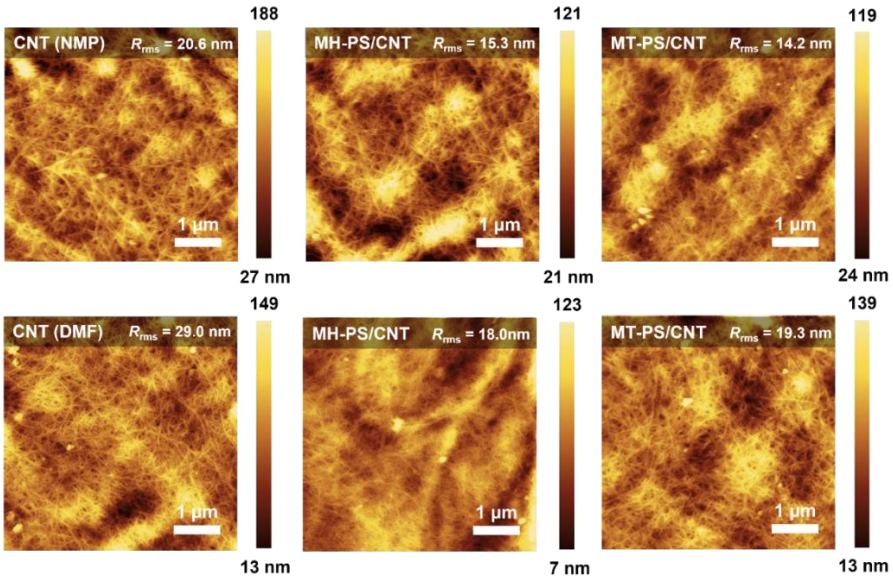

Figure 3.13 AFM images and surface roughness of nanocomposite thin films. Pristine CNT, MT-PS/CNT and MH-PS/CNT nanocomposites in NMP and DMF solvent.

doi:10.6342/NTU202502950

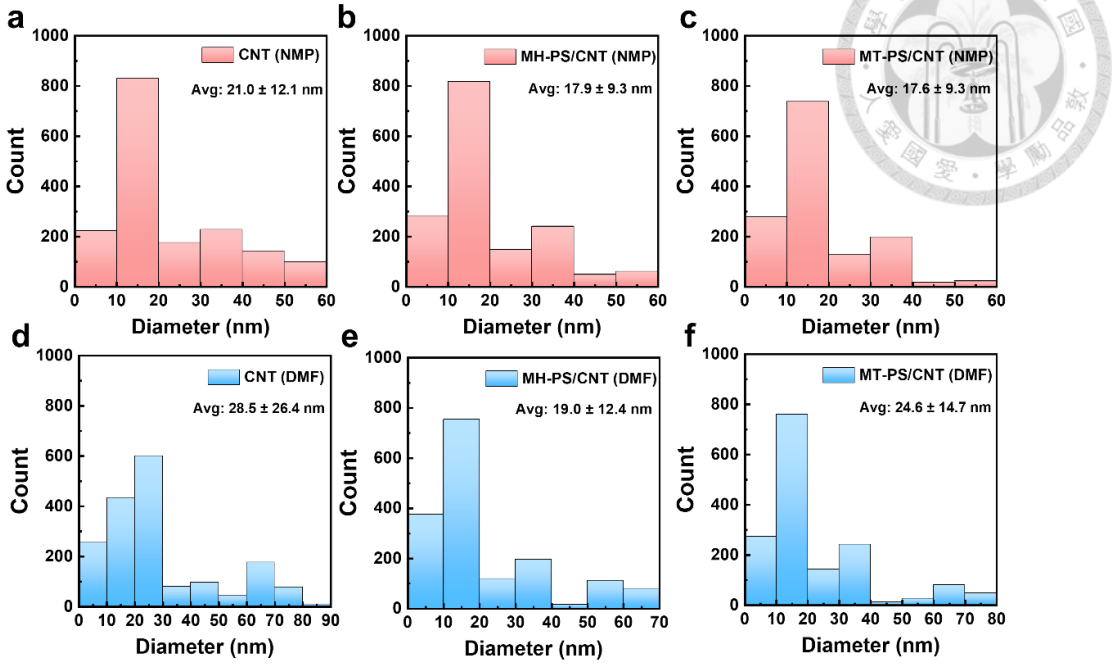

Figure 3.14 CNT bundle size obtained from SEM images. The bundle size was measured using ImageJ software.

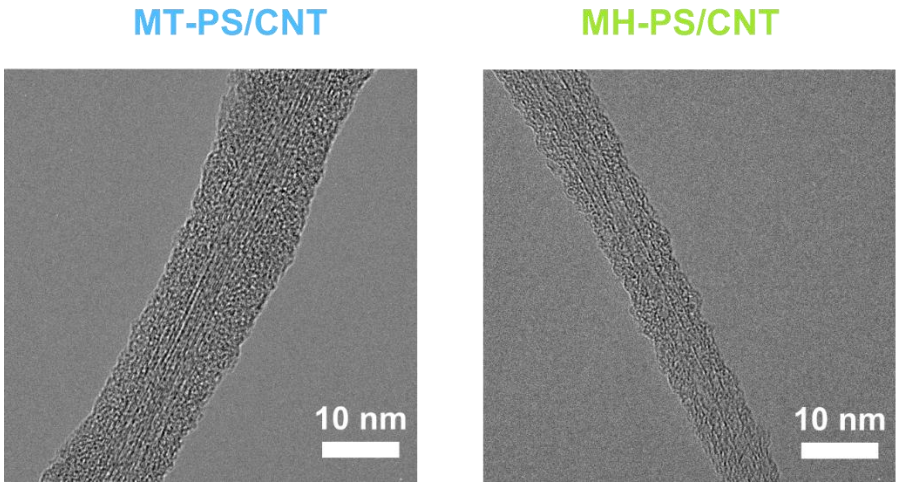

Figure 3.15 TEM images of nanocomposite thin films. MT-PS/CNT and MH-PS/CNT nanocomposites at a mass ratio of 1:2.

doi:10.6342/NTU202502950

3.2.6. Stability Test and Performance Comparison of Sugar-based BCP/CNT Composites

The results in **Figure 3.16** provide a comparative analysis of the long-term TE performance stability of the BCP/CNT nanocomposites fabricated in NMP and DMF under various environmental conditions. Notably, the n-type thin films initially exhibit a pronounced decrease in Seebeck coefficient, which is eventually reversed to a positive value when exposed to ambient conditions. However, these same films exhibit high stability in an inert environment. Previous research has indicated that the n-type characteristics of CNTs dispersed in NMP are inherently unstable in air within an hour.[100] Although the incorporation of polymers or molecular dopants can mitigate this instability, they do not completely prevent the reversal of n-type behavior over time.[101] This change in Seebeck coefficient can, however, be reversed by annealing, where elevated temperature facilitates the physical desorption of oxygen and water molecules from the nanotube surfaces and prevents further oxidation,[102] as demonstrated in **Figure 3.3**. Notably, the MH-PS/CNT composite shows a slower decline in its negative Seebeck coefficient (**Figure 3.16a**) compared to the MT-PS/CNT counterpart, thereby indicating improved surface coverage on the CNTs, which effectively alleviates air oxidation. This behavior can be attributed to the longer block structure of MH-PS, which contains a

doi:10.6342/NTU202502950

greater number of polymer chains that block oxygen diffusion more efficiently. A similar effect has been observed in alkyltrimethylammonium bromide surfactant/CNT systems, where an increase in alkyl chain length was shown to enhance the air stability.[52, 103] For DMF-based composites, shown in **Figure 3.16b**, the positive Seebeck coefficient also demonstrates a gradual decrease in ambient conditions but remains remarkably stable in a glove box for up to 35 days. These results suggest that with suitable encapsulation to impede air-induced oxidation, thermoelectric devices with stable performance can be fabricated and maintained for extended periods (over a month), a crucial consideration for practical applications.

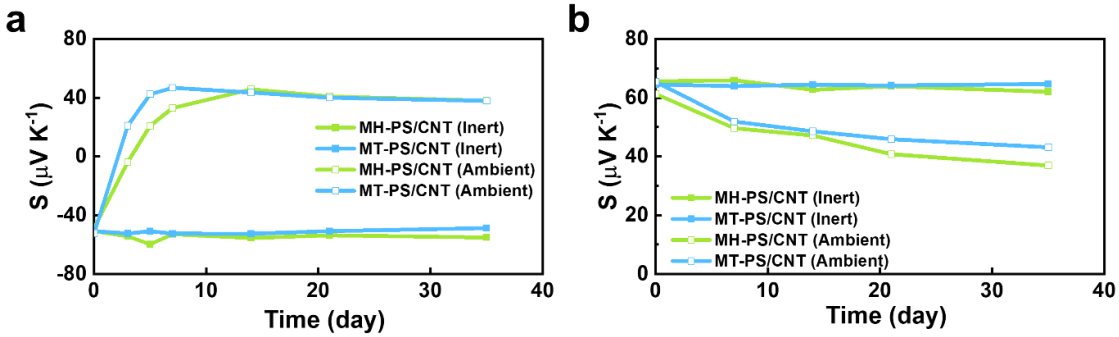

Figure 3.16 Environmental stability of BCP/CNT nanohybrids. (a) NMP-based n-type films and (b) DMF-based p-type films under inert (nitrogen-filled glove box) and ambient conditions (298 K, RH = 50%).

doi:10.6342/NTU202502950

3.2.7. Evaluation of Prototype Sugar-based BCP/CNT Composite TEG

A prototype TEG was assembled by connecting five pairs of p-n junctions in series, as depicted in **Figure 3.17a** and detailed in the Experimental Section. The TEG was configured as a flexible, lateral-structured device, making it ideally suited for integration into wearable TE systems. The results in **Figure 3.18** demonstrate that the nanocomposite bent along the short axis of the TEG can achieve a bending ratio of 78%. Both the MT-PS/CNT and MH-PS/CNT devices maintain stable electrical resistance during 1,000 bending cycles (**Figure 3.17b**), thereby indicating suitable mechanical durability for use in flexible energy harvesting systems. During testing, the heat sink was maintained at a constant temperature of 298 K, while the temperature difference (ΔT) between the heat sink and the heat source was set to increments of 5, 10, 15, 20, and 25 K to measure the output voltage and power. At each tested ΔT, the TEG output exhibits a stable, linear relationship between output voltage and current, both of which increase proportionally with the ΔT. The maximum recorded output power is 126.99 nW for the MH-PS/CNT device and 133.90 nW for the MT-PS/CNT device, both measured at ΔT = 25 K. The theoretical output voltage was calculated by summing the Seebeck coefficients of the p-type and n-type legs and multiplying by the number of leg pairs and the temperature difference. Thus, the estimated ideal output voltage is 15.95 mV for the MH-PS/CNT

doi:10.6342/NTU202502950

device and 17.28 mV for the MT-PS/CNT device, which are slightly higher than the experimental values of 13.85 and 14.46 mV, respectively. This discrepancy is likely due to contact resistances introduced during module fabrication, which leads to a certain voltage drop in each TEG device. Thus, the hybrid sugar-based BCP/CNT nanocomposites enable the straightforward fabrication of both p- and n-type legs by optimizing the choice of solvents and BCP ratios, thereby enabling the development of a series-connected p-n junction TEG. This approach demonstrates a significant potential for scalable and efficient energy-harvesting solutions, and offers a promising pathway for future advancements in flexible TE technology.

doi:10.6342/NTU202502950

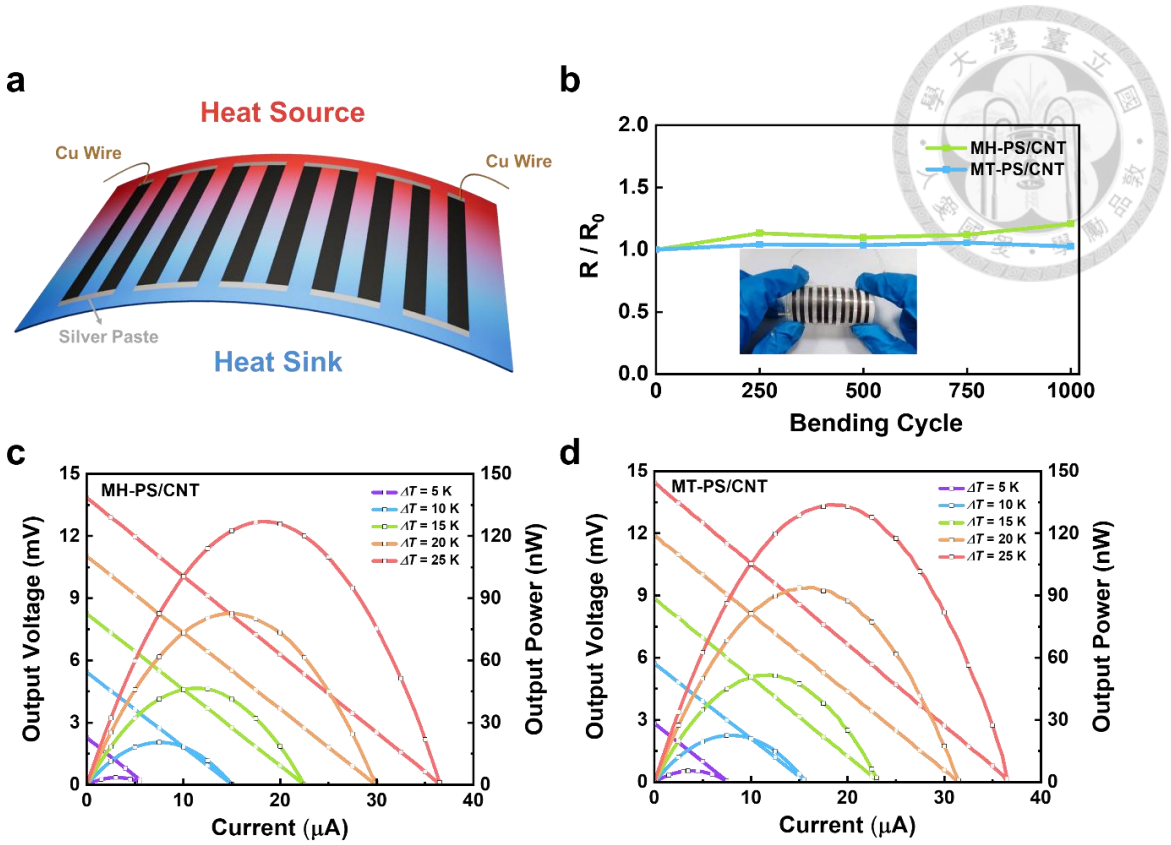

Figure 3.17 Demonstration of sugar-based BCP/CNT thermoelectric generators. (a) Schematic illustration of BCP/CNT-based TEG. (b) Evaluation of internal resistance at a 78% bending ratio across various cycles, along with photographic images of the TEG during the bending test. Output performance of the TEG with 5 pairs of legs under varying temperature gradients for (c) MH-PS/CNT and (d) MT-PS/CNT configurations.

doi:10.6342/NTU202502950

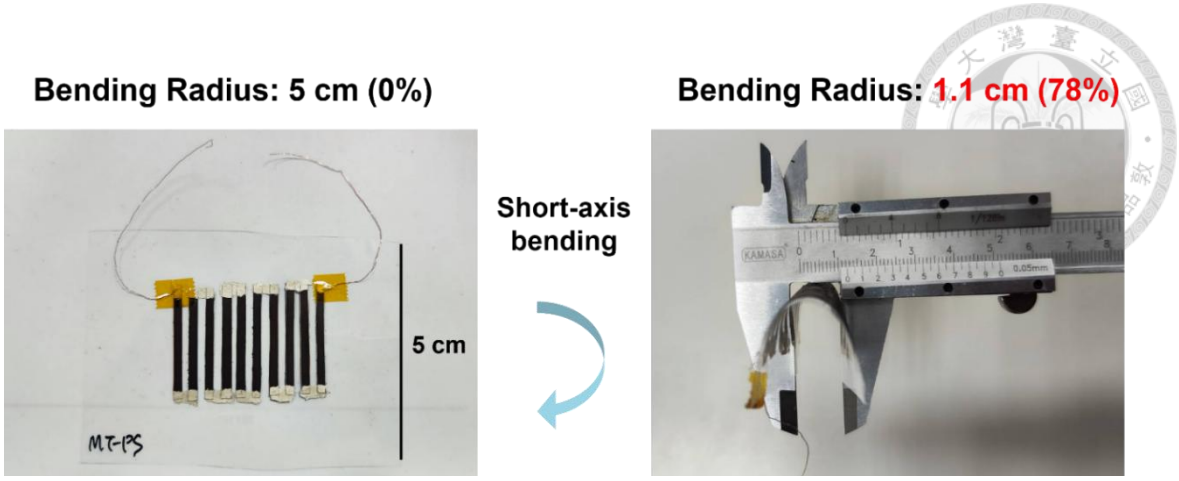

Figure 3.18 Photographic images of the TEG. Flexible TEG under the flat condition and bending test.

3.3. Summary

Our study presents a novel strategy for enhancing the thermoelectric performance by incorporating distinct carbohydrate-based BCP (specifically MT-PS and MH-PS) into CNT matrix. The optimization of solvent systems and weight ratios further amplifies the TE efficiency, thereby indicating the role of the processing environment in facilitating the realization of both n- and p-type semiconductors. This environment-driven tunability of the Fermi level enables ambipolar TE behavior within the same polymeric system. The results reveal that these sugar-based BCPs effectively encapsulate the debundled CNT networks, thereby contributing to enhanced thermoelectric properties in both n- and p-type configurations. When optimized, both the MH-PS/CNT and MT-PS/CNT

doi:10.6342/NTU202502950

nanocomposites manifest superior TE performance relative to pristine CNT networks. However, MT-PS offers an economic advantage over MH-PS due to its reduced production costs, which makes it a more favorable candidate for large-scale commercial applications. Conversely, the n-type MH-PS/CNT composite shows greater performance and environmental stability and durability under ambient conditions, which is likely due to the protective effect of the longer polymer chains against oxidative degradation. This balance between cost-effectiveness and performance presents an interesting challenge for optimization, with the potential to inspire hybrid systems that combine the beneficial attributes of both MT-PS and MH-PS.

doi:10.6342/NTU202502950

4. Sugar-Functionalized Carbon Nanotubes in Aqueous Dispersions: Tailoring Interfaces for Thermoelectric Energy Harvesting

4.1. Brief Introduction

In this study, we employed click chemistry strategy to fabricate sugar-functionalized CNTs. To the best of the present authors' knowledge, the covalent grafting of maltose-derived alkynes or structurally related saccharide-based molecules onto CNTs for thermoelectric applications has not previously been reported. This approach provides a strategy for tailoring the polymer-CNT interfacial properties by grafting bio-derived functionalities such as maltotriose (MT) or maltoheptaose (MH) onto the CNT surfaces. The resulting sugar-functionalized CNTs exhibit enhanced dispersion in aqueous media, along with reduced thermal conductivity, thereby improving the energy conversion efficiency in thermoelectric films. This work provides a new molecular design platform for modulating the interfacial properties of CNTs toward environmentally friendly and high-performance thermoelectric materials.

doi:10.6342/NTU202502950

4.2. Results and Discussion

4.2.1. Synthesis of Sugar-Functionalized CNTs

A surface modification strategy is used to synthesize sugar-functionalized CNTs via click chemistry, wherein the abundant hydroxyl groups on the sugar moieties promote strong interactions with water, thereby effectively stabilizing the sugar-functionalized CNTs in dispersion. The synthetic route for preparing the sugar-functionalized CNTs is illustrated in **Figure 4.1**.

Here, the first step involves the preparation of azide-modified CNTs**.** Previous reports[104] have shown that azide groups can be introduced at graphitic edges via iodine radical reactions with iodine azide, which is generated in situ from iodine chloride and sodium azide in a polar solvent.[105] However, the highly unstable and explosive nature of the intermediate iodine azide represent significant safety concerns.[106] As an alternative approach, Manoharan *et al.* proposed a safer method involving silane-modified CNTs, where azide groups are introduced by the S_N2 substitution of silane-terminal bromine atoms.[74] In the present work, this milder approach is adopted to achieve azide-functionalized CNTs, thereby enabling subsequent click chemistry for covalent modification of the CNT surface under controlled conditions. As detailed in the Experimental section, commercially available carboxylated CNTs (CNTCOOH) were

doi:10.6342/NTU202502950

first reacted with a silane coupling agent in toluene, where silanized CNT (CNT-silane) introduces reactive terminal groups. This was followed by substitution with sodium azide to introduce azide functionalities, thereby enabling site-specific conjugation via azide-alkyne cycloaddition. Finally, a copper-catalyzed azide-alkyne cycloaddition (click) reaction was performed to covalently attach the propargylated oligosaccharides MT or MH to the azide-functionalized CNTs. This functionalization strategy imparts enhanced hydrophilicity to the CNT surfaces by the introduction of carbohydrate moieties.

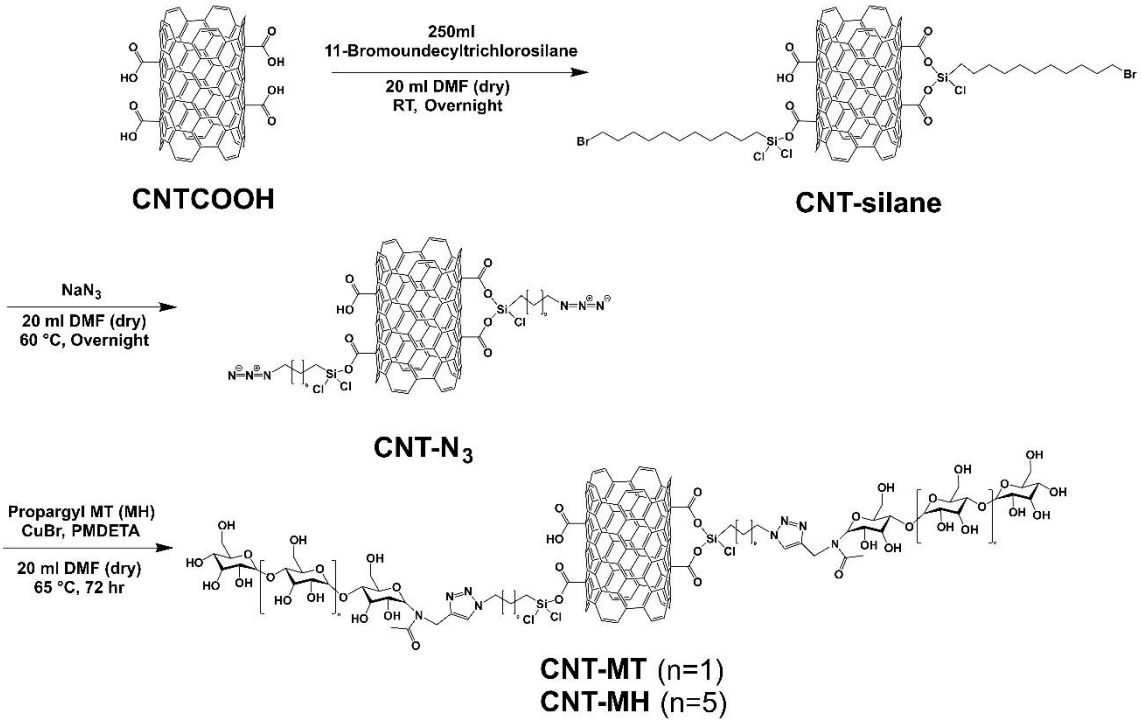

Figure 4.1 Schematic representation of the synthesis and functionalization of CNTs with sugar polymers.

doi:10.6342/NTU202502950

4.2.2. Spectroscopic Properties of Sugar-Functionalized CNTs

X-ray photoelectron spectroscopy (XPS) was used to assess the degree of functionalization and investigate the surface chemical modifications during the synthesis process. This technique enables a quantitative analysis of the elemental composition and provides insights into the electronic structure of the CNT surface at each functionalization stage. The high-resolution Si 2p spectrum of the CNT-silane is presented in **Figure 4.2a**. Here, the deconvoluted peaks correspond to two distinct Si environments: the peak at 102.3 eV is assigned to the Si–O–C bonds, thereby indicating successful covalent bonding between the silane reagent and the carboxylated CNT sidewalls, while the peak at 103.2 eV corresponds to Si–O–Si linkages arising from crosslinking between silane molecules.[107] The predominance of the Si–O–C peak suggests high silanization efficiency and effective grafting of silane onto the CNT surface. The quantitative results in **Table 4.1** indicate a near-complete substitution of end-cap bromines with azides. This azide functionalization is confirmed by the N 1s spectrum of the azide-modified CNTs in **Figure 4.2b**. Here, two distinct peaks are observed, where the higher binding energy (404.5 eV) peak corresponds to the central, electron-deficient nitrogen atom (N=N=N) of the azide group, while the lower binding energy (400.7 eV) peak is attributed to the terminal nitrogen atoms (N=N=N).[105a, 108] The observed intensity ratio of ~1:2 aligns

doi:10.6342/NTU202502950

with the expected stoichiometry of the azide moiety, thereby confirming the successful introduction of azide functionalities. The nitrogen contents of azide-functionalized CNTs synthesized via different methods are compared in **Table 4.2** of the Supporting Information. These results demonstrate that the silane-based approach used herein yields a significantly higher nitrogen content (4.15 at.%) than does the previously reported iodine azide method (1.15 at.%),[104] thereby indicating the improved efficiency of the silane strategy for CNT surface azidation.

The progression of the click reaction is revealed by tracking the changes in the multi-term peak separation (MT-PS) in the N 1s spectrum over time (**Figure 4.2c**). Thus, as the reaction proceeds, a broadening and small blue shift is observed for the lower binding energy peak, while the intensity of the higher binding energy peak gradually decreases. This spectral evolution is characteristic of triazole formation and indicates increasing conversion of azide groups to 1,2,3-triazoles, with near-complete conversion after 72 h.[105a] After bonding with sugar moieties, both the CNT-MT and CNT-MH samples exhibit complete azide-to-triazole conversion, as confirmed by their N 1s spectra (**Figure 4.2d**). Additionally, the XPS analysis in **Table 4.1** and **Figure 4.3** reveals a marked increase in oxygen content after sugar functionalization. Specifically, the oxygen content increases from 6.81 at.% for the CNTCOOH to 12.68 at.% for the CNT-MT and 26.62

doi:10.6342/NTU202502950

at.% for the CNT-MH, thereby reflecting the abundance of hydroxyl groups on the saccharide chains. The higher oxygen content of the CNT-MH compared to the CNT-MT is attributed to the greater chain length of MH relative to MT, thereby providing additional hydroxyl functionalities that enhance the hydrophilicity and potential for intermolecular hydrogen bonding.

The surface functional groups introduced during each step of functionalization are identified by the attenuated total reflection Fourier-transform infrared (ATR-FTIR) spectroscopy results in **Figure 4.4a**. As expected, the pristine CNTs exhibit minimal IR absorption features due to their chemically inert surfaces. By contrast, the CNTCOOH sample displays a broad and intense absorption band, which is attributed to overlapping O–H and C=O stretching vibrations from the abundant hydroxyl and carboxylic acid groups. After silanization, new peaks are observed that correspond to $–CH_2$ stretching vibrations ($\nu_{asym}\ CH_2 = 2928\ cm^{-1}$ and $\nu_{sym}\ CH_2 = 2851\ cm^{-1}$) and symmetric deformation ($\delta_{sym} = 1260\ cm^{-1}$), thereby confirming the successful grafting of long-chain alkyl silane molecules onto the CNT surface.[74, 109] Although the abovementioned XPS analysis confirmed azide functionalization, the characteristic N_3 stretching band near 2100 cm^{-1} is not clearly detected in the ATR-FTIR spectrum of CNT-N_3, which is likely due to the limited sensitivity of the latter technique for low-abundance functional groups. Upon

doi:10.6342/NTU202502950

click functionalization with sugar moieties, the disappearance of the alkyne stretching band at 2120 cm^{-1} (**Figure 4.5**) and the emergence of a new absorption peak near 1554 cm^{-1}, corresponding to the C=N stretching vibration of 1,2,3-triazole rings, provide strong evidence for the successful covalent attachment of sugar molecules onto the CNT backbone.[110]

The aqueous dispersibility of the functionalized CNTs is evaluated by the UV-vis-NIR absorption spectroscopy results in **Figure 4.4b**. Here, water was chosen as the dispersion medium due to its capacity for hydrogen bonding, which can stabilize CNTs with hydrophilic surface functionalities. Individual CNTs are known to exhibit characteristic absorption bands in the 250–270 nm range, which are attributed to transitions associated with one-dimensional van Hove singularities, whereas agglomerated or bundled CNTs typically show negligible absorbance in this region.[111] Meanwhile, the UV-vis-NIR spectra of the pristine sugars in **Figure 4.6** reveal no significant absorption peaks, as these are probably masked by the UV cutoff of the water solvent near 200 nm. Therefore, an evaluation of the CNT dispersion quality based on the absorbance intensity in this region is regarded as valid. Thus, in **Figure 4.4b**, the pristine CNTs exhibit weak absorption at ~270 nm, which is consistent with their poor aqueous dispersibility, while both the CNT-MT and CNT-MH exhibit markedly stronger

doi:10.6342/NTU202502950

absorptions at this wavelength, thereby indicating improved exfoliation and dispersion stability. Notably, the CNT-MH exhibits the highest absorbance, which is consistent with its enhanced hydrophilicity and solvent interactions due to its longer saccharide chain. These findings are further confirmed by visual observation of the aqueous dispersions in **Figure 4.7**. While the pristine CNTs readily re-agglomerate into bundles and undergo sedimentation within hours due to poor dispersion, the sugar-functionalized CNTs, particularly the CNT-MH, remain stably dispersed for at least 7 days, thereby indicating strong interfacial compatibility with the aqueous medium.

The structural integrity and defect levels induced by the chemical modifications are revealed by the Raman spectroscopy results in **Figure 4.4c** and **d**. Here, the radial breathing mode (RBM), which is a unique feature of single-walled CNTs (SWCNTs),[112] was significantly suppressed in all functionalized samples, which suggests the surface functionalization dampen the vibration mode of CNTs (**Figure 4.4c**). Nevertheless, the intensity ratio of the D and G bands (I_D/I_G), which is a common metric for quantifying the density of defects, exhibits only a modest increase after functionalization (**Figure 4.4d**).[113] This suggests that while surface chemistry was effectively introduced, the underlying sp^2-hybridized carbon framework remained largely preserved, which is beneficial for retaining the charge transport properties of the CNTs.

doi:10.6342/NTU202502950

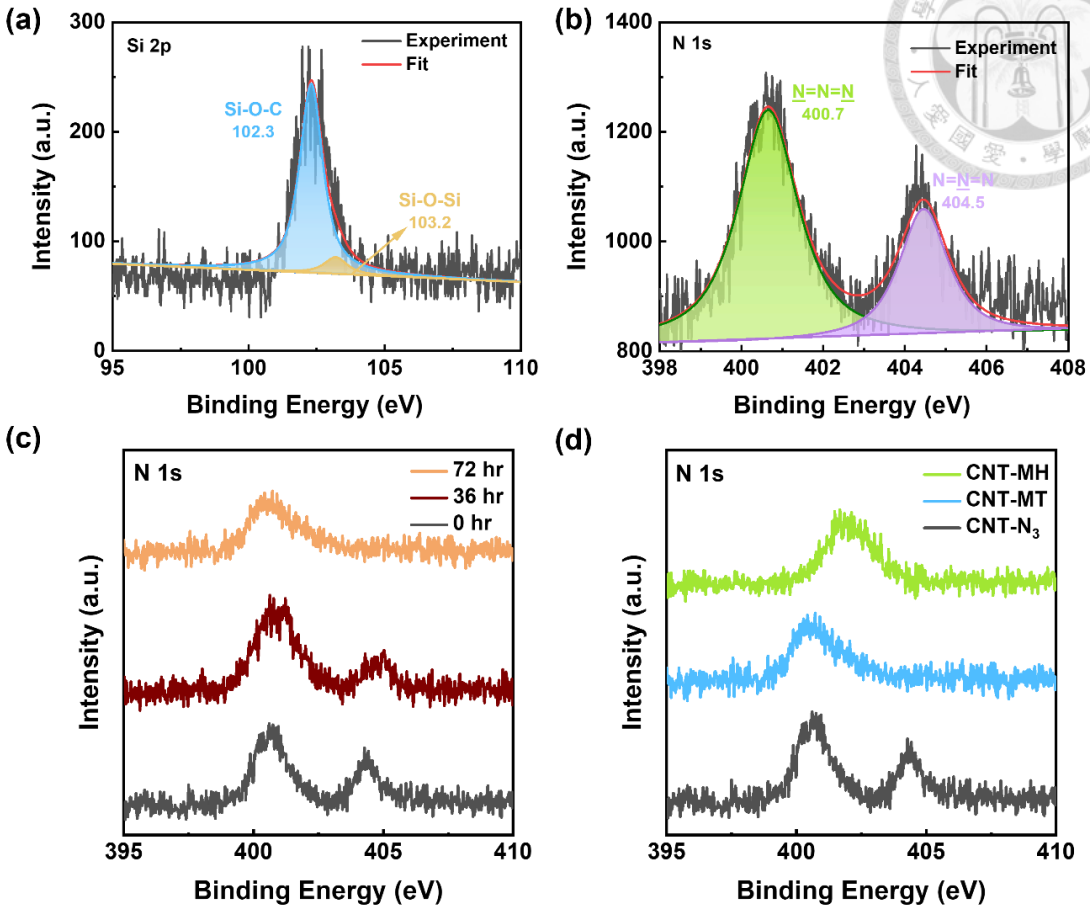

Figure 4.2 XPS spectra of CNT samples: (a) Si 2p peak of carboxylated CNTs after silanization; (b) N 1s peak of azide-functionalized CNTs; (c) MT-PS N 1s peaks after different click reaction times; (d) Comparison of N 1s peaks between azide-functionalized CNTs and the final sugar-functionalized CNT products.

doi:10.6342/NTU202502950

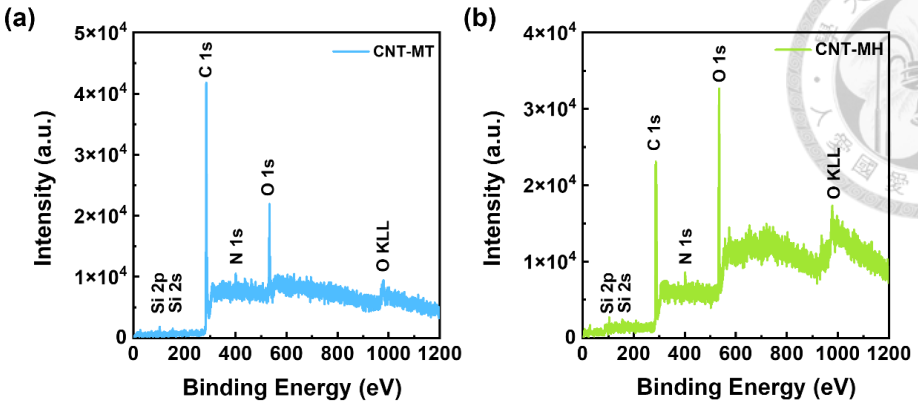

Figure 4.3 XPS full Spectra of (a) CNT-MT and (b) CNT-MH.

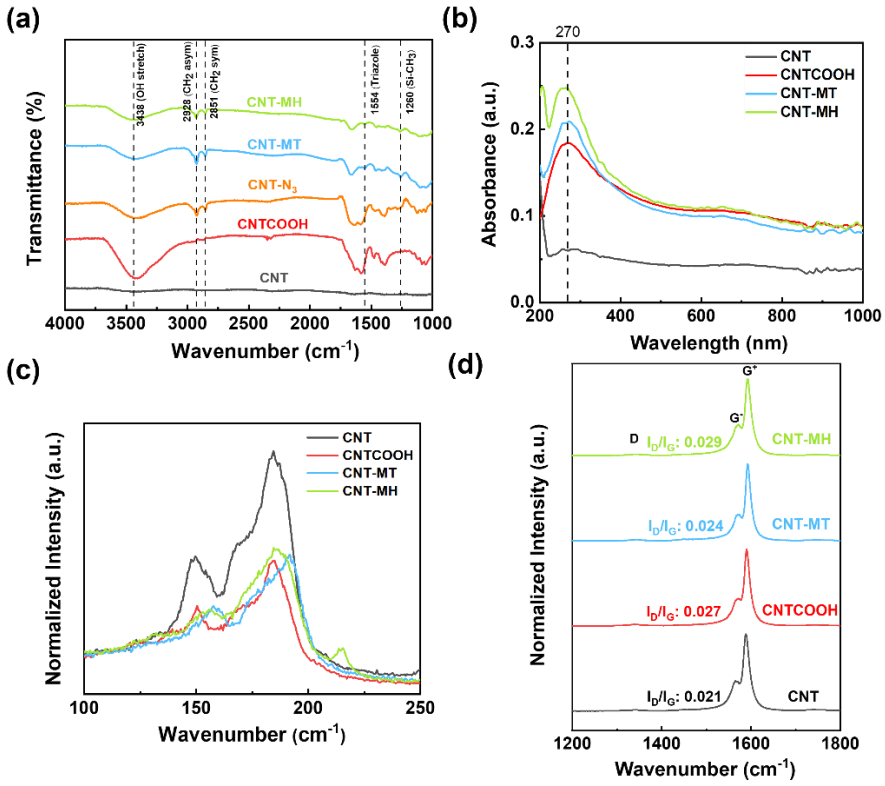

Figure 4.4 (a) ATR-FTIR transmission spectrum, (b) UV-vis-NIR absorption spectrum, (c) Raman spectrum highlighting the radial breathing mode (RBM), and (d) Raman spectrum showing the D and G bands of the as-synthesized samples.

doi:10.6342/NTU202502950

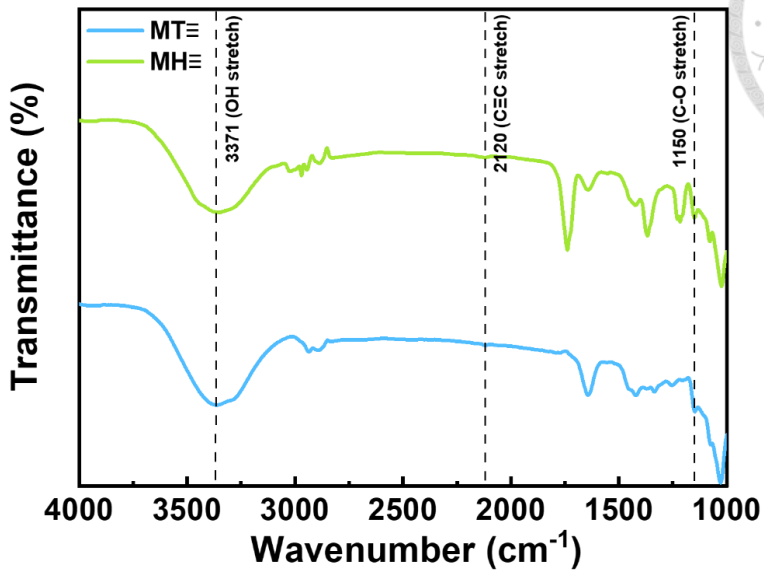

Figure 4.5 ATR-FTIR Spectrum of alkyne-functionalized MT and MH.

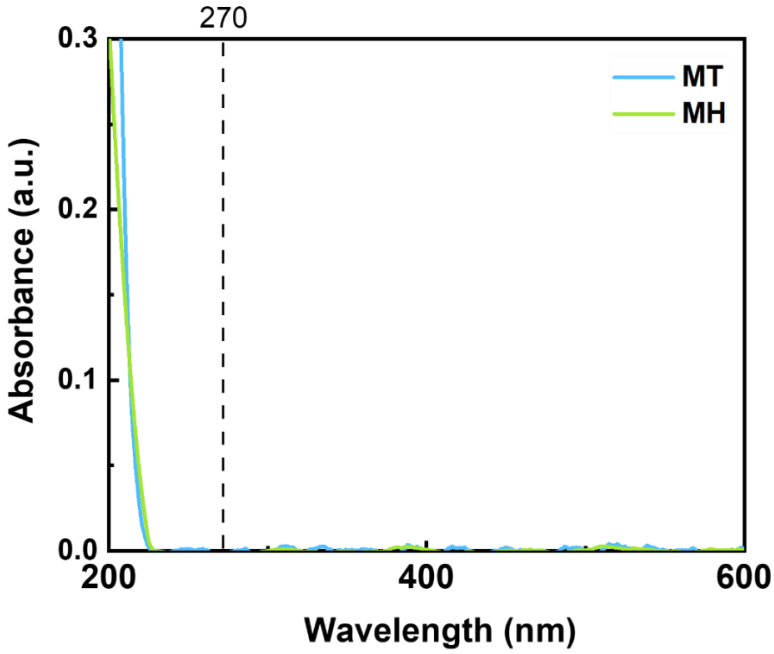

Figure 4.6 UV-Vis Spectrum of MT and MH dissolved in water.

doi:10.6342/NTU202502950

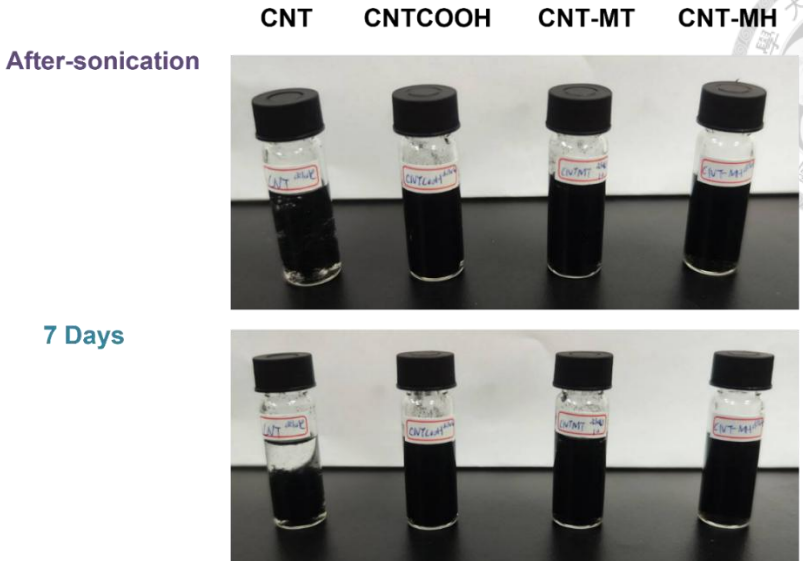

Figure 4.7 Photographs of dispersion stability of CNT and functionalized-CNT in water.

Table 4.1 Atomic concentrations of functionalized CNTs determined by XPS measurement. Reported values represent the average of five measurement points.

Sample	C 1s (%)	N 1s (%)	O 1s (%)	Si 2p (%)	Br 3d (%)
CNTCOOH	93.19	-	6.81	-	-
CNT-silane	92.41	-	5.69	1.23	0.67
CNT-N_3	87.99	4.15	6.11	1.74	0.01
CNT-MT	82.75	3.27	12.68	1.26	0.02
CNT-MH	69.02	2.71	26.62	1.65	0.00

doi:10.6342/NTU202502950

Table 4.2 Atomic concentrations of CNT-N_3 synthesized using different methods, as determined by XPS analysis. Reported values represent the average of five measurement points for each sample.

Method	C1s (%)	N1s (%)	O1s (%)	Si2p (%)	Br3d (%)
Iodine azide	94.40	1.15	4.45	-	-
Silanized (Current)	87.99	4.15	6.11	1.74	0.01

4.2.3. Thermal Analysis of Sugar-Functionalized CNTs

The thermal stability and thermal transitions of the sugar-functionalized CNTs are elucidated by the corresponding thermogravimetric analysis (TGA), differential thermogravimetry (DTG), and differential scanning calorimetry (DSC) results. Thus, both the neat MT and MH saccharide polymers exhibit a decomposition (5% weight loss) temperature (T_d) of approximately 230 °C (**Figure 4.8a**), which is consistent with the known thermal behavior of saccharide-based materials.[114] However, while the CNTCOOH exhibits high thermal stability, with minimal weight loss below 400 °C, both the CNT-MT and CNT-MH exhibit an unexpectedly early weight loss onset at around 200 °C (**Figure 4.8b**). This behavior is elucidated by the XPS analyses before and after

doi:10.6342/NTU202502950

thermal treatment (**Table 4.3**). Here, the nitrogen content remains unchanged at 200 °C, which suggests that this temperature does not induce cleavage of the 1,2,3-triazole ring, in agreement with previous findings.[68] Conversely, the oxygen content of the CNT-MT decreases from 12.68 at.% before to 9.17 at.% after thermal treatment, which may be attributed to partial degradation or caramelization of the surface-bound sugar chains.[115] This relatively early thermal degradation implies that the immobilized saccharides are only weakly stabilized on the CNT surface, which is likely due to limited hydrogen bonding or intermolecular interactions. Notably, this reduced thermal cohesion may correlate with enhanced colloidal stability in aqueous media, as weaker intermolecular forces between the grafted chains create steric hindrance that further suppresses CNT bundling and aggregation.[116]

The DTG results (inset, **Figure 4.8a**) further confirm that thermal degradation of the sugar-functionalized CNTs occurs within the range of 200–400 °C. The complementary elemental analysis in **Table 4.3** shows a marked reduction in oxygen and nitrogen content at elevated temperatures, thereby confirming the decomposition of both saccharide moieties and triazole linkages. The total weight loss at 400 °C is 20.00% for the CNT-MT and 42.88% for the CNT-MH (**Figure 4.8b**). Based on these results, the estimated sugar substitution levels are approximately 1.27 and 1.86 sugar molecules per 100 carbon

doi:10.6342/NTU202502950

atoms for the CNT-MT and CNT-MH, respectively, corresponding to a higher grafting density for MH.

The thermal transitions are elucidated, and the specific heat capacity (C_p) determined, by the DSC results in **Figure 4.8c** and **Figure 4.9**–**Figure 4.11**. Thus, pure MT exhibits a glass transition temperature (T_g) of 124.3 °C (**Figure 4.9**), which is consistent with literature reports,[117] while the lack of a clear T_g for the MH is likely due to its higher molecular weight and more complex amorphous structure. Meanwhile, the DSC profiles of the sugar-functionalized CNTs also exhibit no discernible glass transitions (**Figure 4.8c**), which can be attributed to the low content of sugar moieties relative to CNTs and the limited sensitivity of conventional DSC techniques for detecting thermal transitions in low-loading, surface-tethered polymers.[118]

The temperature-dependent C_p values of the various samples are shown in **Figure 4.10** and **Figure 4.11**, which reveal that the sugar-functionalized CNTs exhibit higher C_p values than the pristine CNTs. This enhancement is ascribed to the flexible molecular structures of the grafted saccharide chains, which introduce additional vibrational modes and thereby contribute to a larger C_p compared to the rigid CNT frameworks.[119] Based on these C_p values, the calculated thermal conductivity (κ) values are summarized in **Figure 4.8d** and **Table 4.4**. Due to the strong anisotropy of the CNT films, where κ

doi:10.6342/NTU202502950

varies significantly with direction,[120] the in-plane κ value was measured, which corresponds to the same direction as the thermoelectric measurements. Thus, the pristine CNTs and the CNTCOOH exhibit relatively high κ values of 15.56 and 16.23 W m^{-1} K^{-1}, respectively, thereby indicating efficient heat transport. By contrast, the sugar-functionalized CNT-MT and CNT-MH exhibit significantly lower κ values of 5.86 and 4.00 W m^{-1} K^{-1}, respectively. The more pronounced suppression of thermal conductivity in the CNT-MH is likely associated with its higher degree of functionalization, as estimated from the TGA analysis. This reduction in thermal transport is advantageous for thermoelectric applications, as a lower thermal conductivity directly contributes to an enhanced thermoelectric conversion efficiency.

doi:10.6342/NTU202502950

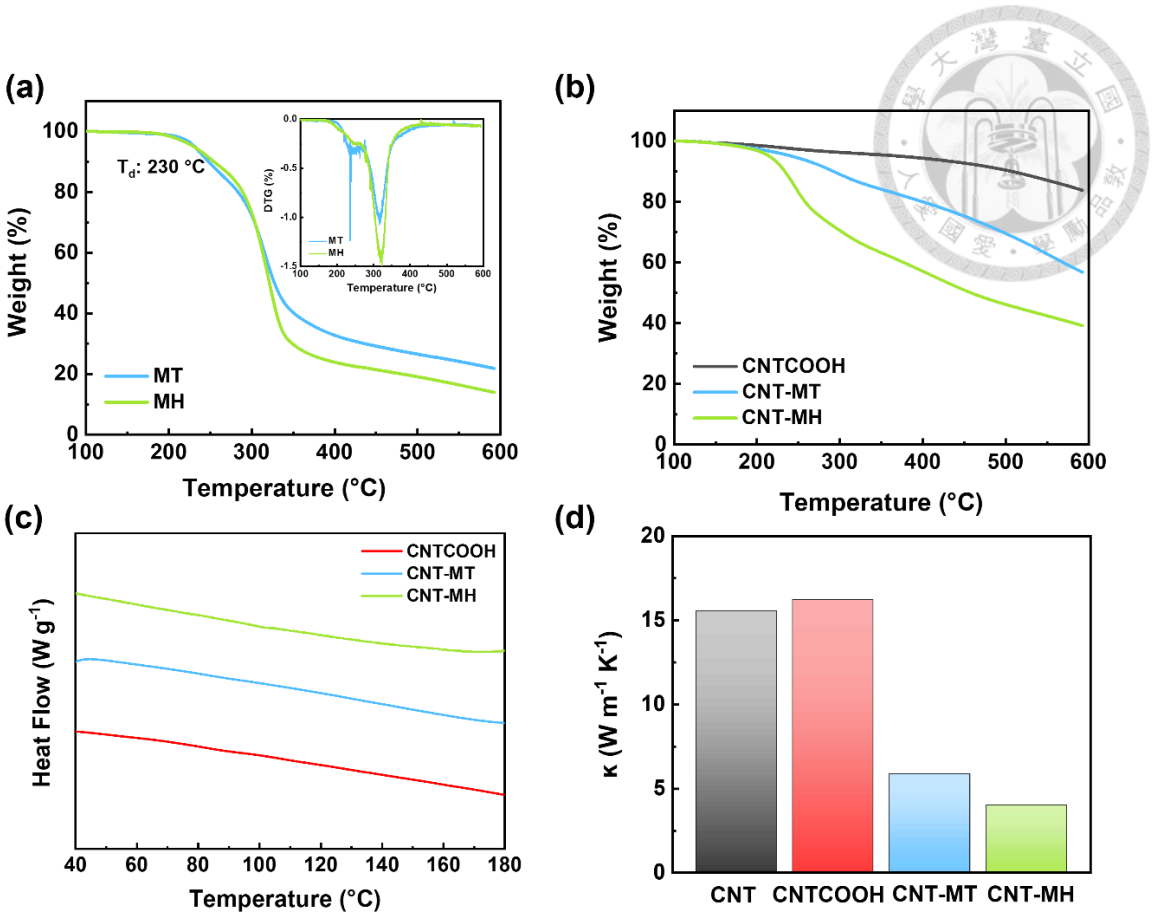

Figure 4.8 TGA analysis of (a) sugar polymers and (b) functionalized CNTs. (c) DSC analysis of functionalized CNTs. (d) In-plane thermal conductivity of each sample measured at 30˚C.

doi:10.6342/NTU202502950

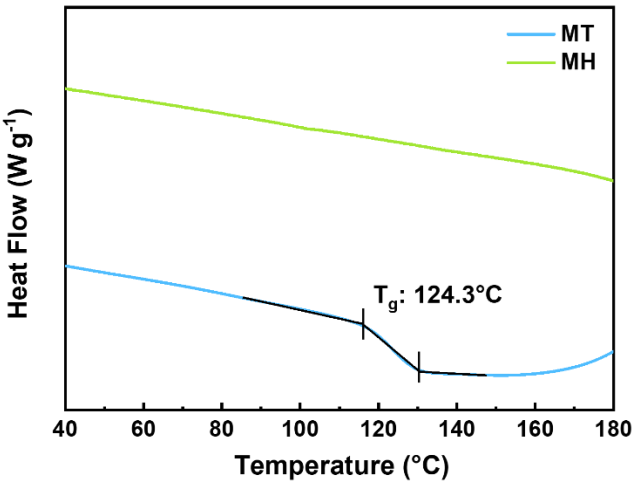

Figure 4.9 DSC analysis of sugar polymers MT and MH.

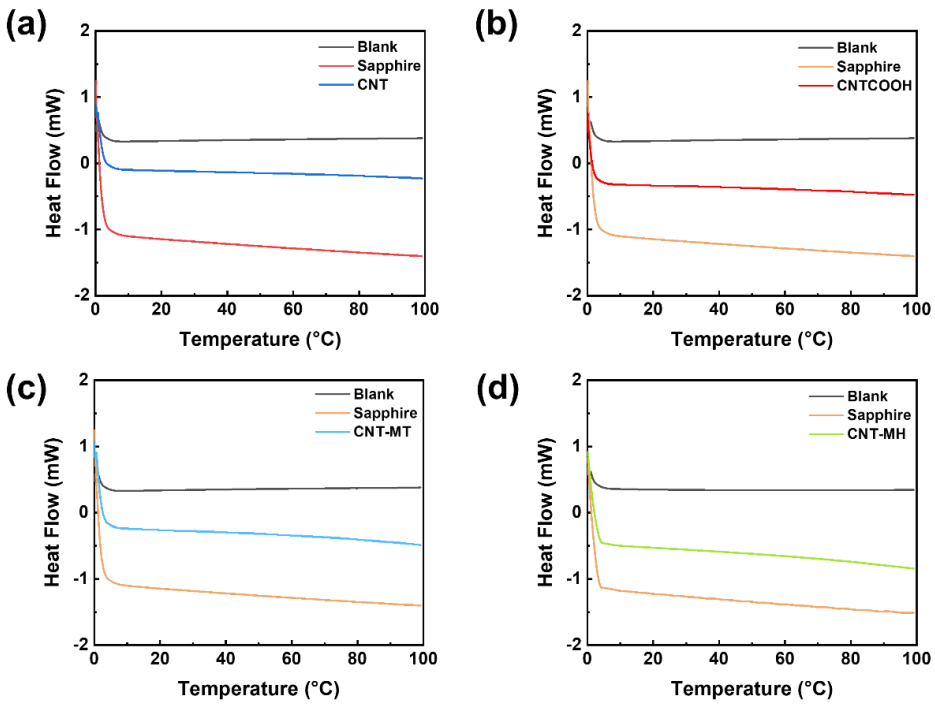

Figure 4.10 DSC heat flow curves of the empty pan, sapphire reference, and sample: (a) CNT, (b) CNTCOOH, (c) CNT-MT and (d) CNT-MH.

doi:10.6342/NTU202502950

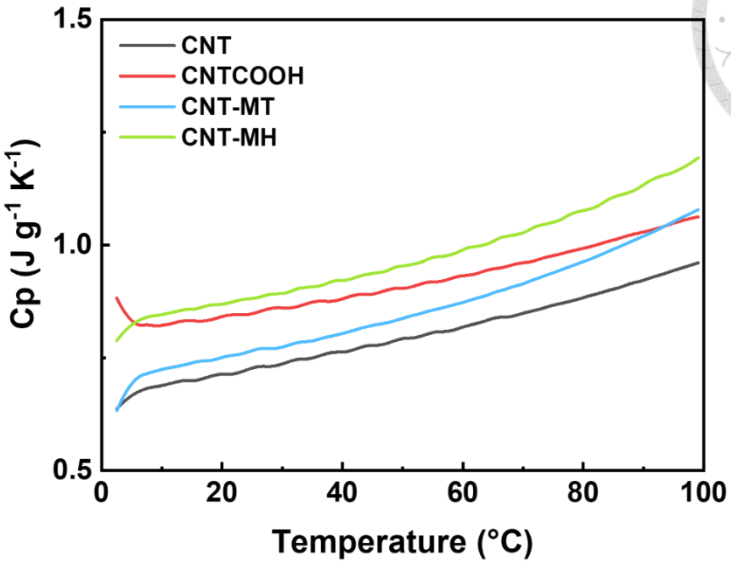

Figure 4.11 Specific heat capacity of each sample as a function of temperature, determined using the sapphire reference method.

Table 4.3 Atomic concentrations of CNT-MT heating at various heating temperatures, as determined by XPS analysis. Reported values represent the average of five measurement points for each sample.

Method	C 1s (%)	N 1s (%)	O 1s (%)	Si 2p (%)	Br 3d (%)
CNT-MT	82.75	3.27	12.68	1.26	0.02
CNT-MT (200˚C)	86.53	3.20	9.17	1.11	-
CNT-MT (400˚C)	92.67	1.34	4.75	1.24	-

doi:10.6342/NTU202502950

Table 4.4 Summary of measured values of density ($\boldsymbol{\rho}$), in-plane thermal diffusivity ($\boldsymbol{\alpha}$), specific heat capacity ($\boldsymbol{C_p}$) and in-plane thermal conductivity (κ) for each sample.

Sample	$\boldsymbol{\rho}$ [g cm^{-3}]	$\boldsymbol{\alpha}$ [m^2 s^{-1}]	$\boldsymbol{C_p}$ [J K^{-1} g^{-1}]	$\boldsymbol{\kappa}$ [W m^{-1} K^{-1}]
CNT	0.62	3.44×10^{-5}	0.73	15.56
CNTCOOH	0.51	3.74×10^{-5}	0.86	16.23
CNT-MT	0.43	1.77×10^{-5}	0.77	5.86
CNT-MH	0.64	8.17×10^{-6}	0.89	4.00

4.2.4. Morphological Analysis of Sugar-Functionalized CNTs

CNT networks intrinsically exhibit strong inter-tube van der Waals interactions, which promote aggregation and bundling, especially in aqueous environments. Therefore, morphological characterization is critical for evaluating dispersion quality and network formation, particularly for thin-film applications. In this respect, the atomic force microscopy (AFM) images in **Figure 4.12** reveal substantial differences in surface morphology between the pristine and functionalized CNTs. The pristine CNT films exhibit the highest root mean square surface roughness (R_{rms}) of 63.1 nm, thereby indicating pronounced aggregation and non-uniform topography. By contrast, the R_{rms}

doi:10.6342/NTU202502950

values progressively decrease for the CNTCOOH (40.5 nm), CNT-MT (38.8 nm), and CNT-MH (36.6 nm), thus suggesting smoother and more evenly distributed nanotube networks. This reduction in surface roughness implies effective suppression of CNT bundling due to surface functionalization. The presence of hydroxyl-rich sugar moieties likely enhances the interfacial interactions with water, thereby facilitating exfoliation and stabilization of individual nanotubes in dispersion.

These findings are further supported by the scanning electron microscopy (SEM) images in **Figure 4.12b**. Here, the pristine CNTs exhibit large, disordered bundles, while both the carboxylated and sugar-functionalized CNTs exhibit more finely dispersed networks. Based on these SEM images, the quantitative size distributions are presented in **Figure 4.13**. Thus, the pristine CNTs exhibit an average bundle diameter of 89.3 ± 53.6 nm with a broad distribution, thereby indicating the challenges in achieving controlled dispersion. Meanwhile, the CNTCOOH exhibits a reduced average bundle size of 58.7 ± 39.1 nm, although clusters larger than 100 nm still remain. Further improvements are observed for the sugar-functionalized CNTs, with decreased average bundle sizes of 58.4 ± 42.7 and 49.5 ± 42.9 nm for the CNT-MT and CNT-MH, respectively, along with more left-skewed distributions due to higher proportions of smaller bundles. These results are consistent with the above UV-vis absorbance spectra

doi:10.6342/NTU202502950

(**Figure 4.4b**), which also indicate better aqueous dispersibility for the CNT-MH. This enhanced dispersibility is attributed to a higher density of hydroxyl groups in the CNT-MH, which promote stronger hydrogen bonding with water and more efficient steric stabilization.

Additional microstructural features are revealed by the transmission electron microscopy (TEM) analysis in **Figure 4.14**. Here, both the CNT-MT and CNT-MH exhibit distinct polymer sheaths surrounding their CNT cores. This sheath appears as a lighter (less electron-dense) coating, and indicates covalent attachment of the sugar functional layer to the CNT surface. The presence of this coating confirms the successful surface modification and provides further evidence of enhanced interfacial interactions between the CNTs and the surrounding medium. Taken together, the AFM, SEM, and TEM results demonstrate that sugar functionalization, particularly with longer-chain MH, substantially improves CNT dispersion by reducing aggregation and promoting a homogeneous film morphology. These enhancements are crucial for optimizing the solution processability and facilitating the integration of CNT-based nanocomposites into functional devices.

doi:10.6342/NTU202502950

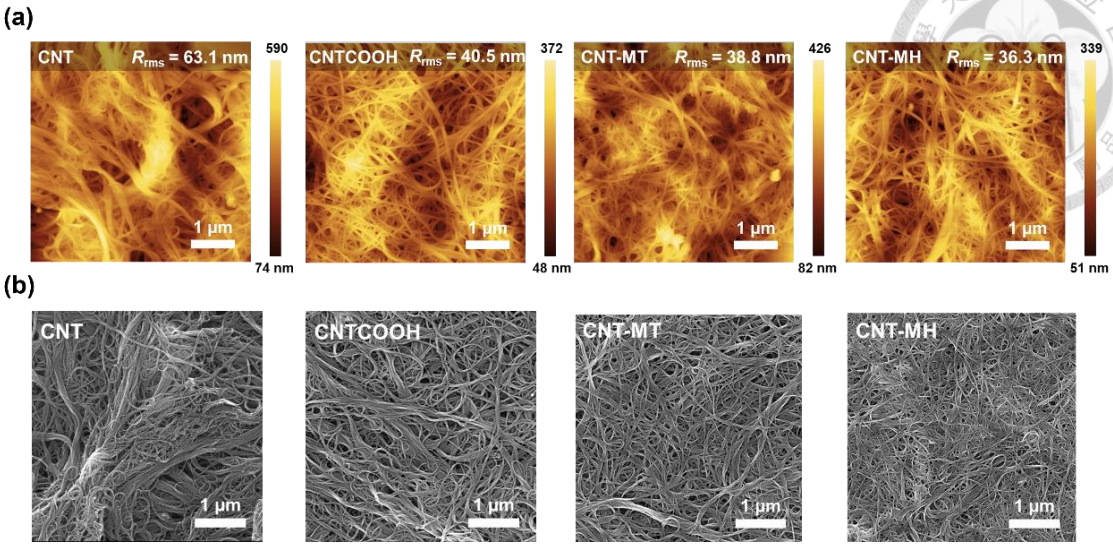

Figure 4.12 (a) AFM images (b) SEM images of pristine and functionalized CNT thin films.

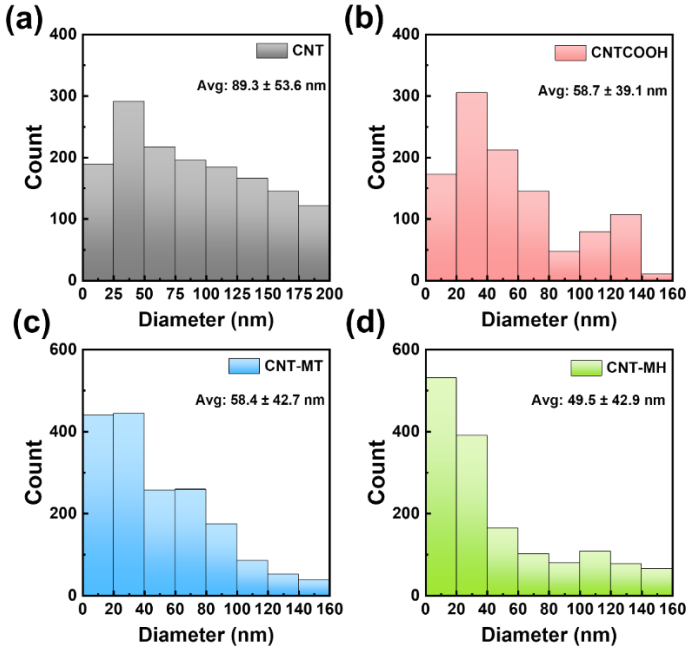

Figure 4.13 CNT network bundle size obtained from SEM images. Bundle size measurements were performed using ImageJ software.

doi:10.6342/NTU202502950

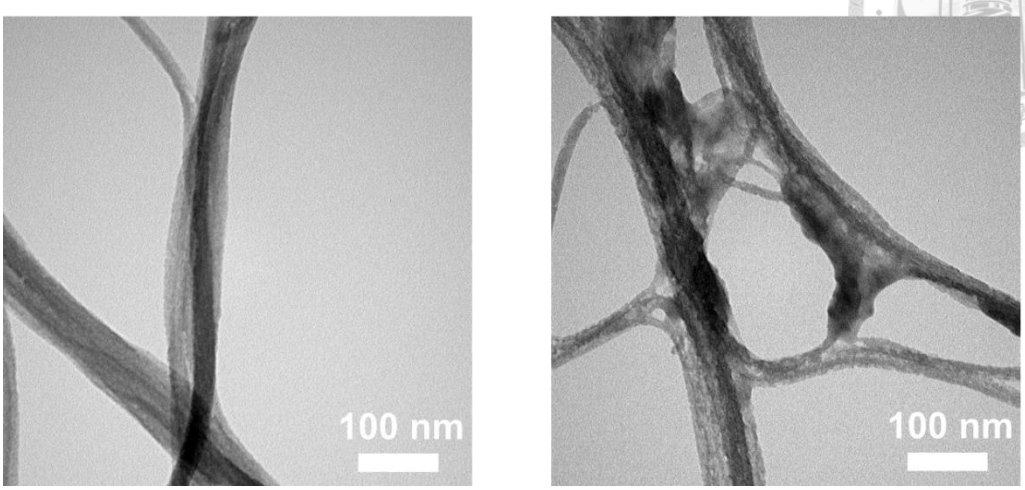

Figure 4.14 TEM images of CNT-MT and CNT-MH thin films.

4.2.5. Theoretical Simulation of Sugar-Functionalized CNTs

To elucidate the interfacial behavior of the sugar-functionalized CNTs in aqueous environments, density functional theory (DFT) and molecular dynamics (MD) simulations were employed. Initial geometric optimizations of the sugar moieties were conducted at the B3LYP/6-311G(d,p) level of theory. The optimized sugar units were then grafted onto the CNT surface, with four sugar molecules per CNT to mimic the experimental functionalization densities. Subsequent MD simulations were performed using the Nanoscale Molecular Dynamics (NAMD) package to investigate the structural evolution and interfacial interactions of the functionalized CNTs in water (**Figure 4.15**). Specific atomic sites for analysis are illustrated in **Figure 4.16a**, and a detailed description

doi:10.6342/NTU202502950

of the computational methodology is provided in the Supporting Information.

Experimental studies have demonstrated that surface functionalization is an effective strategy for tailoring the interfacial properties of CNTs, thereby enhancing their compatibility with various surrounding media.[121] To quantify these interfacial effects, the interaction strength between CNTs (pristine and functionalized) and surrounding water molecules was evaluated. Specifically, the interaction energy was computed as the difference between the total interaction energy of the combined system (CNT/water or functionalized-CNT/water) and the sum of the interaction energies of the isolated water and CNTs or functionalized-CNTs. As shown in **Figure 4.16b**, the time-resolved interaction energy profiles exhibit persistent oscillations, with the pristine CNTs displaying the least favorable interaction (approximately –1300 kcal mol^{-1}), which is indicative of hydrophobic behavior and a strong tendency to self-aggregate in aqueous environments with poor dispersibility. By contrast, functionalized CNTs with hydroxyl or carboxyl groups exhibit progressively more negative interaction energies that are indicative of stronger interactions with water. A clear trend emerges, wherein increasing the number of hydroxyl groups on the CNT surface leads to enhanced water-CNT interactions, with interaction energies of approximately –1450, –2000, and –2900 kcal mol^{-1} for the CNTCOOH, CNT-MT, and CNT-MH, respectively. These

doi:10.6342/NTU202502950

simulation results demonstrate that water molecules preferentially interact with functionalized CNT surfaces, particularly those enriched with hydroxyl groups in sugar chains, via the formation of hydrogen bonds. This enhanced interfacial affinity is consistent with the experimentally observed improvements in dispersion stability for the sugar-functionalized CNTs.[122]

In MD simulations, the intermolecular radial distribution function (RDF), denoted as $g(r)$, is a fundamental tool for probing the local structural organization of atoms or molecules in a system.[123] The RDF uses the coordination number, n_{xy}, to describe the average density of *y* atoms contained within a sphere of radius *r* centered on a reference atom *x*, thereby representing the spatial distribution of local atomic density. This function can be expressed by the following equation:

$$n_{xy} = 4\pi\rho_0 \int_0^R g_{xy}(r) r^2 \, dr$$

where ρ_0 denotes the number density of *y* atoms.

The RDF analysis for the oxygen atoms of the water molecules surrounding specific carbon atoms in the studied system is presented in **Figure 4.16c**. For the functionalized CNTs, the reference carbon atom is defined as the one that is covalently bonded to the functional group (defined in **Figure 4.16a**), thus allowing for consistent comparison

doi:10.6342/NTU202502950

across different surface chemistries. The $g(r)$ functions of the CNT-MT and CNT-MH exhibit sharp peaks at 4.1 and 4.0 Å, respectively, while the CNTCOOH and pristine CNT functions exhibit peaks at slightly larger distances of 4.5 and 4.6 Å, respectively, which is consistent with a previous report.[124] The closer proximity of water molecules to the sugar-functionalized CNTs reflects their enhanced hydrophilicity and stronger hydration shell formation. Notably, despite their inherent amphiphilic nature and enhanced affinity, the sugar-functionalized CNTs exhibit a lower RDF intensity than expected. This may be attributed to steric hindrance introduced by the bulky sugar chains, which limits the space available for water molecules near the CNT surface. The subsequent peaks correspond to additional, less ordered layers of water molecules further from the CNT surface. As the distance increases, the RDF curves converge to a constant value, thus signifying the transition from interfacial structuring to bulk-like water behavior.[125]

To explore the positional dependence of water interactions, RDFs were also calculated for inner (H1) and terminal (H2) hydrogen atoms on the sugar chains in the CNT-MT and CNT-MH (**Figure 4.16d–e**). Here, both H1 and H2 exhibit a prominent first peak at 2.0 Å, corresponding to the first hydration shell, where water molecules form hydrogen bonds with the functional groups on the CNT surface.[126] Notably, the H1 atoms exhibit a higher RDF intensity (**Figure 4.16d**) and greater integrated coordination

doi:10.6342/NTU202502950

number (**Table 4.5**) for the CNT-MH than for the CNT-MT, thereby confirming stronger interaction with water in the former due to the longer sugar chains. For the H2 atoms, however, the CNT-MT exhibits more intense RDF peaks than the CNT-MH, which is likely due to reduced steric crowding and increased chain flexibility that facilitate closer water interactions at the terminal sites. Taken together, the results in **Figure 4.17** and **Table 4.5** show that water molecules preferentially accumulate near the hydroxyl-bearing hydrogen atoms of the sugar units due to hydrogen bonding interactions, and are depleted near the hydrophobic carbon backbone of the CNT surface due to the presence of only weak van der Waals interactions. These simulation results confirm that sugar functionalization significantly enhances the interfacial affinity of CNTs toward water through hydrogen bonding and electrostatic interactions, thereby improving their aqueous dispersion.

doi:10.6342/NTU202502950

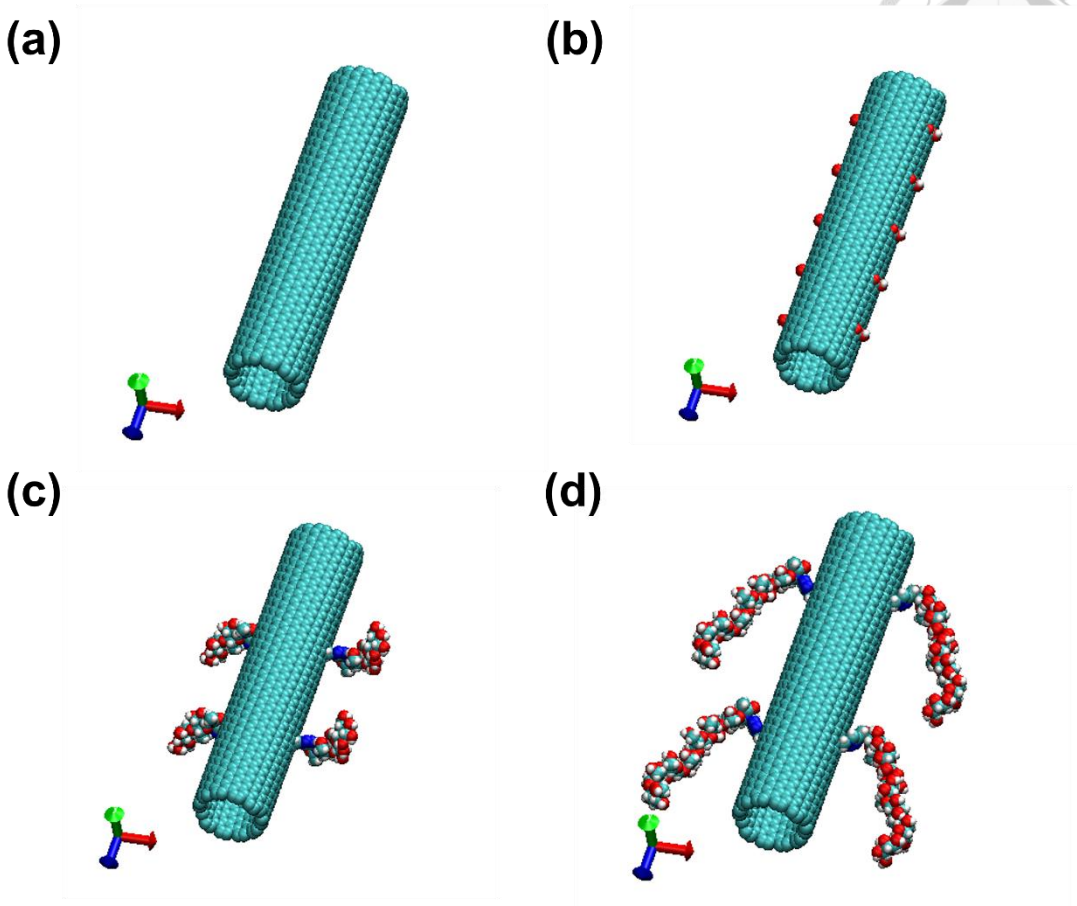

Figure 4.15 Molecular dynamics (MD) simulation snapshots: (a) pristine CNT, (b) CNT functionalized with 10 formic acid molecules (CNT-COOH), (c) CNT functionalized with 4 MT chains (CNT–MT), and (d) CNT functionalized with 4 MH chains (CNT–MH).

doi:10.6342/NTU202502950

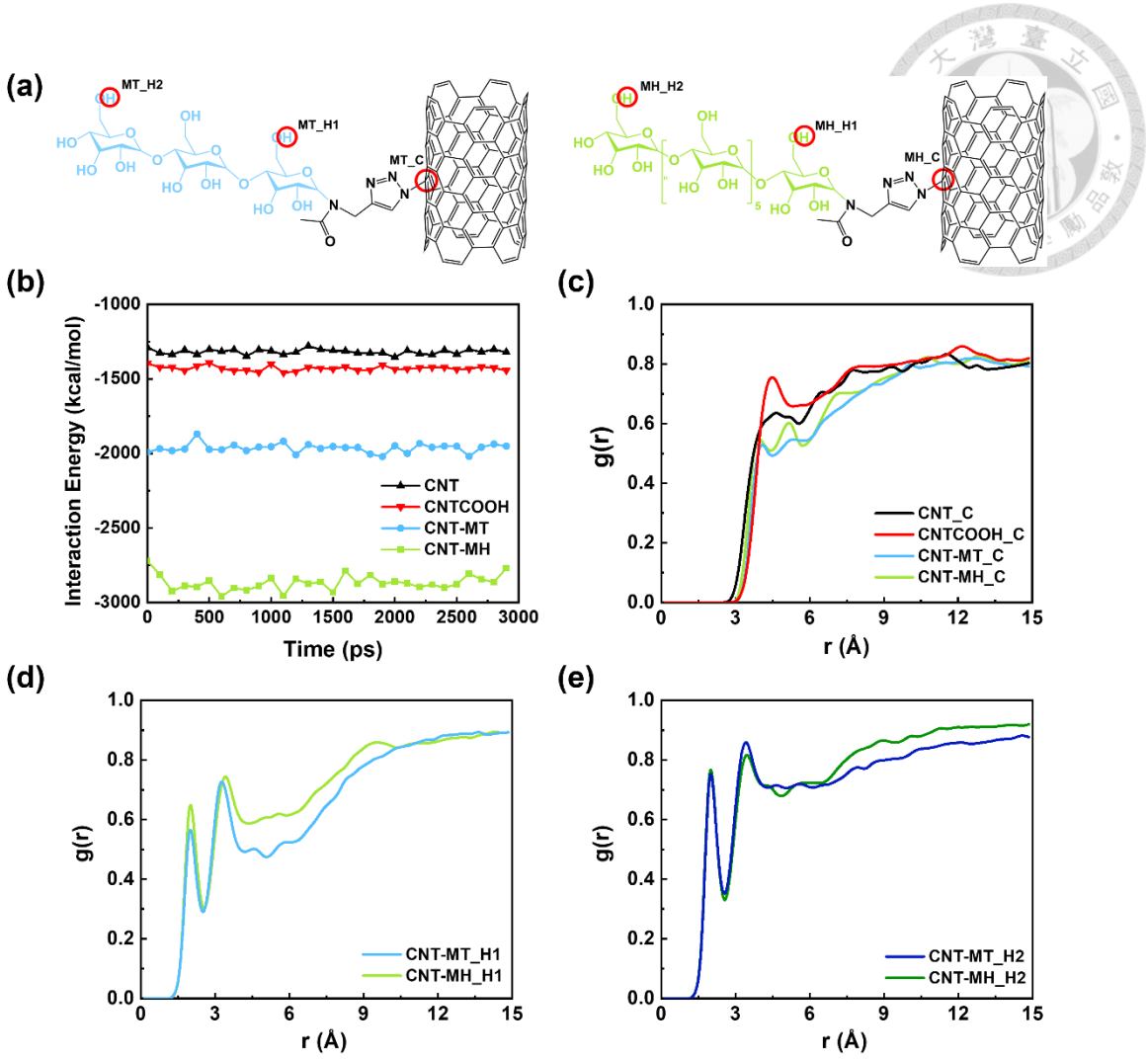

Figure 4.16 (a) Annotated atomic positions of MT and MH used for the radial distribution function analysis. (b) Evolution of interaction energy over 3 ns of molecular dynamics simulations at 300 K. (c) Radial distribution functions between oxygen atoms of water and carbon atoms in different samples. Radial distribution functions between oxygen atoms of water and specific hydrogen atoms in the sugar-functionalized CNTs: (d) inner H1 and (e) terminal H2 in CNT-MT and CNT-MH.

doi:10.6342/NTU202502950

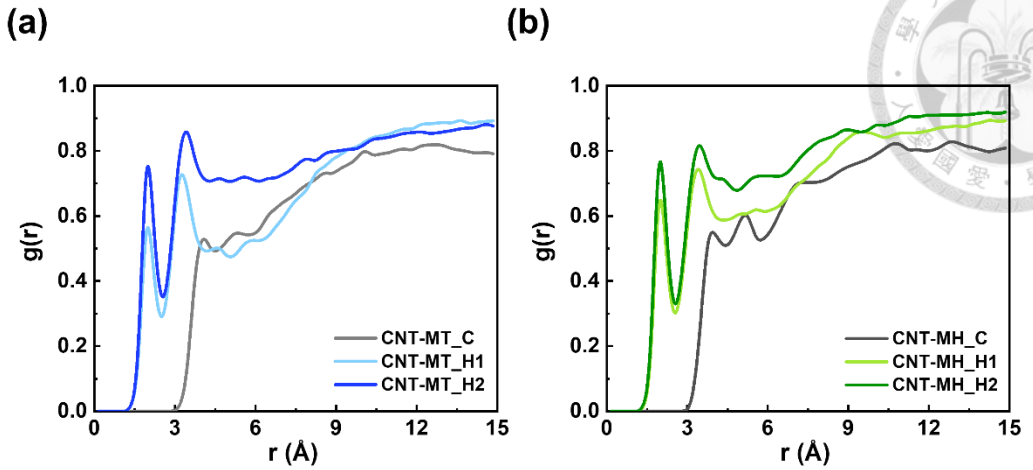

Figure 4.17 Radial distribution functions between oxygen atoms of water and various atomic sites in (a) CNT-MT (b) CNT-MH.

Table 4.5 Coordination numbers $\boldsymbol{n}$ of water oxygen atoms within cutoff distances of 6 Å and 12 Å around different atomic sites in the simulated CNT-MT and CNT-MH systems.

	CNT-MT_C	**CNT-MT_H1**	**CNT-MT_H2**	**CNT-MH_C**	**CNT-MH_H1**	**CNT-MH_H2**
6 Å	11.44	14.08	19.38	12.21	16.51	19.03
12 Å	347.00	374.00	380.87	351.29	382.23	401.54

doi:10.6342/NTU202502950

4.2.6. Thermoelectric Performance of Sugar-functionalized CNTs

The thermoelectric performances of the as-prepared pristine and functionalized CNT films are summarized in **Figure 4.18**, **Figure 4.19**, and **Table 4.6**. All films prepared in ambient using water as the processing solvent demonstrate a positive Seebeck coefficient (S).[25] However, the pristine CNT and CNTCOOH films exhibit distinct electrical conductivity (σ) values of 233.83 ± 91.06 and 534.11 ± 71.25 S cm^{-1}, respectively. This can be attributed to the improved dispersion of CNTCOOH, which facilitates more uniform film formation and enhanced charge transport pathways. This interpretation is supported by the Hall effect measurements in **Table 4.6**, which reveal a higher charge-carrier concentration of 1.46×10^{23} cm^{-3} for the CNTCOOH compared to 1.19×10^{23} cm^{-3} for the pristine CNTs. The observed high charge-carrier concentration aligns with the behavior of degenerate semiconductors as described by the Mott relation, wherein the Seebeck coefficient decreases with increasing charge-carrier concentration.[95] Therefore, the CNTCOOH film displays the lowest S value of 29.84 ± 7.53 μV K^{-1}, along with a moderate power factor (PF) of 47.78 ± 22.62 μW m^{-1} K^{-2}. Conversely, the pristine CNT exhibits the highest S value of 54.61 ± 4.08 μV K^{-1}, which also results in the highest PF of 70.06 ± 26.57 μW m^{-1} K^{-2}. However, the degenerate semiconductor mechanism described by the Mott relation does not fully apply to the sugar-functionalized CNTs.

doi:10.6342/NTU202502950

Although the covalent attachment of sugar moieties causes negligible disruption to the extended conjugated sp^2 carbon network (as indicated by the comparable I_D/I_G values in **Figure 4.4d**), the intrinsically insulating nature of the sugar units impedes the charge carrier transport. This adverse effect directly contributes to the reduced charge-carrier concentration observed in the sugar-functionalized CNTs (**Table 4.7**). As a result, the CNT-MT and CNT-MH exhibit significantly lower σ values of 178.59 ± 64.71 and 124.92 ± 51.89 S cm^{-1}, respectively. Notably, despite the differences in chain length, the immobilization of sugars with the same monomeric unit results in comparable *S* values of 40.28 ± 9.88 and 41.96 ± 7.11 μV K^{-1} for the CNT-MT and CNT-MH, respectively. This outcome likely stems from the analogous electronic interactions of MT and MH with the CNT network, along with a comparable influence on charge-carrier scattering at the interface.[127] Overall, the sugar-functionalized CNTs present lower *PF* values of 24.22 ± 3.97 and 19.20 ± 3.57 μW m^{-1} K^{-2} for the CNT-MT and CNT-MH, respectively.

Despite the comparatively modest *PF* values of the sugar-functionalized CNTs, these results do not rule out functionalization as a promising route for enhancing the thermoelectric properties. A more comprehensive evaluation should include the dimensionless figure of merit (*zT*), which is particularly relevant for low-dimensional materials because it incorporates the κ value and the operating temperature. Hence, the

doi:10.6342/NTU202502950

κ and *zT* values of the various samples are presented in **Figure 4.8** and **Figure 4.18**. Thus, although the pristine CNT film exhibits the highest *PF*, it also possesses a relatively large κ value of 15.56 W m^{-1} K^{-1}, thus resulting in a moderate *zT* of 1.36×10^{-3}. Meanwhile, the CNTCOOH film manifests the lowest *zT* of 8.90×10^{-4}, which is primarily due to its highest κ value of 16.23 W m^{-1} K^{-1} among all the samples. The introduction of an insulating sugar polymer effectively reduces the κ value, thus resulting in *zT* values of 1.25×10^{-3} and 1.46×10^{-3} for the CNT-MT and CNT-MH, respectively. In conclusion, although the covalently functionalized sugar on the CNT surface gives only a modest enhancement in *zT*, with MH giving the best result, it nonetheless highlights the potential of polymer functionalization as a viable strategy for enhancing both the dispersibility and thermoelectric properties of CNTs in aqueous media. Importantly, the ability to tailor interfacial interactions via surface engineering offers a versatile pathway for optimizing CNT-based nanocomposites for thermoelectric and related energy conversion applications.

doi:10.6342/NTU202502950

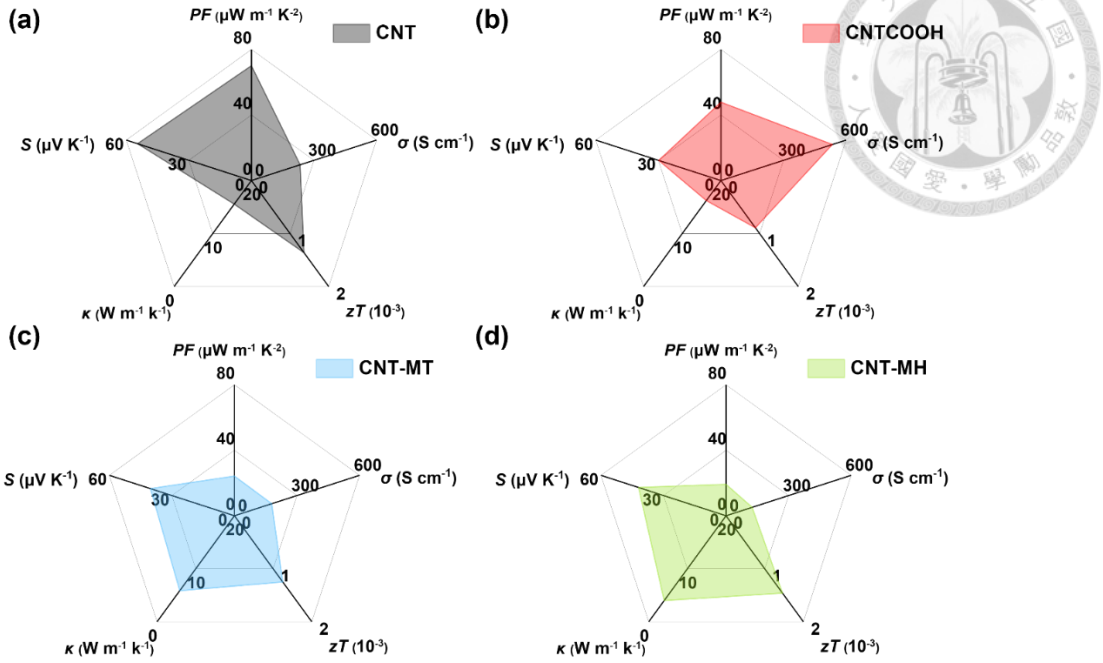

Figure 4.18 Comparative analysis of thermoelectric performance of (a) CNT (b) CNTCOOH (c) CNT-MT and (d) CNT-MH.

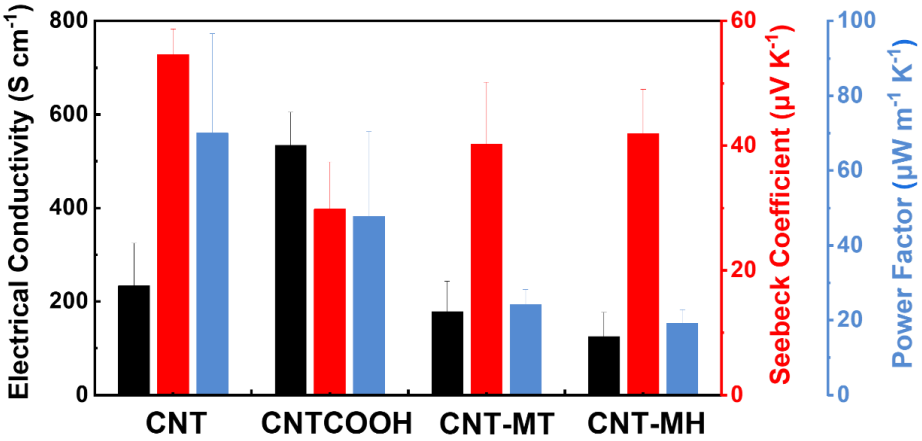

Figure 4.19 Electrical conductivity, Seebeck coefficient and power factor of pristine CNT and functionalized CNTs.

doi:10.6342/NTU202502950

Table 4.6 Thermoelectric characteristics of pristine CNT and functionalized CNTs.

Sample	σ [S cm^{-1}]	*S* [uV K^{-1}]	*PF* [uW m^{-1} K^{-2}]	κ [W m^{-1} K^{-1}]	*zT* [10^{-3}]
CNT	233.83	54.61	70.06	15.56	1.36
CNTCOOH	534.11	29.84	47.78	16.23	0.89
CNT-MT	178.59	40.28	24.22	5.86	1.25
CNT-MH	124.92	41.96	19.20	4.00	1.46

Table 4.7 Hall effect measurement results for pristine CNT and functionalized CNTs.

Sample	Carrier concentration [cm^{-3}]	Carrier mobility [cm^2 V^{-1} s^{-1}]
CNT	1.19×10^{23}	3.02×10^{-2}
CNTCOOH	1.46×10^{23}	4.12×10^{-2}
CNT-MT	2.36×10^{22}	5.57×10^{-2}
CNT-MH	2.03×10^{22}	3.88×10^{-2}

doi:10.6342/NTU202502950

4.3. Summary

Herein, a comprehensive investigation was conducted on the synthesis and characterization of sugar-functionalized carbon nanotubes (CNTs), with pristine CNTs and carboxylated CNTs (CNTCOOH) being included as reference materials for comparison. The sugar-functionalized CNTs were synthesized via the copper(I)-catalyzed azide–alkyne cycloaddition approach, thereby enabling the covalent attachment of sugar moieties onto the CNT sidewalls via the formation of stable 1,2,3-triazole linkages. Extensive spectroscopic characterizations and thermal analyses confirmed the successful functionalization and provided detailed insights into the chemical structures and surface compositions of the modified CNTs. A morphological analysis revealed that the introduction of sugar functional groups significantly enhances the dispersibility of CNTs in aqueous media, thereby increasing solution processability and enabling the fabrication of homogeneous films. This observation was further supported by molecular dynamics simulations, which offer atomistic insights into the interfacial interactions. The increased interaction between sugar-functionalized CNTs and water molecules contributes to their improved dispersion behavior. With respect to the thermoelectric performance, the covalently bonded sugars on the CNT surface inevitably disrupt charge-carrier transport, a drawback that the enhanced dispersibility cannot compensate for.

doi:10.6342/NTU202502950

Conversely, this same interfacial modification leads to a significant reduction in thermal conductivity. Overall, the maltoheptaose (MH) functionalized CNT sample exhibits the highest figure of merit (zT) value of 1.46×10^{-3}, while the maltotriose (MT) functionalized CNT demonstrates a moderate zT value of 1.25×10^{-3}. These results suggest that the sugar chain length and functional group density are influential factors in modulating the thermoelectric properties, thus highlighting the need for further investigation into structure–property relationships in functionalized CNT systems. Moreover, this sugar functionalization approach provides a chemically versatile and bio-inspired route to the engineering of CNT interfaces with potential utility not only in thermoelectric fields but also in biosensing, drug delivery, and green electronics.

doi:10.6342/NTU202502950

5. Conclusion and Future Perspective

Taken together, this study presents two distinct approaches for utilizing sugar-based polymers to facilitate CNT dispersion for TE applications. Based on the experimental results, for the purpose of achieving high-performance nanocomposite materials, the physical adsorption of sugar-based BCPs onto the CNT surface demonstrates superior performance compared to covalently bonded sugar-functionalized CNTs. This outcome can be attributed to the retention of the intrinsic electronic structure of CNTs, which is often disrupted by covalent modifications, as well as the advantages of using organic solvents over aqueous media for achieving dispersion effective CNT dispersion and maintaining high TE performance.

In the case of sugar-based BCPs, future investigations will explore the potential for replacing the PS block with organic semiconductor polymers such as poly(3-hexylthiophene) (P3HT), which is expected to enhance the charge-carrier transport and inter-tube charge transfer in the composite. Indeed, such a system has already been synthesized and we intend to investigate the properties of these sugar-based CNT composites in a forthcoming work.[128] If the modified BCPs maintain their dispersant capabilities, the resulting increase in electrical conductivity could substantially boost the TE efficiency.

doi:10.6342/NTU202502950

On the other hand, aqueous dispersion of CNTs offers a more sustainable and environmentally benign route for the fabrication of TE materials. While covalent functionalization with sugar moieties enables stable dispersion in water, the accompanying disruption to the CNT's conjugated π-network often compromises electrical conductivity. Future research could explore strategies to mitigate this trade-off, such as employing non-covalent functionalization using water-soluble π-conjugated polymers, or developing cleavable or reversible covalent linkages that preserve the intrinsic electronic properties post-processing. In addition, integrating bio-derived or biodegradable dispersants aligned with green chemistry principles may provide pathways toward scalable, solution-processable, and eco-friendly TE systems. Advances in this direction could unlock the potential of aqueous CNT dispersions for flexible, wearable, or biocompatible TE applications.

doi:10.6342/NTU202502950

6. Reference

[1] J. J. Bozell, G. R. Petersen, *Green chemistry* **2010**, 12, 539.

[2] T. J. Seebeck, *Annalen der Physik* **1826**, 82, 133.

[3] M. Massetti, F. Jiao, A. J. Ferguson, D. Zhao, K. Wijeratne, A. Würger, J. L. Blackburn, X. Crispin, S. Fabiano, *Chem. Rev.* **2021**, 121, 12465.

[4] A. Tripathi, Y. Lee, S. Lee, H. Y. Woo, *Journal of Materials Chemistry C* **2022**, 10, 6114.

[5] A. D. LaLonde, Y. Pei, H. Wang, G. J. Snyder, *Mater. Today* **2011**, 14, 526.

[6] O. Caballero-Calero, J. R. Ares, M. Martín-González, *Advanced Sustainable Systems* **2021**, 5, 2100095.

[7] M. Ohtaki, K. Araki, K. Yamamoto, *J. Electron. Mater.* **2009**, 38, 1234.

[8] K. Fujita, T. Mochida, K. Nakamura, *Japanese Journal of Applied Physics* **2001**, 40, 4644.

[9] B. Ge, R. Li, G. Wang, M. Zhu, C. Zhou, *J. Am. Ceram. Soc.* **2024**, 107, 1985.

[10] a) K.-T. Lee, D.-S. Lee, W.-H. Chen, Y.-L. Lin, D. Luo, Y.-K. Park, A. Bandala, *Iscience* **2023**, 26; b) D. Zhou, H. Zhang, H. Zheng, Z. Xu, H. Xu, H. Guo, P. Li, Y. Tong, B. Hu, L. Chen, *Small* **2022**, 18, 2200679.

[11] L. Deng, Y. Liu, Y. Zhang, S. Wang, P. Gao, *Adv. Funct. Mater.* **2023**, 33, 2210770.

[12] S. Qu, Q. Yao, L. Wang, Z. Chen, K. Xu, H. Zeng, W. Shi, T. Zhang, C. Uher, L. Chen, *NPG Asia Materials* **2016**, 8, e292.

[13] G.-H. Kim, L. Shao, K. Zhang, K. P. Pipe, *Nat. Mater.* **2013**, 12, 719.

[14] S. Lee, S. Kim, A. Pathak, A. Tripathi, T. Qiao, Y. Lee, H. Lee, H. Y. Woo, *Macromolecular Research* **2020**, 28, 531.

[15] B. T. McGrail, A. Sehirlioglu, E. Pentzer, *Angew. Chem. Int. Ed.* **2015**, 54, 1710.

[16] a) J. S. Bulmer, A. Kaniyoor, J. A. Elliott, *Adv. Mater.* **2021**, 33, 2008432; b) M. V. Kharlamova, *Prog. Mater Sci.* **2016**, 77, 125.

[17] Y. Bao, Y. Sun, F. Jiao, W. Hu, *Advanced Electronic Materials* **2023**, 9, 2201310.

[18] S. Iijima, *nature* **1991**, 354, 56.

[19] N. Hamada, S.-i. Sawada, A. Oshiyama, *Phys. Rev. Lett.* **1992**, 68, 1579.

[20] a) H. Kataura, Y. Kumazawa, Y. Maniwa, I. Umezu, S. Suzuki, Y. Ohtsuka, Y. Achiba, *Synth. Met.* **1999**, 103, 2555; b) Y.-K. Kwon, D. Tománek, *Phys. Rev. B*

doi:10.6342/NTU202502950

1998, 58, R16001.

[21] a) Y.-M. Liu, X.-L. Shi, T. Wu, H. Wu, Y. Mao, T. Cao, D.-Z. Wang, W.-D. Liu, M. Li, Q. Liu, *Nat. Commun.* **2024**, 15, 3426; b) J.-Y. Seo, B. Mostafiz, X. Tu, C. Y. Khripin, M. Zheng, H. Li, E. Peltola, *Phys. Chem. Chem. Phys.* **2025**, 27, 4959.

[22] B. Kumanek, G. Stando, P. Stando, K. Matuszek, K. Z. Milowska, M. Krzywiecki, M. Gryglas-Borysiewicz, Z. Ogorzałek, M. C. Payne, D. MacFarlane, *Sci. Rep.* **2021**, 11, 8649.

[23] S. Zhou, X. L. Shi, L. Li, Q. Liu, B. Hu, W. Chen, C. Zhang, Q. Liu, Z. G. Chen, *Adv. Mater.* **2025**, 2500947.

[24] P. G. Collins, K. Bradley, M. Ishigami, D. Zettl, *Science* **2000**, 287, 1801.

[25] S. Hata, M. Shiraishi, S. Yasuda, G. Juhasz, Y. Du, Y. Shiraishi, N. Toshima, *Energy Mater. Adv.* **2022**.

[26] J. Chen, *DYSONA-Applied Science* **2022**, 3, 46.

[27] R. S. Prasher, X. Hu, Y. Chalopin, N. Mingo, K. Lofgreen, S. Volz, F. Cleri, P. Keblinski, *Phys. Rev. Lett.* **2009**, 102, 105901.

[28] M. J. O'connell, S. M. Bachilo, C. B. Huffman, V. C. Moore, M. S. Strano, E. H. Haroz, K. L. Rialon, P. J. Boul, W. H. Noon, C. Kittrell, *Science* **2002**, 297, 593.

[29] A. Abdulhameed, N. Z. A. Wahab, M. N. Mohtar, M. N. Hamidon, S. Shafie, I. A. Halin, *J. Electron. Mater.* **2021**, 50, 3207.

[30] a) K. D. Ausman, R. Piner, O. Lourie, R. S. Ruoff, M. Korobov, *J. Phys. Chem. B* **2000**, 104, 8911; b) J. L. Bahr, E. T. Mickelson, M. J. Bronikowski, R. E. Smalley, J. M. Tour, *Chem. Commun.* **2001**, 193.

[31] a) R. J. Chen, Y. Zhang, D. Wang, H. Dai, *J. Am. Chem. Soc.* **2001**, 123, 3838; b) B. J. Landi, H. J. Ruf, J. J. Worman, R. P. Raffaelle, *J. Phys. Chem. B* **2004**, 108, 17089.

[32] F. Torrens, *Int. J. Quantum Chem.* **2006**, 106, 712.

[33] F. Daneshvar, H. Chen, K. Noh, H.-J. Sue, *Nanoscale Adv.* **2021**, 3, 942.

[34] L. Jiang, L. Gao, J. Sun, *J. Colloid Interface Sci.* **2003**, 260, 89.

[35] J. Yu, N. Grossiord, C. E. Koning, J. Loos, *Carbon* **2007**, 45, 618.

[36] a) S. Gómez, N. M. Rendtorff, E. F. Aglietti, Y. Sakka, G. Suárez, *Appl. Surf. Sci.* **2016**, 379, 264; b) S. W. Kim, T. Kim, Y. S. Kim, H. S. Choi, H. J. Lim, S. J. Yang, C. R. Park, *Carbon* **2012**, 50, 3; c) H. Leinonen, M. Pettersson, M. Lajunen, *Carbon* **2011**, 49, 1299.

[37] D. Liu, L. Shi, Q. Dai, X. Lin, R. Mehmood, Z. Gu, L. Dai, *Trends in Chemistry* **2024**.

doi:10.6342/NTU202502950

[38] a) A. Kuznetsova, I. Popova, J. T. Yates Jr, M. J. Bronikowski, C. B. Huffman, J. Liu, R. E. Smalley, H. H. Hwu, J. G. Chen, *J. Am. Chem. Soc.* **2001**, 123, 10699; b) J. Lee, D. R. Hwang, J. Hong, D. Jung, S. E. Shim, *J. Dispersion Sci. Technol.* **2010**, 31, 1230; c) H. Yu, Y. Jin, F. Peng, H. Wang, J. Yang, *J. Phys. Chem. C* **2008**, 112, 6758.

[39] a) L. S. Salah, N. Ouslimani, D. Bousba, I. Huynen, Y. Danlée, H. Aksas, *J. Nanomater.* **2021**, 2021, 4972770; b) L. Vaisman, G. Marom, H. D. Wagner, *Adv. Funct. Mater.* **2006**, 16, 357.

[40] a) V. N. Khabashesku, W. E. Billups, J. L. Margrave, *Acc. Chem. Res.* **2002**, 35, 1087; b) Z. Qian, J. Ma, J. Zhou, P. Lin, C. Chen, J. Chen, H. Feng, *J. Mater. Chem.* **2012**, 22, 22113.

[41] C. A. Dyke, J. M. Tour, *Nano Lett.* **2003**, 3, 1215.

[42] a) J. K. Lim, W. S. Yun, M.-h. Yoon, S. K. Lee, C. H. Kim, K. Kim, S. K. Kim, *Synth. Met.* **2003**, 139, 521; b) C. Zhao, X. Wang, X. Chen, Y. Liu, Y. Xie, H. Xu, *Mater. Chem. Front.* **2020**, 4, 1174.

[43] M. Hamon, H. Hui, P. Bhowmik, H. Itkis, R. Haddon, *Appl. Phys. A* **2002**, 74, 333.

[44] S. Qin, D. Qin, W. T. Ford, D. E. Resasco, J. E. Herrera, *Macromolecules* **2004**, 37, 752.

[45] C. Gao, C. D. Vo, Y. Z. Jin, W. Li, S. P. Armes, *Macromolecules* **2005**, 38, 8634.

[46] N. G. Sahoo, S. Rana, J. W. Cho, L. Li, S. H. Chan, *Prog. Polym. Sci.* **2010**, 35, 837.

[47] Y. Zhou, Q. Wei, M. Zhang, H. Nakajima, T. Okazaki, T. Yamada, K. Hata, *ACS Appl. Mater. Interfaces* **2023**, 16, 4199.

[48] X. Lan, C. Liu, T. Wang, J. Hou, J. Xu, R. Tan, G. Nie, F. Jiang, *J. Electron. Mater.* **2019**, 48, 6978.

[49] Y. Wang, Q. Li, J. Wang, Z. Li, K. Li, X. Dai, J. Pan, H. Wang, *Nano Energy* **2022**, 93, 106804.

[50] C.-C. Chueh, C.-Z. Li, F. Ding, Z. a. Li, N. Cernetic, X. Li, A. K.-Y. Jen, *ACS Appl. Mater. Interfaces* **2017**, 9, 1136.

[51] X. Cheng, X. Wang, G. Chen, *J. Mater. Chem. A* **2018**, 6, 19030.

[52] S. Hata, K. Maeshiro, M. Shiraishi, Y. Du, Y. Shiraishi, N. Toshima, *ACS Appl. Electron. Mater.* **2022**, 4, 1153.

[53] a) H.-Y. Chen, H.-P. Shen, C.-H. Wu, W.-Y. Chiu, W.-C. Chen, H.-J. Tai, *Journal of Materials Chemistry C* **2013**, 1, 5351; b) K. Zhang, J. Qiu, S. Wang,

doi:10.6342/NTU202502950

Nanoscale **2016**, 8, 8033.

[54] C. Yu, K. Choi, L. Yin, J. C. Grunlan, *ACS Nano* **2011**, 5, 7885.

[55] Q. Yao, L. Chen, W. Zhang, S. Liufu, X. Chen, *ACS Nano* **2010**, 4, 2445.

[56] Q. Yao, Q. Wang, L. Wang, L. Chen, *Energy Environ. Sci.* **2014**, 7, 3801.

[57] a) C. T. Hong, Y. H. Kang, J. Ryu, S. Y. Cho, K.-S. Jang, *J. Mater. Chem. A* **2015**, 3, 21428; b) S. Mardi, K. Yusupov, P. M. Martinez, A. Zakhidov, A. Vomiero, A. Reale, *ACS Omega* **2021**, 6, 1073.

[58] a) Y. Li, C.-Y. Gao, X.-H. Fan, L.-M. Yang, *Chem. Eng. J.* **2022**, 443, 136536; b) J. Wu, Y. Sun, W.-B. Pei, L. Huang, W. Xu, Q. Zhang, *Synth. Met.* **2014**, 196, 173.

[59] a) J. G. Jang, T.-h. Kim, S. H. Kim, J.-I. Hong, *ACS Appl. Electron. Mater.* **2023**, 5, 5573; b) Y. H. Kang, Y.-C. Lee, C. Lee, S. Y. Cho, *Org. Electron.* **2018**, 57, 165.

[60] a) J. Wang, D. Wang, Y. Zhang, J. Dong, *ACS Biomater. Sci. Eng.* **2021**, 7, 963; b) J.-S. Benas, F.-C. Liang, W.-C. Chen, C.-W. Hung, J.-Y. Chen, Y. Zhou, S.-T. Han, R. Borsali, C.-C. Kuo, *Chem. Eng. J.* **2022**, 431, 133701; c) I. Otsuka, N. Nilsson, D. Suyatin, I. Maximov, R. Borsali, *Soft Matter* **2017**, 13, 7406; d) L. Mazzarino, C. Travelet, S. Ortega-Murillo, I. Otsuka, I. Pignot-Paintrand, E. Lemos-Senna, R. Borsali, *J. Colloid Interface Sci.* **2012**, 370, 58.

[61] G. L. Gregory, E. M. López-Vidal, A. Buchard, *Chem. Commun.* **2017**, 53, 2198.

[62] Y. Zhang, J. W. Chan, A. Moretti, K. E. Uhrich, *J. Controlled Release* **2015**, 219, 355.

[63] C. Giacomelli, V. Schmidt, K. Aissou, R. Borsali, *Langmuir* **2010**, 26, 15734.

[64] a) Y. C. Chiu, I. Otsuka, S. Halila, R. Borsali, W. C. Chen, *Adv. Funct. Mater.* **2014**, 24, 4240; b) Y. Liao, W. C. Chen, R. Borsali, *Adv. Mater.* **2017**, 29, 1701645; c) S. Tallegas, T. Baron, G. Gay, C. Aggrafeil, B. Salhi, T. Chevolleau, G. Cunge, A. Bsiesy, R. Tiron, X. Chevalier, *Phys. Status Solidi C* **2013**, 10, 1195.

[65] a) N. Baumgarten, M. Mumtaz, D. H. Merino, E. Solano, S. Halila, J. Bernard, E. Drockenmuller, G. Fleury, R. Borsali, *ACS Appl. Mater. Interfaces* **2023**, 15, 23736; b) Y. Liao, L. J. Goujon, E. Reynaud, S. Halila, A. Gibaud, B. Wei, R. Borsali, *Carbohydr. Polym.* **2019**, 212, 222.

[66] a) E. Wilhelm, *J. Solution Chem.* **2018**, 47, 1626; b) I. Otsuka, S. Tallegas, Y. Sakai, C. Rochas, S. Halila, S. Fort, A. Bsiesy, T. Baron, R. Borsali, *Nanoscale* **2013**, 5, 2637.

doi:10.6342/NTU202502950

[67] C. C. Hung, Y. C. Chiu, H. C. Wu, C. Lu, C. Bouilhac, I. Otsuka, S. Halila, R. Borsali, S. H. Tung, W. C. Chen, *Adv. Funct. Mater.* **2017**, 27, 1606161.

[68] T. Mulia, E. Ercan, M. Mumtaz, Y.-C. Lin, R. Borsali, W.-C. Chen, *Carbohydr. Polym.* **2024**, 344, 122476.

[69] A. Lofstrand, R. Jafari Jam, K. Mothander, T. Nylander, M. Mumtaz, A. Vorobiev, W.-C. Chen, R. Borsali, I. Maximov, *ACS Appl. Nano Mater.* **2021**, 4, 5141.

[70] T. Mulia, M. Mumtaz, E. Ercan, W.-C. Yang, C.-F. Lin, Y.-C. Lin, R. Borsali, W.-C. Chen, *ACS Appl. Polym. Mater.* **2023**, 5, 3898.

[71] M. A. Villetti, A. R. Clementino, I. Dotti, P. R. Ebani, E. Quarta, F. Buttini, F. Sonvico, A. Bianchera, R. Borsali, *Molecules* **2021**, 26, 6507.

[72] I. Otsuka, K. Fuchise, S. Halila, S. Fort, K. Aissou, I. Pignot-Paintrand, Y. Chen, A. Narumi, T. Kakuchi, R. Borsali, *Langmuir* **2010**, 26, 2325.

[73] E. Daskalaki, B. Le Droumaguet, D. Gérard, K. Velonia, *Chem. Commun.* **2012**, 48, 1586.

[74] G. Manoharan, P. Bösel, J. Thien, M. Holtmannspötter, L. Meingast, M. Schmidt, H. Eickmeier, M. Haase, J. Maultzsch, M. Steinhart, *Molecules* **2023**, 28, 2161.

[75] a) J. C. Phillips, R. Braun, W. Wang, J. Gumbart, E. Tajkhorshid, E. Villa, C. Chipot, R. D. Skeel, L. Kale, K. Schulten, *J. Comput. Chem.* **2005**, 26, 1781; b) J. C. Phillips, D. J. Hardy, J. D. Maia, J. E. Stone, J. V. Ribeiro, R. C. Bernardi, R. Buch, G. Fiorin, J. Hénin, W. Jiang, *J. Chem. Phys.* **2020**, 153.

[76] W. Humphrey, A. Dalke, K. Schulten, *J. Mol. Graphics* **1996**, 14, 33.

[77] I. Otsuka, M. Osaka, Y. Sakai, C. Travelet, J.-L. Putaux, R. Borsali, *Langmuir* **2013**, 29, 15224.

[78] M. Kleiman, K. A. Ryu, A. P. Esser-Kahn, *Macromol. Chem. Phys.* **2016**, 217, 284.

[79] M. T. García, I. Gracia, G. Duque, A. De Lucas, J. F. Rodríguez, *Waste Manage. (Oxford)* **2009**, 29, 1814.

[80] Y. Hernandez, M. Lotya, D. Rickard, S. D. Bergin, J. N. Coleman, *Langmuir* **2010**, 26, 3208.

[81] P. G. Collins, K. Bradley, M. Ishigami, d. A. Zettl, *Science* **2000**, 287, 1801.

[82] a) S. Liu, H. Li, J. C. C. Yeo, J. Kong, P. Anukunwithaya, C. He, *Carbon* **2023**, 203, 111; b) H.-J. Shin, S. M. Kim, S.-M. Yoon, A. Benayad, K. K. Kim, S. J. Kim, H. K. Park, J.-Y. Choi, Y. H. Lee, *J. Am. Chem. Soc.* **2008**, 130, 2062.

[83] W. Zhao, J. Ding, Y. Zou, C.-a. Di, D. Zhu, *Chem. Soc. Rev.* **2020**, 49, 7210.

doi:10.6342/NTU202502950

[84] Y. Nonoguchi, M. Nakano, T. Murayama, H. Hagino, S. Hama, K. Miyazaki, R. Matsubara, M. Nakamura, T. Kawai, *Adv. Funct. Mater.* **2016**, 26, 3021.
[85] K. Liao, S. Li, *Appl. Phys. Lett.* **2001**, 79, 4225.
[86] B. Yu, S. Fu, Z. Wu, H. Bai, N. Ning, Q. Fu, *Composites, Part A* **2015**, 73, 155.
[87] A. Takano, Y. Ohta, K. Masuoka, K. Matsubara, T. Nakano, A. Hieno, M. Itakura, K. Takahashi, S. Kinugasa, D. Kawaguchi, *Macromolecules* **2012**, 45, 369.
[88] a) A. B. Kaiser, *Phys. Rev. B* **1989**, 40, 2806; b) M. Piao, M. R. Alam, G. Kim, U. Dettlaff-Weglikowska, S. Roth, *Phys. Status Solidi B* **2012**, 249, 2353.
[89] P. Chakraborty, T. Ma, A. H. Zahiri, L. Cao, Y. Wang, *Adv. Condens. Matter Phys.* **2018**, 2018, 3898479.
[90] W. Zhao, S. Fan, N. Xiao, D. Liu, Y. Y. Tay, C. Yu, D. Sim, H. H. Hng, Q. Zhang, F. Boey, *Energy Environ. Sci.* **2012**, 5, 5364.
[91] a) Q. Hao, Y. Xiao, H. Zhao, *J. Appl. Phys.* **2016**, 120; b) R. H. Tarkhanyan, D. G. Niarchos, *J. Electron. Mater.* **2014**, 43, 3808.
[92] S. Costa, E. Borowiak-Palen, M. Kruszynska, A. Bachmatiuk, R. Kalenczuk, *Mater. Sci.-Pol.* **2008**, 26, 433.
[93] a) A. M. Rao, P. Eklund, S. Bandow, A. Thess, R. E. Smalley, *Nature* **1997**, 388, 257; b) J. Zou, L. Liu, H. Chen, S. I. Khondaker, R. D. McCullough, Q. Huo, L. Zhai, *Adv. Mater.* **2008**, 20, 2055.
[94] Z. Lin, H. Dang, C. Zhao, Y. Du, C. Chi, W. Ma, Y. Li, X. Zhang, *Nanoscale* **2022**, 14, 9419.
[95] G. J. Snyder, E. S. Toberer, *Nat. Mater.* **2008**, 7, 105.
[96] P.-S. Lin, S. Inagaki, J.-H. Liu, M.-C. Chen, T. Higashihara, C.-L. Liu, *Chem. Eng. J.* **2023**, 458, 141366.
[97] S. D. Bergin, V. Nicolosi, P. V. Streich, S. Giordani, Z. Sun, A. H. Windle, P. Ryan, N. P. P. Niraj, Z.-T. T. Wang, L. Carpenter, W. J. Blau, J. J. Boland, J. P. Hamilton, J. N. Coleman, *Adv. Mater.* **2008**, 20, 1876.
[98] G. Sun, Z. Liu, G. Chen, *Nano* **2010**, 5, 103.
[99] a) S. D. Bergin, Z. Sun, D. Rickard, P. V. Streich, J. P. Hamilton, J. N. Coleman, *ACS Nano* **2009**, 3, 2340; b) M. W. Forney, J. C. Poler, *J. Phys. Chem. C* **2011**, 115, 10531.
[100] X. Nie, X. Mao, X. Li, J. Wu, Y. Liu, B. Li, L. Xiang, C. Gao, Y. Xie, L. Wang, *Chem. Eng. J.* **2021**, 421, 129718.
[101] F. Abdallah, L. Ciammaruchi, A. Jiménez-Arguijo, E. S. M. Duraia, H. S. Ragab, B. Dörling, M. Campoy-Quiles, *Adv. Mater. Technol.* **2020**, 5, 2000256.

doi:10.6342/NTU202502950

[102] Y. Wang, X. Dai, J. Pan, J. Wang, X. Sun, K. Li, H. Wang, *J. Mater. Chem. A* **2024**, 12, 18948.
[103] R. M. Fernandes, B. Abreu, B. Claro, M. Buzaglo, O. Regev, I. Furó, E. F. Marques, *Langmuir* **2015**, 31, 10955.
[104] a) B. Kadem, M. Göksel, A. Şenocak, E. Demirbaş, D. Atilla, M. Durmuş, T. Basova, K. Shanmugasundaram, A. Hassan, *Polyhedron* **2016**, 110, 37; b) E. C. Landis, R. J. Hamers, *Chem. Mater.* **2009**, 21, 724.
[105] a) A. Devadoss, C. E. Chidsey, *J. Am. Chem. Soc.* **2007**, 129, 5370; b) L. Marinescu, J. Thinggaard, I. B. Thomsen, M. Bols, *J. Org. Chem*, **2003**, 68, 9453.
[106] A. Kirschning, H. Monenschein, C. Schmeck, *Angew. Chem. Int. Ed.* **1999**, 38, 2594.
[107] D. Vennerberg, Z. Rueger, M. R. Kessler, *Polymer* **2014**, 55, 1854.
[108] A. Gouget-Laemmel, J. Yang, M. Lodhi, A. Siriwardena, D. Aureau, R. Boukherroub, J.-N. Chazalviel, F. Ozanam, S. Szunerits, *J. Phys. Chem. C* **2013**, 117, 368.
[109] a) C. Barbot, O. Bouloussa, W. Szymczak, M. Plaschke, G. Buckau, J.-P. Durand, J. Pieri, J. Kim, F. Goudard, *Colloids Surf., A* **2007**, 297, 221; b) Y. Song, Y. Huang, E. A. Havenga, I. S. Butler, *Vib. Spectrosc* **2001**, 27, 127; c) Z. Tang, H. Li, D. W. Hess, V. Breedveld, *Cellulose* **2016**, 23, 1401.
[110] a) W. Tan, J. Zhang, F. Luan, L. Wei, Q. Li, F. Dong, Z. Guo, *Int. J. Biol. Macromol.* **2017**, 101, 845; b) S. Wang, C. Liu, X. Guo, G. Tang, L. Gan, C. Qi, J. Huang, *J. Appl. Polym. Sci.* **2017**, 134, 45359.
[111] a) P. Alafogianni, K. Dassios, S. Farmaki, S. Antiohos, T. Matikas, N.-M. Barkoula, *Colloids Surf., A* **2016**, 495, 118; b) L. Yue, G. Pircheraghi, S. A. Monemian, I. Manas-Zloczower, *Carbon* **2014**, 78, 268.
[112] Z. Liu, J. Zhang, B. Gao, *Chem. Commun.* **2009**, 6902.
[113] a) S. G. King, L. McCafferty, V. Stolojan, S. R. P. Silva, *Carbon* **2015**, 84, 130; b) S. Hussain, K. A. Shah, S. Islam, *Mater. Sci.-Pol.* **2013**, 31, 276.
[114] C. G. Flores-Hernández, A. Colín-Cruz, C. Velasco-Santos, V. M. Castaño, J. L. Rivera-Armenta, A. Almendarez-Camarillo, P. E. García-Casillas, A. L. Martínez-Hernández, *Polymers* **2014**, 6, 686.
[115] G. Sengar, H. K. Sharma, *J. Food Sci. Technol.* **2014**, 51, 1686.
[116] I. Szleifer, R. Yerushalmi-Rozen, *Polymer* **2005**, 46, 7803.
[117] M. Schugmann, P. Foerst, *Foods* **2022**, 11, 1679.
[118] a) A. Saiter, H. Couderc, J. Grenet, *J. Therm. Anal. Calorim.* **2007**, 88, 483; b)

doi:10.6342/NTU202502950

O. Yousefzade, H. Garmabi, J. Puiggali, *Thermochim. Acta* **2018**, 667, 35.
[119] a) S. Hepplestone, A. Ciavarella, C. Janke, G. Srivastava, *Surf. Sci.* **2006**, 600, 3633; b) X. Xie, D. Li, T.-H. Tsai, J. Liu, P. V. Braun, D. G. Cahill, *Macromolecules* **2016**, 49, 972.
[120] F. Deng, Q.-S. Zheng, L.-F. Wang, C.-W. Nan, *Appl. Phys. Lett.* **2007**, 90.
[121] a) D. Aztatzi-Pluma, E. O. Castrejón-González, A. Almendarez-Camarillo, J. F. Alvarado, Y. Duran-Morales, *J. Phys. Chem. C* **2016**, 120, 2371; b) G.-X. Chen, H.-S. Kim, B. H. Park, J.-S. Yoon, *Polymer* **2006**, 47, 4760; c) H. Chen, Q. Xue, Q. Zheng, J. Xie, K. Yan, *J. Phys. Chem. C* **2008**, 112, 16514.
[122] M. Foroutan, M. Moshari, *Phys. E: Low-Dimens. Syst. Nanostruct.* **2010**, 43, 359.
[123] M. P. Allen, D. J. Tildesley, *Computer simulation of liquids*, Oxford university press, **2017**.
[124] K. Balamurugan, P. Baskar, R. M. Kumar, S. Das, V. Subramanian, *Phys. Chem. Chem. Phys.* **2014**, 16, 24509.
[125] A. Srivastava, S. Abedrabbo, J. Hassan, D. Homouz, *Sci. Rep.* **2024**, 14, 15480.
[126] A. P. Terzyk, P. A. Gauden, S. Furmaniak, R. P. Wesołowski, P. Kowalczyk, *Phys. Chem. Chem. Phys.* **2010**, 12, 10701.
[127] M. Statz, S. Schneider, F. J. Berger, L. Lai, W. A. Wood, M. Abdi-Jalebi, S. Leingang, H.-J. r. Himmel, J. Zaumseil, H. Sirringhaus, *ACS Nano* **2020**, 14, 15552.
[128] Y. Sakai-Otsuka, S. Zaioncz, I. Otsuka, S. Halila, P. Rannou, R. Borsali, *Macromolecules* **2017**, 50, 3365.

doi:10.6342/NTU202502950